ELEMENTA
Science of the Anthropocene

Gaudel, A, et al. 2018. Tropospheric Ozone Assessment Report: Present-day distribution and trends of tropospheric ozone relevant to climate and global atmospheric chemistry model evaluation. *Elem Sci Anth,* 6: 39. DOI: https://doi.org/10.1525/elementa.291

RESEARCH ARTICLE

Tropospheric Ozone Assessment Report: Present-day distribution and trends of tropospheric ozone relevant to climate and global atmospheric chemistry model evaluation

A. Gaudel[1,2], O. R. Cooper[1,2], G. Ancellet[3], B. Barret[4], A. Boynard[3,5], J. P. Burrows[6], C. Clerbaux[3], P.-F. Coheur[7], J. Cuesta[8], E. Cuevas[9], S. Doniki[7], G. Dufour[8], F. Ebojie[10], G. Foret[8], O. Garcia[11], M. J. Granados-Muñoz[12,13], J. W. Hannigan[14], F. Hase[15], B. Hassler[1,2,16], G. Huang[17], D. Hurtmans[7], D. Jaffe[18,19], N. Jones[20], P. Kalabokas[21], B. Kerridge[22], S. Kulawik[23,24], B. Latter[22], T. Leblanc[12], E. Le Flochmoën[4], W. Lin[25], J. Liu[26,27], X. Liu[17], E. Mahieu[27], A. McClure-Begley[1,2], J. L. Neu[23], M. Osman[29], M. Palm[6], H. Petetin[4], I. Petropavlovskikh[1,2], R. Querel[28], N. Rahpoe[23], A. Rozanov[23], M. G. Schultz[31,32], J. Schwab[33], R. Siddans[22], D. Smale[20], M. Steinbacher[34], H. Tanimoto[35], D. W. Tarasick[36], V. Thouret[4], A. M. Thompson[37], T. Trickl[38], E. Weatherhead[1,2], C. Wespes[39], H. M. Worden[40], C. Vigouroux[40], X. Xu[41], G. Zeng[30], J. Ziemke[42]

The Tropospheric Ozone Assessment Report (TOAR) is an activity of the International Global Atmospheric Chemistry Project. This paper is a component of the report, focusing on the present-day distribution and trends of tropospheric ozone relevant to climate and global atmospheric chemistry model evaluation. Utilizing the TOAR surface ozone database, several figures present the global distribution and trends of daytime average ozone at 2702 non-urban monitoring sites, highlighting the regions and seasons of the world with the greatest ozone levels. Similarly, ozonesonde and commercial aircraft observations reveal ozone's distribution throughout the depth of the free troposphere. Long-term surface observations are limited in their global spatial coverage, but data from remote locations indicate that ozone in the 21st century is greater than during the 1970s and 1980s. While some remote sites and many sites in the heavily polluted regions of East Asia show ozone increases since 2000, many others show decreases and there is no clear global pattern for surface ozone changes since 2000. Two new satellite products provide detailed views of ozone in the lower troposphere across East Asia and Europe, revealing the full spatial extent of the spring and summer ozone enhancements across eastern China that cannot be assessed from limited surface observations. Sufficient data are now available (ozonesondes, satellite, aircraft) across the tropics from South America eastwards to the western Pacific Ocean, to indicate a likely tropospheric column ozone increase since the 1990s. The 2014–2016 mean tropospheric ozone burden (TOB) between 60°N–60°S from five satellite products is 300 Tg ± 4%. While this agreement is excellent, the products differ in their quantification of TOB trends and further work is required to reconcile the differences. Satellites can now estimate ozone's global long-wave radiative effect, but evaluation is difficult due to limited in situ observations where the radiative effect is greatest.

Keywords: tropospheric ozone; ground-level ozone; Tropospheric composition and chemistry; Global tropospheric ozone burden; Ozone trends

1. Introduction

1.1. The Tropospheric Ozone Assessment Report (TOAR)

Tropospheric ozone is a greenhouse gas and pollutant detrimental to human health, and crop and ecosystem productivity (LRTAP Convention, 2015; REVIHAAP, 2013; US EPA, 2013; Monks et al., 2015). Since 1990 a large portion of the anthropogenic emissions that react in the atmosphere to produce ozone have shifted from North America and Europe to Asia (Granier et al., 2011; Cooper et al., 2014; Zhang et al., 2016). This rapid shift, coupled with limited monitoring in developing nations, has left scientists unable to answer the most basic questions: Which regions of the world have the greatest human and plant exposure to ozone pollution? Is ozone continuing to decline in nations with strong ozone precursor emissions controls? To what extent is ozone increasing in the developing world? Are natural sources of tropospheric ozone and its precursors changing? How can the atmospheric sciences community facilitate access to ozone metrics necessary for quantifying ozone's impact on climate, human health and crop/ecosystem productivity?

To answer these questions the International Global Atmospheric Chemistry Project (IGAC) developed the *Tropospheric Ozone Assessment Report (TOAR): Global metrics for climate change, human health and crop/ecosystem research* (www.igacproject.org/activities/TOAR). Initiated in 2014, TOAR's mission is to provide the research community with an up-to-date scientific assessment of tropospheric ozone's global distribution and trends from the surface to the tropopause. TOAR's primary goals are, 1) Produce the first tropospheric ozone assessment

[1] Cooperative Institute for Research in Environmental Sciences, University of Colorado, Boulder, US

[2] NOAA Earth System Research Laboratory, Boulder, Colorado, US

[3] LATMOS/IPSL, UPMC Univ. Paris 06 Sorbonne Universités, UVSQ, CNRS, Paris, FR

[4] Laboratoire d'Aérologie, UMR 5560, CNRS and Université de Toulouse, Toulouse, FR

[5] SPASCIA, Ramonville Saint-Agne, 31520, FR

[6] Institute of Environmental Physics, University of Bremen, DE

[7] Université libre de Bruxelles (ULB), Atmospheric Spectroscopy, Service de Chimie Quantique et Photophysique, Brussels, BE

[8] Laboratoire Inter-universitaire des Systèmes Atmosphériques (LISA), UMR7583, Universités Paris-Est Créteil et Paris-Diderot, CNRS, Créteil, FR

[9] Izaña Atmospheric Research Centre, AEMET, Santa Cruz de Tenerife, ES

[10] Laboratoire de Physico-Chimie de l'Atmosphère (LPCA), Maison de la Recherche en Environnement Industriel 2 (MREI 2), Université du Littoral Côte d'Opale, Dunkerque, FR

[11] Izaña Atmospheric Research Centre (IARC), Agencia Estatal de Meteorología (AEMET), Santa Cruz de Tenerife, ES

[12] Table Mountain Facility, Jet Propulsion Laboratory, California Institute of Technology, Wrightwood, California, US

[13] Remote Sensing Laboratory (RSLAB), Department of Signal Theory and Communications, Universitat Politècnica de Catalunya (UPC), Barcelona, 08034, ES

[14] Atmospheric Chemistry, Observations & Modeling (ACOM), National Center for Atmospheric Research (NCAR), Boulder, Colorado, US

[15] Hase: Karlsruhe Institute of Technology (KIT), Institute for Meteorology and Climate Research (IMK-ASF), Karlsruhe, DE

[16] Deutsches Zentrum für Luft- und Raumfahrt, Institut für Physik der Atmosphäre, Oberpfaffenhofen, DE

[17] Harvard-Smithsonian Center for Astrophysics, Cambridge, Massachusetts, US

[18] University of Washington Bothell, School of STEM, Bothell, Washington, US

[19] University of Washington Seattle, Department of Atmospheric Sciences, Seattle, Washington, US

[20] Centre for Atmospheric Chemistry, University of Wollongong, Wollongong, AU

[21] Academy of Athens, Research Center for Atmospheric Physics and Climatology, Athens, GR

[22] Rutherford Appleton Laboratory, Chilton, Didcot, Oxfordshire, UK

[23] Jet Propulsion Laboratory, California Institute of Technology, Pasadena, California, US

[24] BAER Institute, Mountain View, California, US

[25] Meteorological Observation Center, China Meteorological Administration, Beijing, CN

[26] Department of Geography and Planning, University of Toronto, CA

[27] School of Atmospheric Sciences, Nanjing University, Nanjing, CN

[28] Institute of Astrophysics and Geophysics, University of Liège (ULg), Liège, BE

[29] Environment Canada/Cooperative Institute for Mesoscale Meteorological Studies, The University of Oklahoma, and NOAA/National Severe Storms Laboratory, Norman, US

[30] National Institute of Water and Atmospheric Research (NIWA), Lauder, NZ

[31] Institute for Energy and Climate Research – Troposphere (IEK-8), Forschungszentrum Jülich, DE

[32] Jülich Supercomputing Centre, Forschungszentrum Jülich, Jülich, DE

[33] Atmospheric Sciences Research Center, University at Albany – State University of New York, Albany, New York, US

[34] Empa, Swiss Federal Laboratories for Materials Science and Technology, Duebendorf, CH

[35] National Institute for Environmental Studies, Tsukuba, JP

[36] Experimental Studies Research Division, MSC/Environment and Climate Change Canada, Downsview, Ontario, CA

[37] NASA/Goddard Space Flight Center, Greenbelt, Maryland, US

[38] Karlsruher Institut für Technologie, IMK-IFU, Garmisch-Partenkirchen, DE

[39] National Center for Atmospheric Research, Boulder, Colorado, US

[40] Royal Belgian Institute for Space Aeronomy, Bruxelles, BE

[41] Institute of Atmospheric Composition, Chinese Academy of Meteorological Sciences, China Meteorological Administration, Beijing, CN

[42] Morgan State University, Baltimore, Maryland, US

Corresponding authors: A. Gaudel (audrey.gaudel@noaa.gov), O. R. Cooper (owen.r.cooper@noaa.gov)

report based on all available surface observations, the peer-reviewed literature and new analyses, and 2) Generate easily accessible and documented ozone exposure metrics at thousands of measurement sites around the world. Through the *TOAR-Surface Ozone Database* (https://join.fz-juelich.de, Schultz et al., 2017) these ozone metrics are freely accessible for research on the global-scale impact of ozone on climate, human health and crop/ecosystem productivity (*TOAR-Surface Ozone Database*, Schultz et al., 2017).

The assessment report is organized as a series of papers in a Special Feature of *Elementa: Science of the Anthropocene*. Three of the papers focus on the global distribution and trends of ozone relevant to different aspects of tropospheric ozone impacts, utilizing a range of ozone metrics described in the companion paper, *TOAR-Metrics* (Lefohn et al., 2018). *TOAR-Health* (Fleming et al., 2018) and *TOAR-Vegetation* (Mills et al., 2018) rely on ozone metrics drawn exclusively from the *TOAR-Surface Ozone Database* (Schultz et al., 2017). These metrics are of interest to scientists and policy-makers who wish to explore the impacts of ozone on human health and vegetation, impacts which typically occur during the warm spring and summer months. In contrast, this paper (hereinafter referred to as *TOAR-Climate*) presents seasonal surface ozone metrics that are designed to understand mean changes of ozone around the world, and that are appropriate for evaluating the global atmospheric chemistry models that calculate ozone's radiative forcing (Stevenson et al., 2013). In addition, *TOAR-Climate* summarizes ozone's global distribution and trends throughout the free troposphere using observations collected from ozonesondes, commercial aircraft, ground-based remote sensing instruments and satellite instruments, and presents the first intercomparison of the global tropospheric ozone burden from multiple satellite instruments. *TOAR-Climate* focuses on the period from the mid-1970s to the present when measurements from modern UV-absorption instruments are widely available. Further insight on ozone levels around the world from the late 1800s to the early 1970s, when ozone observations were much more limited and based on a variety of methods, is provided by *TOAR-Observations* (Tarasick et al., 2018). An assessment of the present-day capabilities of the global atmospheric chemistry models used to calculate tropospheric ozone's radiative forcing is provided by *TOAR-Model Performance* (Young et al., 2018).

1.2. Tropospheric ozone's relevance to climate

Due to its relatively short lifetime, tropospheric ozone is considered a 'near-term climate forcer', a class of compounds whose impact on climate occurs primarily within the first decade after their emission (IPCC AR5: Myhre et al., 2013). The influence of tropospheric ozone on climate is dependent on its radiative forcing (RF) which is the change in the Earth's energy flux since 1750 (due to changes of tropospheric ozone). The quantity of ozone in the troposphere in 1750 is unknown because observations in those days did not exist. The earliest quantitative observations only began in the late 1800s and even then these measurements suffered from interferences from other trace gases (see *TOAR-Observations*, Tarasick et al., 2018). In the absence of observations, global atmospheric chemistry models are relied upon to estimate ozone in 1750. Based on output from multiple models, tropospheric ozone's global-average radiative forcing is estimated to be 0.40 ± 0.20 W m^{-2} (IPCC, 2013). The relatively large error bars of ± 50% are due to uncertainties in the estimate of pre-industrial ozone levels (Forster et al., 2007; Gauss et al., 2006; Mickley et al., 2001; Young et al., 2013), and uncertainties in the present-day spatial distribution of tropospheric ozone (Gauss et al., 2003; Kiehl et al., 1999; Naik et al., 2005; Portmann et al., 1997; Stevenson et al., 2006; Wu et al., 2007). Ozone can also affect radiative forcing indirectly due to its impact on vegetation, carbon uptake (Sitch et al., 2007; Lombardozzi et al., 2015), and methane lifetime (West et al., 2007; Fiore et al., 2008).

Improvement to the estimate of ozone's radiative forcing requires greater confidence in global atmospheric chemistry model estimates of the tropospheric ozone burden (TOB: the total mass of ozone in the troposphere, Tg) in pre-industrial times, plus an accurate observation-based quantification of the present-day TOB and its horizontal and vertical distribution. The vertical distribution is especially critical because the relative greenhouse effect of ozone is greatest in the tropical and sub-tropical upper troposphere (UT), a region with limited ozone observations (Lacis et al., 1990; Forster and Shine, 1997; Berntsen et al., 1997; Worden et al., 2008, 2011; Gauss et al., 2003, 2006; Bowman et al., 2013; Stevenson et al., 2013; Kuai et al., 2017). Current global atmospheric chemistry models vary in their estimates of the quantity of tropospheric ozone originating from the stratosphere or from in situ photochemistry (Wu et al., 2007), but agree that photochemistry is the dominant gross source, exceeding the flux from the stratosphere by factors of 7–15 (Young et al., 2013; Banerjee et al., 2016). Most (~90%) of the ozone produced in the atmosphere is also destroyed through photochemical loss processes, with the remainder deposited to the surface, which on an annual basis is similar in magnitude to the flux from the stratosphere. These same models estimate that approximately 30% of the present-day TOB is attributable to human activity and that the average present-day tropospheric ozone lifetime is approximately 22 days (Young et al., 2013). Further details on the tropospheric ozone budget are described in the TOAR companion paper by Archibald et al. (2018), hereinafter referred to as *TOAR-Ozone Budget*.

In addition to changes of ozone precursor emissions, the quantity and distribution of tropospheric ozone is affected by unforced, low-frequency climate variability and long-term anthropogenic climate change (Jacob and Winner, 2009; Fiore et al., 2015; Barnes et al., 2016). Unforced climate variability refers to cyclical meteorological and transport patterns that affect tropospheric ozone at a particular location by modulating the frequency of air masses that are either enhanced or depleted in ozone, or by modulating cloud cover or air mass stagnation events which impact ozone photochemical production and loss.

Examples include El Niño/Southern Oscillation (Ziemke et al., 2015), the North Atlantic Oscillation (Eckhardt et al., 2003), the Quasi-Biennial Oscillation (Neu et al., 2014), the Pacific-North American pattern (Lin et al., 2014), and the frequency of synoptic scale heat-waves and mid-latitude cyclones (Mickley et al., 2004; Leibensperger et al., 2008; Shen et al., 2017). While climate variability produces interannual variability of observed ozone levels, anthropogenic climate change can produce forced long-term ozone trends. Many studies have examined the impacts of anthropogenic climate change on future tropospheric ozone levels and future ozone precursor transport pathways (Fiore et al., 2015 and references therein; Barnes et al., 2016; Shen et al., 2016; Doherty et al., 2017). The general ozone response in a warmer climate is an ozone reduction within air masses transported over long distances, due to an increase in water vapor and a decrease in ozone lifetime, but an ozone increase near the surface in regions where heat waves and air mass stagnation allow ozone precursors to accumulate. However, to elicit a strong ozone response in a future climate the simulations require relatively high global temperature increases associated with radiative forcings of 4.5 or 8.5 W m^{-2} and 50 to 100 years of climate change. On shorter timescales surface ozone trends due to anthropogenic climate change are difficult to detect as 20-yr ozone trends driven by unforced climate variability can be as large as those caused by changes in precursor emissions or anthropogenic climate change (Barnes et al., 2016; Garcia-Menendez et al., 2017). The longest continuous UV-absorption ozone records began in the mid-1970s and since then global temperatures have risen by approximately 0.7°C (Blunden and Arndt, 2017; NASA: www.columbia.edu/~mhs119/Temperature). Given the limited temperature increase so far over the span of the longest continuous surface ozone records, definitive attribution of observed global scale ozone changes due to anthropogenic climate change will likely require several more years of observations.

Previous assessments of tropospheric ozone have primarily focused on the processes that control ozone on the regional and global scale, and these works serve as a series of milestones in the scientific community's collective understanding of tropospheric ozone (National Research Council, 1992; Team N.S., 2000; Brasseur et al., 2003; The Royal Society, 2008; Monks et al., 2015). In contrast, *TOAR-Climate* assesses ozone's global distribution and trends from the mid-1970s to 2016, with the goal of providing a wide range of in situ and remotely sensed ozone observations for quantifying the present-day TOB and to evaluate the global atmospheric chemistry models that estimate pre-industrial and future-scenario tropospheric ozone. Accordingly, *TOAR-Climate* studies ozone variability measured at surface sites, but focuses on remote or non-urban sites because they are more easily compared to relatively coarse-scale global atmospheric chemistry models and because they are more broadly representative of regional-scale ozone. *TOAR-Climate* also explores ozone in the free troposphere (defined as the layer between the atmospheric boundary layer and the tropopause) as well as ozone in the full tropospheric column to quantify TOB and its vertical and horizontal distribution. Another unique aspect of *TOAR-Climate* is the intercomparison of several near-global ozone products derived from in situ observations and remote sensing. Many of these products, such as TCO from the OMI and IASI satellite-borne instruments, are quite new (Payne et al., 2017, Wespes et al., 2017) and are expected to form a key component of an evolving global ozone observational network (Burrows et al., 2011; Bowman, 2013). TOAR's emphasis on collaboration has provided an opportunity to compare these satellite products for the first time. The purpose of the intercomparison is to determine if the various products agree in their quantification of TOB, TCO or long-term trends. The most robust results can then be used for global atmospheric chemistry model evaluation as described in *TOAR-Model Performance* (Young et al., 2018).

The results of *TOAR-Climate* are presented as follows. Ozone metrics and statistics have been selected for their relevance to understanding average tropospheric conditions and for evaluating the global atmospheric chemistry models used to estimate pre-industrial and future ozone levels. The observations are from a wide range of instruments implementing in situ (surface ozone analyzers, aircraft-based instruments and ozonesondes) and remotely sensed techniques (ground-based Umkehr and FTIR, lidar and satellite), and are described in Section 2 and **Table 1**. The present-day global distribution of ozone at the surface, in the free troposphere and in the full tropospheric column is presented in Section 3. Trends in these same regions are presented in Section 4, with time series beginning anywhere from the mid-1970s (where data are available) to the year 2000, and extending through 2014, 2015 or 2016, depending on data availability. Finally, Section 5 discusses ozone trends or distributions in several regions of the world and describes how the datasets used in *TOAR-Climate* can be accessed.

2. Method

2.1. Surface ozone metrics relevant to climate and global model evaluation

TOAR-Metrics (Lefohn et al., 2018) describes all of the ozone metrics in the TOAR database. The metrics relevant to climate and global atmospheric chemistry model evaluation that were selected for *TOAR-Climate* are: 1) the seasonal daytime average (8:00 to 20:00 local time) for surface observations, 2) seasonal nighttime averages (20:00 to 8:00 local time) at mountaintop sites, 3) monthly and seasonal means for free tropospheric observations from commercial aircraft (IAGOS), ozonesondes and lidars, as well as for TCO retrievals from space and ground-based remote sensing instruments. In some instances 5^{th}, 50^{th}, 95^{th} and 98^{th} percentiles are also shown. The present-day period is defined as the 5-years between 2010 and 2014. Seasonal ozone values at surface sites are assessed for 2010–2014, with each site required to have at least three years of data during this 5-year period, and data capture of at least 75% in any season (Schultz et al., 2017). At a given surface site the magnitude of the temporal ozone trend is determined with the Theil-Sen (T-S) estimator, and the significance of the trend is determined with the

Table 1: All products discussed in this paper. DOI: https://doi.org/10.1525/elementa.291.t1

Product name and institution	Horizontal resolution of gridded products	Horizontal coverage	Vertical range (tropopause definition)	Temporal resolution/time of day	Record length
Satellite					
OMI/MLS *NASA GSFC*	1° × 1.25°	60°S–60°N	Surface to tropopause (WMO 2 K km^{-1} lapse-rate)	Monthly/ Seasonal 13:45	2004–2016, continuing
GOME & OMI *Smithsonian Astrophysical Observatory (SAO)*	1° × 1.25°	60°S–60°N	Surface to tropopause (WMO 2 K km^{-1} lapse-rate)	Monthly/Seasonal OMI: 13:45 GOME: 10:30	GOME: 1995–6/2003 OMI: 10/2004–2015, continuing
OMI-RAL *Rutherford Appleton Laboratory (RAL)*[1]	5° × 5°	60°S–60°N	Surface to 450 hPa mole fraction and surface to tropopause column (WMO 2 K km^{-1} lapse rate)	Monthly/ Seasonal 13:45	1995–2016, continuing
IASI-LISA *LISA*	Averaged over 0.25° × 0.25° grids	Regional (Asia)	Surface to 6 km and 6–12 km	Seasonal 9: 30	2008–2014, continuing
IASI+GOME-2 *LISA*	1° × 1°	Regional (Europe, Asia)	Surface to 3 km, and 3–9 km	Monthly/Seasonal 9:30	2009–2010
IASI – FORLI *Université Libre de Bruxelles and LATMOS/IPSL*	Averaged over 5° × 5° grids	90°S–90°N	Surface to tropopause (WMO 2 K km^{-1} lapse rate)	Seasonal 9:30	2008–2016, continuing
IASI – SOFRID *CNRS*	5° × 5°	80°S–80°N	Surface to tropopause (WMO 2 K km^{-1} lapse rate)	Seasonal 9:30	2008–2016, continuing
SCIAMACHY	Averaged over grids 1° × 1°, 2° × 2°, 5° × 5°	80°S–80°N	Tropopause to 60 km (blended tropopause)	Monthly 10:00	2002/08–2012/4
Ground-based instrument					
FTIR *NDACC*	Point location	Various sites around the world	Surface to 8 km a.s.l. in this analysis. Retrievals to 45 km are also possible	Monthly/Annual	Earliest data from 1995, continuing
Umkehr Umk04+stray light correction, NOAA processing	Point location	Various sites around the world	Surface to 250 hPa	Monthly/Annual Morning and afternoon profiles, averaged profile during measurements between 70–90° SZA, latitude and season dependent time of measurements	Earliest data from 1956 at Arosa, Switzerland, continuing
TOST	5° × 5°	90°S–90°N	Surface to tropopause (WMO 2 K km^{-1} lapse rate)	Seasonal/Annual	2008–2012
IAGOS	5° × 5° and airport location	Various airport in the world	surface to 12 km	Hourly (over Frankfurt) /Monthly /Seasonal	1994–2013
Lidar	Point location	2 sites (OHP-France, TMF-California USA)	3 to 14 km (OHP) 4 to 18 km (TMF)	Seasonal	1991–2015 (OHP) 1999–2014 (TMF)
TOAR surface ozone metrics	Point location	3136 non urban sites	sea level to mountain top	Seasonal	Most sites: 2000–2014 Selected sites: 1973–2017

[1] GOME-1, –2A and –2B data in preparation.

nonparametric Mann-Kendall (M-K) test, as described in *TOAR-Metrics* (Lefohn et al., 2018). Statistical significance is based on an α value of 0.05, and all trends are reported with 95% confidence intervals. For a site to qualify for the 2000–2014 trend analysis, it must have at least 12 years of data and not more than 2 years missing at either end of the interval. In addition, data capture must exceed 75% in any given season.

TOAR uses specific units when describing ozone observations and levels of exposure. When referencing an observation in ambient air, TOAR follows World Meteorological Organization guidelines (Galbally et al., 2013) and uses the mole fraction of ozone in air, expressed in SI units of nmol mol^{-1}. Under tropospheric conditions the nmol mol^{-1} is indistinguishable from the volumetric mixing ratio ppb. The same units are applied to any ozone statistic, such as median or 95th percentile values. In *TOAR-Health* (Fleming et al., 2018) and *TOAR-Vegetation* (Mills et al., 2018), the volumetric mixing ratio, ppb is used for the ozone exposure metrics discussed in those papers to maintain consistency with the ozone human health and vegetation research communities.

When referring to a TCO value, TOAR uses the Dobson unit (DU), where 1 DU is the number of molecules of ozone per square centimeter required to create a layer of pure ozone 0.01 millimeters thick at standard temperature and pressure (or 2.69×10^{16} ozone molecules cm^{-2}). The tropospheric column extends from the surface to the tropopause, which can be defined according to a variety of methods including temperature lapse rate, temperature cold point (tropical tropopause), trace gas thresholds or thermodynamic properties such as isentropic potential vorticity. The choice of tropopause definition varies between research groups and due to the differences in altitude between the various tropopause definitions, independently calculated TCO values for a given time and location can differ by several DU. Discrepancies in tropopause altitude are particularly common at mid-latitudes in the region of the subtropical jet stream (Bethan et al., 1996; Wirth, 2000; Rodriguez-Franco and Cuevas, 2013).

2.2. Regionally representative surface sites

The *TOAR-Surface Ozone Database* (Schultz et al., 2017) contains climate-relevant ozone metrics at hundreds of surface sites around the world, both urban and rural. For this analysis a subset of non-urban surface sites has been selected for the purposes of illustrating the spatial and temporal variability of regionally representative ozone around the globe and for straightforward comparison to global atmospheric chemistry models. Urban sites were not considered because in spatial terms they are not regionally representative and because the local emissions and photochemical and deposition processes are too small-scale to be resolved by global atmospheric chemistry models, as described by *TOAR-Model Performance* (Young et al., 2018). Sites were classified as urban if they exceeded thresholds for human population and satellite-detected nighttime lights intensity (see *TOAR-Surface Ozone Database* for a detailed description of the site classification algorithm, Schultz et al., 2017). This selection algorithm was applied to objectively identify the most highly urbanized sites, with approximately one quarter of all sites in the database classified as urban. The non-urban sites considered in this paper include suburban sites as well as rural sites surrounded by heavily urbanized areas. At the other extreme, some of the sites are considered to be remote, either located in unpopulated coastal regions, on islands, on top of high mountains, or in low-elevation, land-locked areas remote from anthropogenic emissions.

Another subset of sites was selected to explore long term trends in air masses characteristic of the lower free troposphere. This subset consists of eight mountaintop or very high elevation sites in the Northern Hemisphere. One of these sites, Mauna Loa Observatory (MLO) on the Big Island of Hawaii in the central North Pacific Ocean (19.5°N, 155.6°W, 3397 m), receives further analysis because of its location at the northern edge of the tropics. MLO is impacted by mid-latitude air masses which originate to the north and west and tropical air masses that originate to the south and east (Harris and Kahl, 1990; Oltmans et al., 2006). Ozone is typically greater in the mid-latitude air masses and the long term trend at MLO is affected by the relative frequency of air mass transport from high and low latitudes in response to climate variability driven by ENSO and the Pacific Decadal Oscillation (Lin et al., 2014). To reduce the noise in the trend due to climate variability we apply a new method for examining ozone trends at MLO (Ziemke and Cooper, 2017). Co-located dewpoint observations are used to separate the ozone observations into dry air samples, representative of mid-latitude air masses from higher altitudes and higher latitudes, and moist air samples, representative of tropical air masses from lower latitudes and lower altitudes. The dry/moist classification is performed for each month of the 1974–2016 time series using only nighttime data to avoid times with upslope winds. Each month must have at least 50% nighttime data availability. Dry air masses are those with a dewpoint value less than the monthly climatological 40th percentile, while moist air masses are those with a dewpoint value greater than the monthly climatological 60th percentile. A dry or moist category in any given month must have a sample size of at least 24 individual hourly nighttime observations.

2.3. Tropospheric ozone profiles: Ozonesondes, TOST, IAGOS, lidar

2.3.1. Ozonesondes

Ozonesondes are the most important source of vertically-resolved tropospheric ozone data for long-term climate studies due to their very long record, with regular soundings beginning in the early 1960s (Hering, 1964; Hering and Borden, 1964, 1965, 1967; Komhyr and Sticksel, 1967a, b; Attmannspacher and Dütsch, 1970). Using KI-based electrochemical detection methods similar to those developed for surface monitoring, they show good accuracy and reasonable stability over a 50-year period (Tanimoto et al., 2015; *TOAR-Observations*, Tarasick et al., 2018), and provide vertical resolution of about 100 m. Ozonesondes can be launched under cloudy conditions and therefore are not biased towards clear-sky conditions. Ozonesonde data are particularly valuable in the upper

troposphere-lower stratosphere (UTLS) region, especially in the tropics where much of the UT is not sampled by instrumented commercial aircraft. The UTLS is not highly-resolved by satellite instruments either.

However, ozonesonde data are temporally sparse and unevenly distributed, with only about 60 sites worldwide making regular soundings, most only once per week. Therefore *TOAR-Climate* uses a derived product that addresses these issues by taking advantage of the long lifetime of ozone in the free troposphere. This product is known as the Trajectory-mapped Ozonesonde dataset for the Stratosphere and Troposphere (TOST) and is described in Section 2.3.2. Ozone observations at individual ozonesonde sites, for example, Lauder, New Zealand, are only assessed by *TOAR-Climate* for the purposes of evaluating remotely sensed TCO.

2.3.2. TOST

The Trajectory-mapped Ozonesonde dataset for the Stratosphere and Troposphere (TOST) is a 3-dimensional, long-term ozone dataset derived from ozone soundings using a trajectory-based ozone mapping methodology (Tarasick et al., 2010; Liu, G. et al., 2013; Liu, J. et al., 2013). TOST is derived from over 67,000 ozonesonde profiles at over 100 stations from the 1960s to 2010s. Locations of these stations for the period 2008–2012 are shown in Figure S-1. The Hybrid Single-Particle Lagrangian Integrated Trajectory (HYSPLIT) model (Draxler and Hess, 1998), driven by the National Centers for Environmental Prediction (NCEP) reanalysis data, is applied to extend each ozone record along its trajectory path forward and backward for four days, as ozone lifetime in the free troposphere is a few weeks. Then, all ozone values along these trajectory paths are binned into grids of 5° × 5° × 1 km (latitude, longitude, and altitude), from sea level or ground level up to 26 km. TCO is integrated from the ozone concentrations below the tropopause, which is defined by the NCEP reanalysis data (**Table 1**). TOST provides a more accurate ozone distribution than simple linear or polynomial interpolation of ozonesonde data. It depends on neither a priori data nor photochemical modeling and reveals ozone variations in three dimensions. It covers a longer term and higher latitudes than some satellite-derived tropospheric ozone data. TOST has been evaluated by comparing with individual ozonesondes (removed from TOST one by one). The agreement is generally quite good. Biases are larger near the tropopause, over mountainous regions and in areas with sparse soundings.

2.3.3. IAGOS

The In-Service Aircraft for the Global Observing System (IAGOS) program conducts long-term observations of atmospheric trace gases, aerosols and cloud particles on the global scale using commercial aircraft of internationally operating airlines. The origins of IAGOS lie with the MOZAIC (Measurements of OZone and water vapor on Airbus In-service airCraft) program, in which as many as five long-range Airbus A340 commercial aircraft provided in-situ measurements of ozone (as well as other species and thermodynamic parameters) along their flight routes in various regions of the world (Marenco et al., 1998). Initiated in August 1994, MOZAIC continuously measured tropospheric vertical profiles (landing and takeoff phase) and monitored the UTLS (cruise phase), until November 2014. Ozone measurements were performed using a dual-beam ultra violet (UV)-absorption monitor (time resolution of 4 seconds) with an accuracy estimated at about ± (2 nmol mol^{-1} +2 %) (Thouret et al., 1998). As the successor to MOZAIC, with the objective of long-term sustainable operations, the first IAGOS aircraft became operational in July 2011 (Petzold et al., 2015; Nédélec et al., 2015). As of 2017, eight IAGOS aircraft from six airlines (Air France, Lufthansa, China Airlines, Cathay Pacific, Iberia and Hawaiian Airlines) are in operation. The 4-year overlap of MOZAIC and IAGOS has demonstrated that the new system provides data with the same quality as the former, permitting the reliable calculation of temporal trends from 1994 to the present (Nédélec et al., 2015). The MOZAIC-IAGOS data record (referred to as IAGOS hereafter) now contains over 50,000 flights, freely available through the open-access central database (http://www.iagos.org). In this study, we use IAGOS data averaged in 5° × 5° grids in the UT and profiles over USA, Europe and Asia (**Table 1**).

2.3.4. Lidar

Differential Absorption Lidar (DIAL) is a well-known technique to measure tropospheric and stratospheric ozone. The two DIAL systems described below contribute routine measurements 2–4 times per week to the Network for the Detection of Atmospheric Composition Change (NDACC).

The DIAL system located at the Observatoire de Haute Provence, France (OHP, 44°N, 6°E, 690 m) has operated since 1991 (Ancellet et al., 1997). The instrument measures ozone between 3 and 14 km above sea level (a.s.l.) with a vertical resolution ranging from 200 m at 2 km to 1000 m at 12 km. Precision remains within 9% at all altitudes, and accuracy is 5 ± 5 nmol mol^{-1}. For this analysis, the lidar data set is combined with data from Electrochemical Concentration Cell (ECC) ozonesondes launched weekly from OHP. Because the number of lidar profiles is 2 to 3 times higher than the number of ECC profiles, the combination of both data sets improves the trend estimate obtained in the yearly ozone trend analysis (Gaudel et al., 2015).

The second DIAL used here is the tropospheric ozone lidar operated since 1999 at the Jet Propulsion Laboratory Table Mountain Facility in California (McDermid et al., 2002). The measurements cover altitudes between 4 and 18 km with an effective vertical resolution between 150 m and 3 km. Starting in 2006, the profile range was extended to 25 km by using a channel from a co-located water vapor lidar (Leblanc et al., 2012). The standard uncertainty is 5–10% throughout most of the profile, increasing to 15% at the top (Granados-Muñoz and Leblanc, 2016; Leblanc et al., 2016a).

2.4. Tropospheric Column Ozone from the ground

2.4.1. Ground-based FTIR

Observations from solar viewing ground-based Fourier Transform Infrared (FTIR) instruments are taken within the framework of the Network for the Detection of

Atmospheric Composition Change (NDACC, www.ndacc.org) and conform with the guidelines set by the Infrared Working Group (IRWG, https://www2.acom.ucar.edu/irwg). They achieve a spectral resolution of 0.005 cm^{-1} or better. The ozone retrievals are performed using the 10μ spectral region and described in Vigouroux et al., 2015. Using the Optimal Estimation technique (Rodgers, 2000), up to 5 independent layers (or degrees of freedom of signal, DOFS) can be resolved to 45 km (see *TOAR-Observations*, Tarasick et al., 2018). There is at least one tropospheric layer (to 8 km a.s.l.), as defined as having DOFS of 0.8 to 1.0, depending on the station. This ozone partial column has expected random and systematic uncertainties of 11% and 4%, respectively (see *TOAR-Observations*, Tarasick et al., 2018). The dominant systematic uncertainty are spectroscopic parameters. The total uncertainty is nominally 14%.

Among the NDACC FTIR stations, a subset provides time-series longer than 10 years (up to 23 years) for ozone trend studies (Vigouroux et al. 2008; García et al., 2012; Vigouroux et al., 2015; WMO, 2010; WMO, 2014). A list of the stations used in *TOAR-Climate* is provided in *TOAR-Observations* (Tarasick et al., 2018). The observations are limited to clear sky daytime conditions, which excludes the polar night observations for the highest latitude stations. For all stations the average number of measurements is 2.5, 7, and 15 per day, week and month, respectively, but with high variability depending upon station location.

2.4.2. Umkehr Dobson and Brewer ozone profile retrievals

Dobson (Dobson, 1968a, 1968b) and Brewer spectrometers (Kerr et al., 1981) are capable of ozone profile retrievals from zenith sky measurements (so-called Umkehr curve method, Mateer, 1964; Mateer and DeLuisi, 1992; Petropavlovskikh et al., 2005). Details of the method and ozone uncertainties are discussed in *TOAR-Observations* (Tarasick et al., 2018). Tropospheric ozone variability captured by the Umkehr method is determined by relative contributions of the a priori information and the measurement. The AK describes the mapping of the vertically distributed sensitivity of the measurement into the retrieved ozone profile. Although the tropospheric Umkehr layer is defined between the surface and 250 hPa, a small but non-negligible contribution from the lower stratosphere has to be taken into account. Therefore, attribution of the lowest Umkehr layer information to TCO (below the tropopause) variability is not well-defined and can be influenced by ozone variability in the lower stratosphere. The bias between Umkehr and other measurements, including ozonesondes and lidar has been identified (Komhyr et al, 1995; Fioletov et al., 2006; Nair et al., 2011). The bias between ozonesondes and Umkehr in the troposphere (~10–20%) is reduced by almost half when the ozonesonde profiles are smoothed with the Umkehr AKs. Correction for the out-of-band stray light error reduces the bias by about 5% (Petropavlovskikh et al., 2011), and the Umkehr tropospheric ozone data for this study are treated for stray light error (ftp://aftp.cmdl.noaa.gov/data/ozwv/DobsonUmkehr/Stray%20light%20corrected/). The data have been deseasonalized prior to trend analysis.

2.5. Tropospheric Column Ozone from Space

TOAR-Climate provides an intercomparison of several remotely sensed TCO products, as measured by satellite-borne instruments: OMI (Ozone Monitoring Instrument)/MLS (Microwave Limb Sounder), GOME (Global Ozone Monitoring Experiment) and OMI-SOA (Smithsonian Astrophysical Observatory), OMI-RAL (Rutherford Appleton Laboratory), IASI (Infrared Atmospheric Sounding Interferometer)-FORLI (Fast Optimal Retrievals on Layers), IASI-SOFRID (SOftware for a Fast Retrieval of IASI Data), IASI-LISA (Laboratoire Interuniversitaire des Systèmes Atmosphériques), IASI+GOME-2, and SCIAMACHY (SCanning Imaging Absorption SpectroMeter for Atmospheric CHartographY). Details of each product are described below with key parameters listed in **Tables 2** and **3**.

As for ground-based remote sensing (section 2.4), satellite data rely on retrieval algorithms that model the expected measured radiance with a forward model and then invert this model using the measurement, usually with optimal estimation (Rodgers et al., 2000), to produce an estimated vertical distribution of abundance (nmol mol^{-1}) or sub-columns (DU) along with a posteriori error covariance and averaging kernel (AK) matrices. The AK quantifies the relative sensitivity of the radiance and retrieval to the "true state" for vertical retrieval layers and varies with observation type (land/ocean, day/night), the spectral range being measured (thermal infrared or UV), spectral resolution, measurement noise and choice of a priori covariance. For example, OMI/MLS, OMI-SOA, IASI-FORLI and IASI-SOFRID are more sensitive to the UT, while OMI-RAL is more sensitive to the lower half of the troposphere (Figures S-2, S-3 and S-4). In this report, we have taken care to use common parameters, where possible, such as tropopause height to determine TCO. However, fundamental differences remain due to the different measurement techniques and retrieval algorithms. Algorithm implementation details in addition to the choice of a priori, such as the choice of spectroscopic data and other forward model parameters can also have significant impacts on the retrievals, even for the same measurements using the same inversion technique (Liu et al., 2007; Liu et al., 2013). Finally, satellite ozone retrievals from various instruments differ due to sampling strategy, both spatially and diurnally (see **Table 1**).

2.5.1. OMI/MLS

Daily measurements of TCO and tropospheric ozone mean mole fraction were determined from the NASA Aura satellite's OMI v8.5 total ozone (http://disc.sci.gsfc.nasa.gov/Aura/data-holdings/OMI) and MLS v3.3 stratospheric column ozone (SCO) (Livesey et al., 2011). Calculation of TCO (Ziemke et al., 2006) requires subtraction of MLS SCO from OMI total ozone (TO) for near clear-sky scenes (OMI radiative cloud fractions less than 30%) yielding a 1° latitude × 1.25° longitude gridded product. SCO was first calculated along orbit paths using standard vertical pressure integration of MLS ozone mole fraction profiles from 0.0215 hPa to the tropopause pressure (determined from NCEP reanalyses using the WMO 2 K km^{-1} lapse-rate definition). Daily SCO measurements were interpolated hori-

Table 2: Characteristics associated with IASI products used in this study. DOI: https://doi.org/10.1525/elementa.291.t2

	IASI-SOFRID	IASI-FORLI	IASI-LISA	IASI+GOME-2 (LISA)
Spectral range	1025–1075 cm^{-1}	1025–1075 cm^{-1}	7 wavelengths in [975–1100 cm^{-1}]	7 in [980–1070 cm^{-1}] 2 in [290–345 nm]
RTM[a]	SOFRID/ RTTOV	FORLI	KOPRA-KOPRAFIT	KOPRA VLIDORT
Retrieval method	OEM[a]	OEM[a]	Altitude dependent TP[a]	Altitude dependent TP[a]
A priori	Obs.[a] in 2008: Ozonesondes MOZAIC-IAGOS MLS	McPeters et al. (2007)	McPeters et al. (2007)	McPeters et al. (2007)
Tropopause Calculation	Based on temperature profile from ECMWF analysis (WMO thermal definition[a])	Based on IASI temperature from Eumetsat Level-2 products (WMO thermal definition[a])	No use of tropopause height estimation	No use of tropopause height estimation
Vertical range	Surface to tropopause	Surface to tropopause	surface to 6 km 6 to 12 km	surface to 3 km
Cloud filter	20%	13%	15%	30%
Pressure level of peak of vertical sensitivity	500–400 hPa	~ 500 hPa	700–540 hPa	800–700 hPa
Reference	Barret et al. (2011)	Boynard et al. (2016, 2017), Hurtmans et al. (2012)	Dufour et al. (2012)	Cuesta et al. (2013)

[a] RTM: Radiative Transfer Model; OEM: optimal estimation method; TP: Tikhonov-Philips; Obs.: Observations; WMO thermal definition: the thermal tropopause is defined as the lowest level at which the lapse rate is 2K km^{-1} or less, provided also that the average lapse rate between this level and all higher levels within 2 km does not exceed 2K km^{-1} (WMO, 1957).

zontally (Gaussian + linear) between orbit paths to obtain gridded SCO fields at the 1° × 1.25° horizontal resolution of OMI, and then subtracted from the gridded OMI total ozone to derive daily gridded TCO fields.

Biases and long-term stability of OMI and MLS ozone measurements have been evaluated in detail (e.g. Hubert et al., 2016; Schenkeveld et al., 2016). OMI/MLS TCO calibration was tested here against ozonesondes and screened for cross-instrumental drift issues including the OMI row anomaly error (http://www.knmi.nl/omi/research/product/rowanomaly-background.php). A small drift correction of –0.5 DU-$decade^{-1}$ and a small offset correction of +2 DU was applied to this TCO product. The OMI/MLS tropospheric ozone mass burden calculated for 60°S–60°N was an average of 291 Tg in year 2004 and 306 Tg for 2016, a statistically significant net increase of about 5%.

2.5.2. GOME and OMI (SAO)

Ozone profiles with 24 layers (~2.5 km thick) from the surface to 60 km are retrieved from Global Ozone Monitoring Experiment (GOME; Burrows et al., 1999) and OMI (Levelt et al., 2006) radiances in the Hartley and Huggins bands using the optimal estimation technique (Liu et al., 2005, 2007, 2010; Huang et al., 2017). NCEP daily tropopause height based on the WMO 2 K km^{-1} lapse-rate definition is used as one of the retrieval levels, allowing TCO, with its retrieval errors, to be derived from the retrieved profiles. The time series from GOME (7/1995–6/2003) and OMI (10/2004–2015) are combined to produce a nearly 20-year record. GOME data prior to March 1996 are systematically higher due to a shorter integration time and are not used in this study. To generate monthly GOME and OMI data to a common grid of 1° latitude × 1.25° longitude, only retrievals with good quality flags under near clear-sky conditions (with effective cloud fraction < 0.3) were used.

The individual retrieval TCO errors due to precision and smoothing errors are typically within 2–5 DU (14% on average), and average total errors including other systematic and forward model errors are estimated to be ~21%. Both GOME and OMI TCOs typically show good agreement with ozonesonde TCO to within 3 DU. However, accurate radiometric calibration of Level 1b data as a function of time is critical to producing a long-term consistent data record. The degradation correction in GOME data might cause time-dependent systematic biases in the retrievals and no time-dependent correction is applied to OMI data even during the occurrence of the serious row anomaly since 2009. In addition, small GOME/OMI biases are expected due to some small algorithm differences and different overpass times. As shown in Figure S-5, the time

Table 3: Characteristics associated with OMI and SCIAMACHY products used in this study. DOI: https://doi.org/10.1525/elementa.291.t3

	OMI/MLS	GOME-OMI	OMI-RAL	SCIAMACHY
Spectral range	OMI: UV-1: 270–314 nm UV-2: 306–380 nm MLS: 240 GHz radiances	GOME: 289–307 nm 325–340 nm OMI: 269–309 nm 312–330 nm	UV-1: 266–307 nm UV-2: 323–336 nm	326–335 nm 264–675 nm
RTM	TOMRAD	VLIDORT	Modified GOME-TRAN++	SCIATRAN
Retrieval method	LNM[a]	OEM[a]	OEM[a]	LNM[a]
A priori	Ozonesondes SAGE/MLS (McPeters et al., 2007)	McPeters et al. (2007)	McPeters et al. (2007)	Nadir: TOMS V7 ozone profile shape climatology (Wellemeyer et al., 1997) Limb: Climatology generated with a chemical transport model (McLinden et al., 2000)
Tropopause Calculation	Based on temperature from NCEP Reanalysis (WMO thermal definition[a])	Based on temperature from NCEP Reanalysis (WMO thermal definition[a])	Based on temperature from ERA-Interim Reanalysis (WMO thermal definition[a])	Based on temperature and potential vorticity from ECMWF reanalysis, ERA-Interim (Both WMO thermal and dynamical definition[a])
Vertical range	Surface to tropopause	Surface to tropopause	Surface to tropopause	Surface to tropopause
Cloud filter	30%	30%	20%	30%
Pressure level of peak of vertical sensitivity	~500–300 hPa	~600 hPa	~800 hPa	
Reference	Ziemke et al. (2006)	Liu et al. (2005, 2007, 2010) Huang et al. (2017)	Miles et al. (2015)	Ebojie et al. (2014)

[a]RTM: Radiative Transfer Model; OEM: optimal estimation method; LNM: Limb-Nadir-Match; WMO thermal definition: the thermal tropopause is defined as the lowest level at which the lapse rate is 2K km^{-1} or less, provided also that the average lapse rate between this level and all higher levels within 2 km does not exceed 2K km^{-1} (WMO, 1957); Dynamical definition: the dynamical tropopause is characterized by a sharp gradient in potential vorticity (PV). The value used in the paper to define the tropopause is for PV = 2 pvu.

series of GOME and OMI retrievals show clear systematic biases as some similar temporal patterns occur for different latitude bands, even though the seasonal variations are expected to be different (Liu et al., 2005, 2007, 2010; Huang et al., 2017).

2.5.3. OMI-RAL

Global height-resolved ozone distributions spanning the stratosphere and troposphere are retrieved from satellite UV nadir sounders by the RAL's optimal estimation scheme (Miles et al., 2015). Data sets spanning 1995–2016 are being produced from a series of five instruments for ESA's Climate Change Initiative (CCI) and will be updated in coming years for the EU's Copernicus Climate Change Service (C3S). RAL's scheme was the first to demonstrate tropospheric sensitivity (Munro et al., 1998). This is achieved through a three-step approach: firstly, the strong wavelength dependence of ozone absorption in the Hartley band (260–307 nm) is exploited in fitting the ratio of backscattered to direct-sun spectra to retrieve height-resolved information principally in the stratosphere; secondly, an effective surface albedo is retrieved in the 335–340 nm interval and, thirdly, temperature dependent ozone absorption in the Huggins bands (323–334 nm) is fitted to high precision (<0.1% RMS) to extend the profile retrieval into the troposphere. Ozone prior information for the first step is from a zonal mean monthly climatology (McPeters et al., 2007). Retrieval outputs from the first and second steps improve the prior constraints for the third step. Precision on the 1013–450 hPa layer retrieved from an individual sounding is typically ~4 DU. This requires key instrument spectral and radiometric parameters to be pre-retrieved from direct-sun spectra and some instrumental and geophysical parameters to be co-retrieved with the ozone profile. The on-line forward-model is a modified version of GOMETRAN (Rozanov et

al., 1997). Developments since Miles et al. (2015) include: height-dependent treatment of rotational Raman scattering in ozone absorption lines and modifications for OMI's 2-D detector array in place of across-track scanning by GOME-class sensors. Spectral coverage in the Huggins bands has also been extended to 321.5–334 nm. Developments are in progress to improve near-surface sensitivity through addition of the ozone visible band (Chappuis) and, for GOME-2 on Metop, improvement of UTLS vertical resolution by addition of co-located IR measurements by IASI. The scheme as adapted for OMI will be applied to Sentinel-5 Precursor, launched in 2017, and subsequently to Sentinel-5 on Eumetsat's Metop-SG series, planned for 2021–40.

2.5.4. IASI

IASI is a nadir viewing Fourier transform spectrometer that sounds the Earth-atmosphere system in the thermal infrared region. It operates from the Metop satellite series (Metop-A launched in 2006 and Metop-B launched in 2012) and provides global distributions twice a day for numerous trace gases (e.g. Clerbaux et al., 2009; Hilton et al., 2012). Four IASI ozone products are described below.

IASI-FORLI: Ozone vertical profiles are retrieved on the global scale in near real time with the FORLI-O_3 (for IASI–v20151001) processing chain set up by the Université Libre de Bruxelles (U.L.B.) and LATMOS teams (Hurtmans et al., 2012). FORLI-O_3 relies on a fast radiative transfer and on the optimal estimation method and provides profiles on a uniform 1 km vertical grid on 41 layers from the surface. FORLI-O_3 uses only one single a priori profile and variance-covariance matrix which are built from a climatology. The code is implemented in the Eumetsat ground-based facility to become the official IASI ozone product to be distributed by Eumetcast in 2017. The FORLI-O_3 product has undergone a series of validations against independent measurements (e.g. Boynard et al., 2018). The sensitivity of IASI in the troposphere maximizes around 4–8 km for most scenes. Negative ozone trends in the troposphere at mid-high northern latitudes have been reported, especially in summer (Wespes et al., 2018). For the present study, the daily tropopause height used to generate the IASI-FORLI TCO dataset relies on the WMO definition applied to the IASI level 2 temperature profiles provided through the Eumetcast operational processing system (August et al., 2012). Only daytime and clear-sky measurements characterized by a good spectral fit have been considered. Similar to other products, the IASI data were mapped on a daily basis to a grid of 5° latitude × 5° longitude, and then averaged to produce seasonal and annual means.

IASI-SOFRID: SOFRID retrieves global ozone (Barret et al., 2011) and CO (De Wachter et al., 2012) profiles from IASI radiances. SOFRID is built on the RTTOV (Radiative Transfer for TOVS) operational radiative transfer model (Saunders et al., 1999, Matricardi et al., 2004) jointly developed by ECMWF, Meteo-France, UKMO and KNMI within the NWPSAF. The RTTOV regression coefficients are based on line-by-line computations performed using the HITRAN2004 spectroscopic database (Rothman et al., 2005) and the land surface emissivity is computed with the RTTOV UW-IRemis module (Borbas et al., 2010). We use the IASI-L2 temperature profiles from EUMETSAT for radiative transfer computation. The retrievals are performed with the UKMO 1D-Var algorithm (Pavelin, et al., 2008) based on the optimal estimation method (Rodgers, 2000). The results presented here are based on the IASI-SOFRID v1.5 ozone product (Barret et al., 2011). In this data version, SOFRID uses a single a priori ozone profile and associated covariance matrix based on one year (2008) of ozonesondes from the WOUDC network. The retrievals are performed for clear-sky conditions (cloud cover fraction < 20%). IASI-SOFRID ozone retrievals enable almost independent retrievals in the lower-middle troposphere (below 225 hPa), the UTLS (225–70 hPa) and the stratosphere (above 70 hPa) (Barret et al., 2011). Dufour et al. (2012) have shown that IASI-SOFRID ozone tropospheric columns were in good agreement with coincident ozone columns from ozonesondes for the year 2008, with correlation coefficient of 0.82 (0.93) and 4 ± 4% at mid-latitudes and 5 ± 3% in the tropics.

IASI-LISA: The retrieval of the IASI-LISA ozone vertical profiles is performed using the radiative transfer model KOPRA (Karlsruhe Optimised and Precise Radiative transfer Algorithm), its inversion module KOPRAFIT, and a Tikhonov-Phillips (TP) altitude-dependent regularization (Eremenko et al., 2008). The retrieval constraints are optimized to enhance sensitivity in the lower troposphere (Dufour et al., 2012). Three different a priori profiles and constraint matrices are used depending on the tropopause height (for polar, midlatitude and tropical situations; see Dufour et al., 2015). Two semi-independent partial columns of ozone can be determined between the surface and 12 km (especially in the case of positive thermal contrasts): the lower-tropospheric column, integrating the ozone profile from the surface to 6 km a.s.l.; the upper-tropospheric column, integrating the ozone profile from 6–12 km a.s.l. (Dufour et al., 2010, 2012). The lower-tropospheric column has a maximum sensitivity between 3 and 4 km with a limited sensitivity at the surface (Dufour et al., 2012). The retrieval algorithm is not optimized to provide near-real-time global data, and at present only regional data above Europe and Asia are available. For this study, only morning observations for clear-sky conditions (cloud fraction less than 15%) and high-quality pixels (based on quality flags) are used. The IASI-LISA product was mapped on a daily basis to a grid of 0.25° latitude × 0.25° longitude, and then averaged to produce seasonal means over the 2008–2014 period.

IASI+GOME-2 (LISA): In order to better characterize the vertical distribution of tropospheric ozone down to the lowermost troposphere (LMT, surface to 3 km a.s.l.), a new multispectral approach called IASI+GOME-2 combines the information provided by thermal IR radiances measured by the IASI instrument and Earth reflectance UV spectra from GOME-2 (Cuesta et al., 2013). Both co-located spectra are fitted simultaneously for deriving vertical profiles of ozone (for effective cloud cover < 0.3), providing multispectral retrievals at the IASI horizontal resolution (12-km diameter pixels spaced by 25 km at nadir). Both IASI and

GOME-2 are onboard the Metop satellites and they offer scanning capabilities with daily global coverage. Altitude-dependent Tikhonov–Phillips-type constraints optimize sensitivity in the lowermost troposphere, which exhibits a relative maximum around 2 to 2.5 km a.s.l. over land (where thermal contrast is positive). Further details are provided in *TOAR-Observations* (Tarasick et al., 2018). The multispectral synergism of IASI and GOME-2 enhances the vertical resolution of the retrieval so as to consistently resolve ozone levels in the lower/middle troposphere, the middle/upper troposphere and lower stratosphere. Since January 2017, global scale IASI+GOME-2 observations are routinely produced at the ESPRI French National data center (http://cds-espri.ipsl.fr) of the AERIS data center (http://www.aeris-data.fr) and will be available soon for the scientific community. For the current paper, the new capability of the recent IASI+GOME2 product is illustrated with the dataset available before 2017 (the year 2010 for East Asia and August 2009 for Europe).

2.5.5. SCIAMACHY

SCIAMACHY is a passive UV-Vis-NIR-SWIR spectrometer operated on board the European Envisat satellite from March 2002 to April 2012 (Burrows et al., 1995; Bovensmann et al., 1999). The instrument alternated between limb and nadir geometries so that the region probed during the limb scan was observed about 7 minutes later during the nadir scan. TOCs are retrieved applying the Limb-Nadir-Matching (LNM) technique (Ebojie et al., 2014; Ebojie, 2014; Jia et al., 2017) to coincident limb and nadir measurements from SCIAMACHY. Thereby, the total ozone columns are derived from nadir observations while the limb measurements are used to retrieve stratospheric ozone profiles. The latter are integrated down to the tropopause to obtain stratospheric ozone columns. TCO is calculated by subtracting the stratospheric ozone columns from its total column. The tropopause height was determined from the ECMWF ERA-Interim reanalysis, using a blended definition that transitions from a thermal tropopause definition in the tropics to a potential vorticity definition in the extra-tropics (Hoinke, 1998; Wilcox et al., 2012). As the lowermost altitude of the stratospheric O_3 profiles used in this study (V2.9) is 12 km, extrapolation using ozonesonde climatologies was performed where needed. Only cloud free limb scenes and nadir pixels with cloud fraction < 30% were used. The analysis was restricted to solar zenith angles smaller than 80° and to the descending part of the orbit. The total error of the TCO data is estimated to be about 5 DU and is dominated by the error of the stratospheric ozone column.

2.6. Satellite observations of tropospheric ozone as a greenhouse gas

TES (Tropospheric Emission Spectrometer) operated on the NASA EOS-Aura satellite from 2004 to 2018 and measured vertical ozone profiles using thermal infrared spectra, similar to IASI, using Fourier Transform Spectrometry (Beer et al., 2001). TES obtained global observations from 2004 to 2009 but shifted to a smaller latitude range following instrument failures associated with continuous operation. Seasonal mean TCO as measured by TES is shown for the years 2004–2008 in Figure S-6. Since IASI observations will continue into the next decade with identical IASI instruments on Metop-B and -C, there have been efforts to combine the TES and IASI data records by accounting for differences in spatial coverage, spectral resolution, and a priori information in the optimal estimation retrievals (Oetjen et al., 2014, 2016).

Radiative forcing due to tropospheric ozone has significant regional variability (Shindell and Faluvegi, 2009). While satellite observations cannot measure pre-industrial to present-day radiative forcing of tropospheric ozone, they can measure the ozone greenhouse effect of reduced TOA flux due to ozone radiance absorption. Long-wave (thermal infrared) measurements from TES and IASI are used to compute instantaneous radiative kernels (IRK) for ozone in W m^{-2} per nmol mol^{-1} for each vertical pressure level. IRKs are computed along with the retrieved ozone vertical profiles using the Jacobians, $\boldsymbol{K}$, which quantify the sensitivity of the TOA radiance to each vertical profile (Worden et al., 2008, 2011; Doniki et al., 2015). Multiplying the IRK by the tropospheric ozone profile and summing the values from the surface to the tropopause gives the long-wave radiative effect (LWRE) in W m^{-2}.

3. Present-day distribution of tropospheric ozone

3.1. Surface ozone

Non-urban surface ozone observations for the present-day (2010–2014) are mostly found in North America, Europe and East Asia (Korea and Japan); observations beyond these regions are relatively sparse. **Figure 1** shows daytime average surface ozone mole fractions at all available non-urban sites in December–January–February (DJF) and in June–July–August (JJA), the minimum and maximum seasons of ozone production in the NH mid-latitudes (note that many US sites only operate during April–September, hence the fewer number of sites in DJF). In NH winter (DJF) high ozone (>40 nmol mol^{-1}) is mainly confined to high elevation regions: western USA, Western Europe (Alps, Apennines and Pyrenees), central Japan, central China, Himalayas, Greenland, southern Algeria and Izaña (Canary Islands). Such high ozone values are less frequent at low elevations, limited to western Canada, southern California, northeastern Utah (in a region of intense oil and natural gas extraction (Oltmans et al., 2016)), Israel, islands in the Mediterranean Sea and island/coastal sites in the vicinity of South Korea, Japan, Hong Kong and Taiwan. During NH summer, high ozone values (>50 nmol mol^{-1}) are concentrated in northern mid-latitudes at both high and low elevations, primarily in the western USA, southern Europe, China, South Korea and Japan. Ozone in the SH is more difficult to assess due to the sparse data coverage. The available observations indicate that SH ozone is much lower than in the NH, with only one region (the high elevation Highveld of South Africa (Balashov et al., 2014)) exceeding 40 nmol mol^{-1}. These

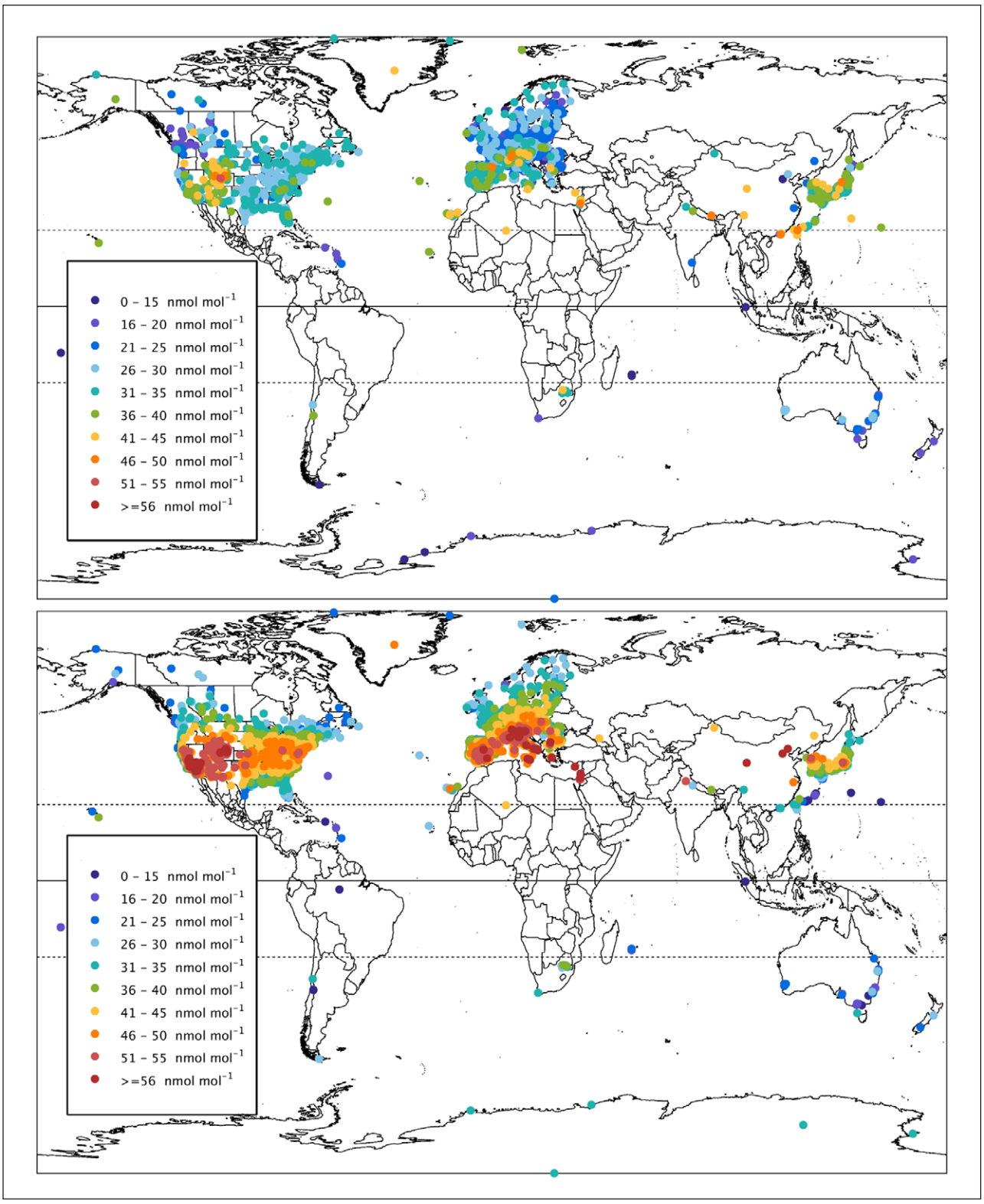

Figure 1: Present-day global daytime average ozone (nmol mol^{-1}). Global daytime average ozone (nmol mol^{-1}) at 2702 non-urban surface sites in December–January–February (top) and 3136 non-urban sites in June–July–August (bottom) for the present-day period, 2010–2014. DOI: https://doi.org/10.1525/elementa.291.f1

high ozone events occur in DJF, and also in September–October–November (SON), which is springtime and the peak ozone season in the SH.

Figures 2 and **3** focus on the three regions with dense surface networks (North America, Europe, East Asia) and show daytime averages for all four seasons. In each region, maximum ozone is observed in spring/summer and the minimum ozone is observed in autumn/winter. Notably, maximum ozone values in southeastern China, South Korea and Japan occur in spring, not summer. However, ozone in the Beijing region peaks in summer. Finally, to illustrate the distribution of extreme ozone values, Figure S-7 shows 98th percentile ozone at all available sites around the world (urban and non-urban) for the 6-month warm season (April–September in the NH, and October–March in the

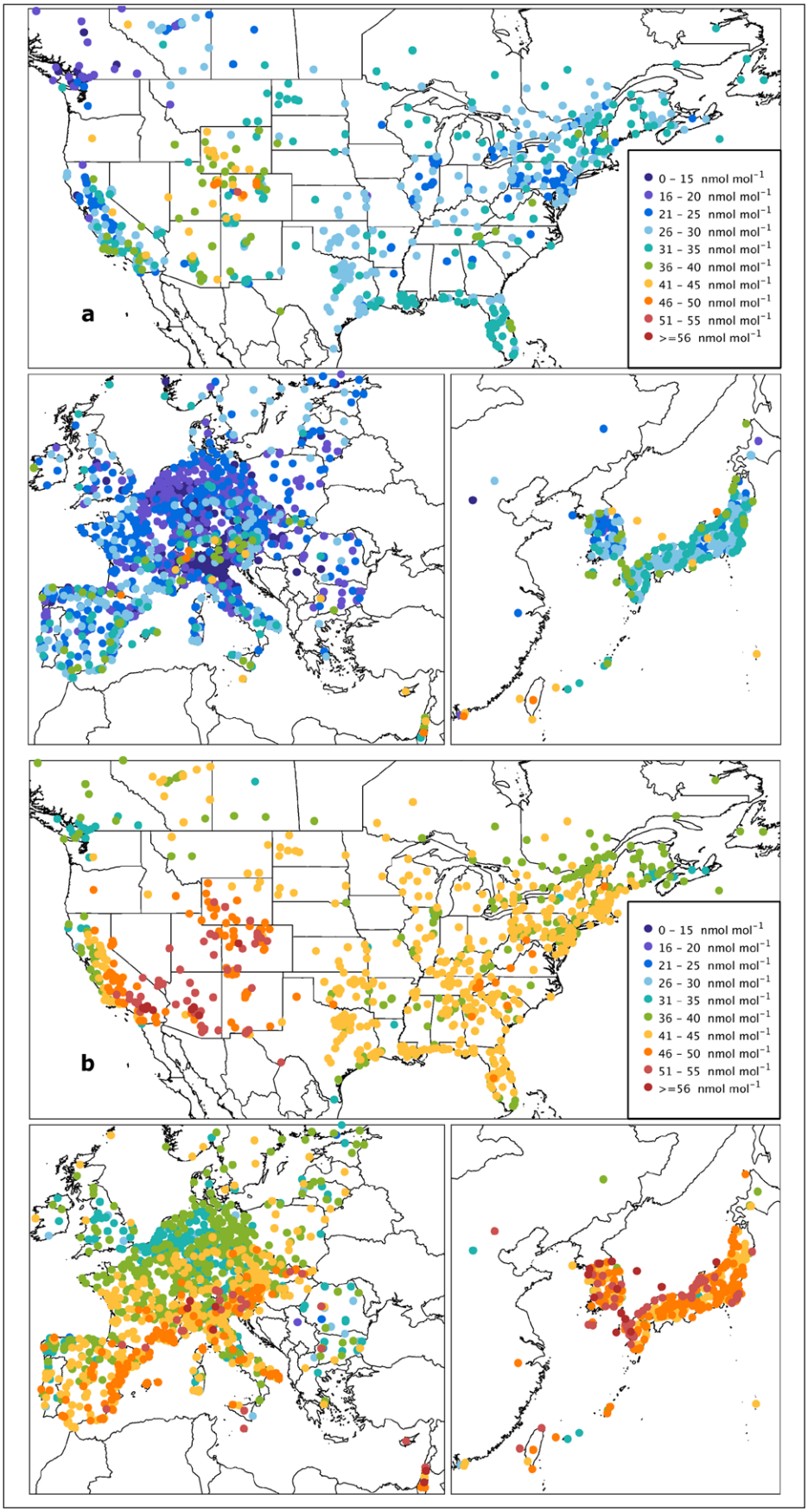

Figure 2: Present-day regional daytime average ozone (nmol mol^{-1}). Regional daytime average ozone (nmol mol^{-1}) at all available non-urban surface sites for December–January–February (DJF, **a**), March–April–May (MAM, **b**) for the present-day period, 2010–2014. Panel (a) shows the same data as Figure 1 (top), but focuses on the three regions with dense surface networks. DOI: https://doi.org/10.1525/elementa.291.f2

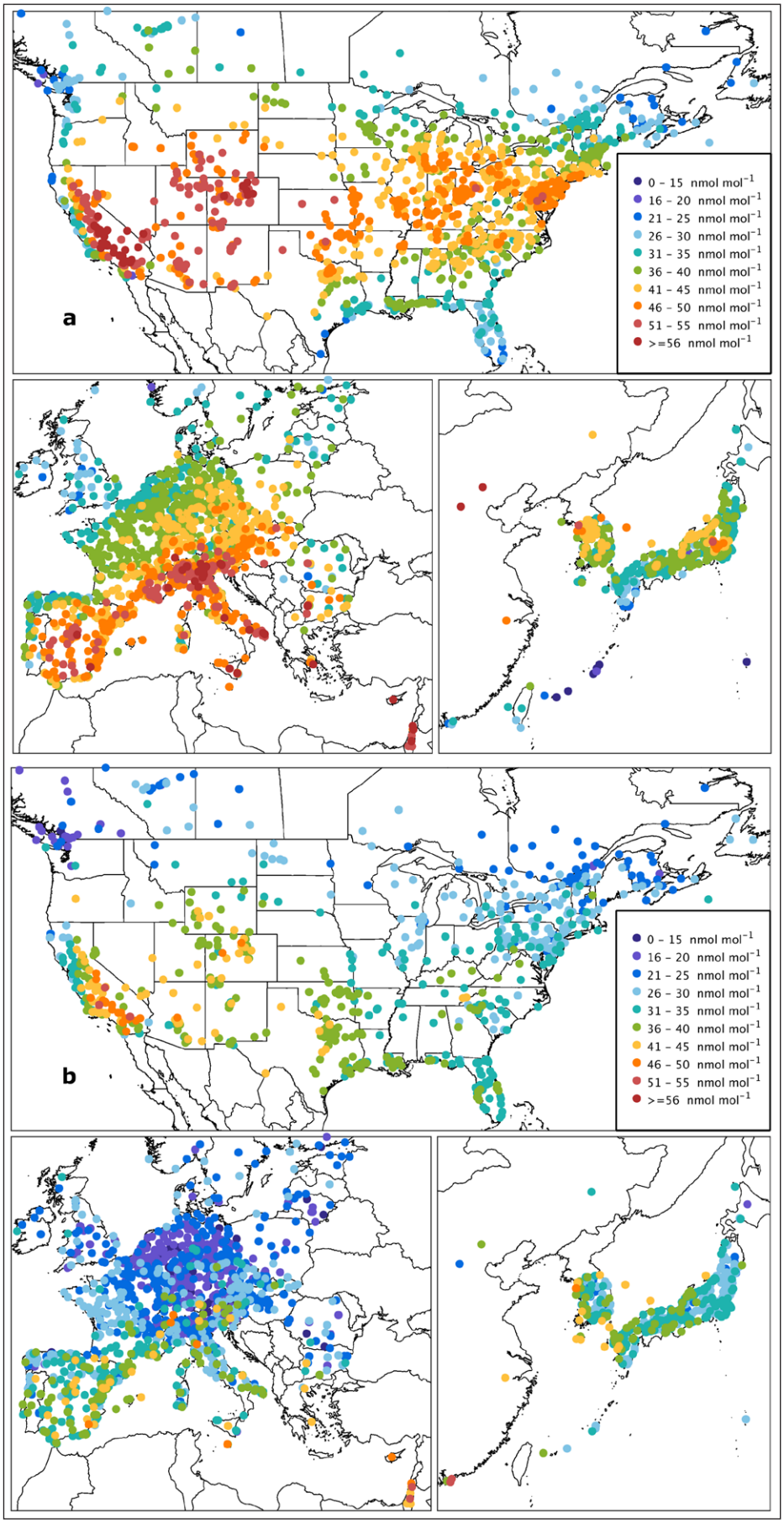

Figure 3: Present-day regional daytime average ozone (nmol mol^{-1}). As Figure 2 but for June–July–August (JJA, **a**) and September–October–November (SON, **b**). DOI: https://doi.org/10.1525/elementa.291.f3

SH). Greatest values in North America are found in California and Mexico City. Europe has a strong north-south gradient with highest values in northern Italy, Spain and Greece. On the eastern edge of the Mediterranean a monitoring site at 1 km a.s.l. in the West Bank has ozone values as great as those found in the heavily urbanized regions of Europe. Across Asia very high ozone values (>80 nmol mol^{-1}) are widespread (northern India, eastern mainland China, Hong Kong, Taiwan, South Korea, and Japan) despite a limited number of monitoring sites.

3.2. Free tropospheric ozone

3.2.1. Global ozone distribution in the free troposphere from aircraft and ozonesondes

Figures 4 and **5** show seasonal mean ozone in the UT as measured by IAGOS commercial aircraft and averaged using the methodology developed by Thouret et al. (2006). Measurements are obtained from aircraft cruising altitude (9–12 km a.s.l.), and cover a large portion of the NH mid-latitudes and tropics, and some areas of the SH.

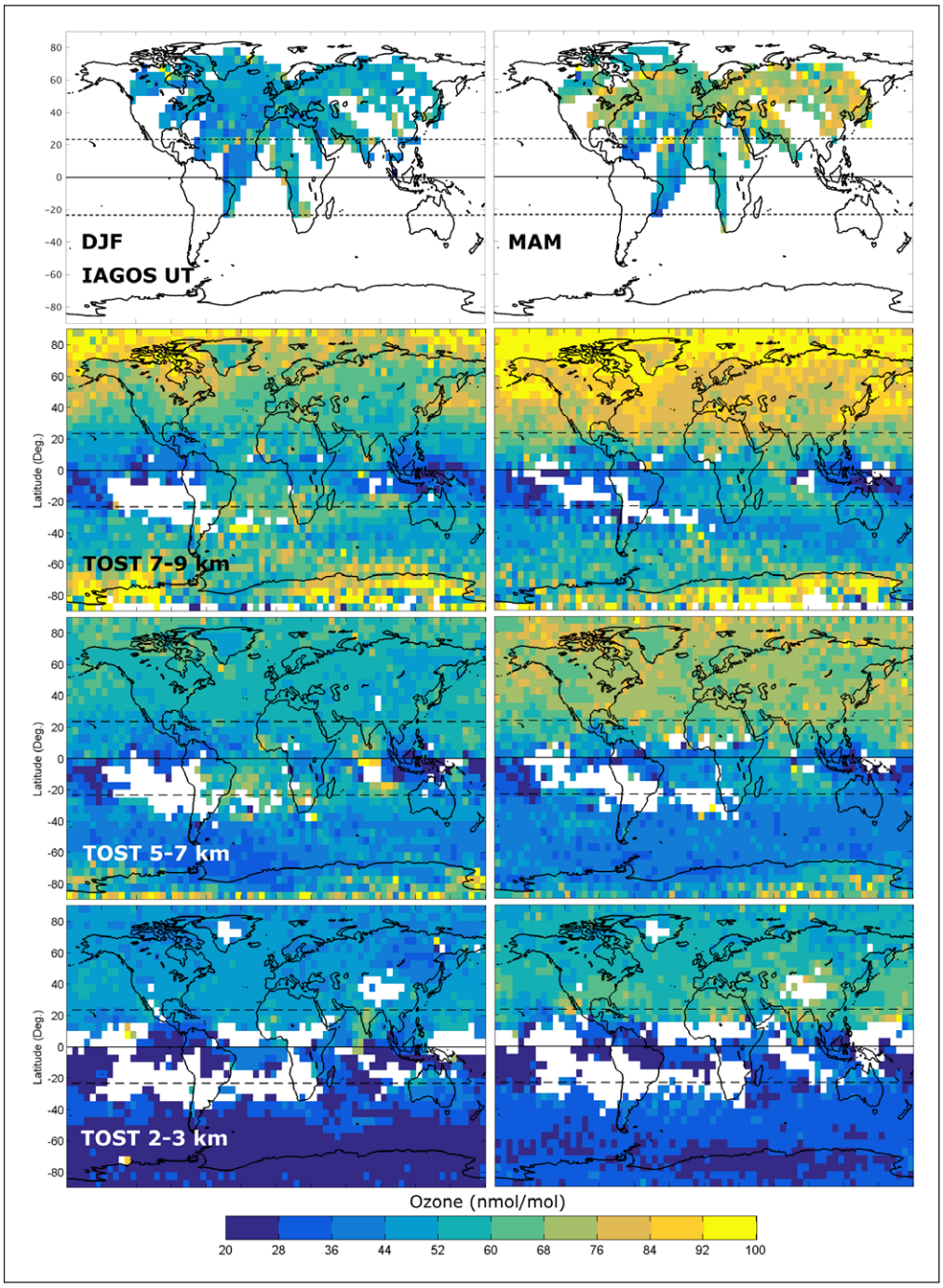

Figure 4: Seasonal mean ozone (nmol mol^{-1}) as measured by IAGOS commercial aircraft and by ozonesondes (TOST). Mean ozone (nmol mol^{-1}) at four levels in the free troposphere as measured by IAGOS commercial aircraft (2009–2013) at 9–12 km (UT), but below the dynamical tropopause (top row), and from ozonesondes (ozonesonde data from 2008–2012 spatially interpolated by trajectory-mapping in TOST) at 7–9 km (2nd row), 5–7 km (3rd row) and 2–3 km (bottom row). White areas indicate no data. Data are displayed seasonally for December–January–February (DJF, left) and March–April–May (MAM, right). DOI: https://doi.org/10.1525/elementa.291.f4

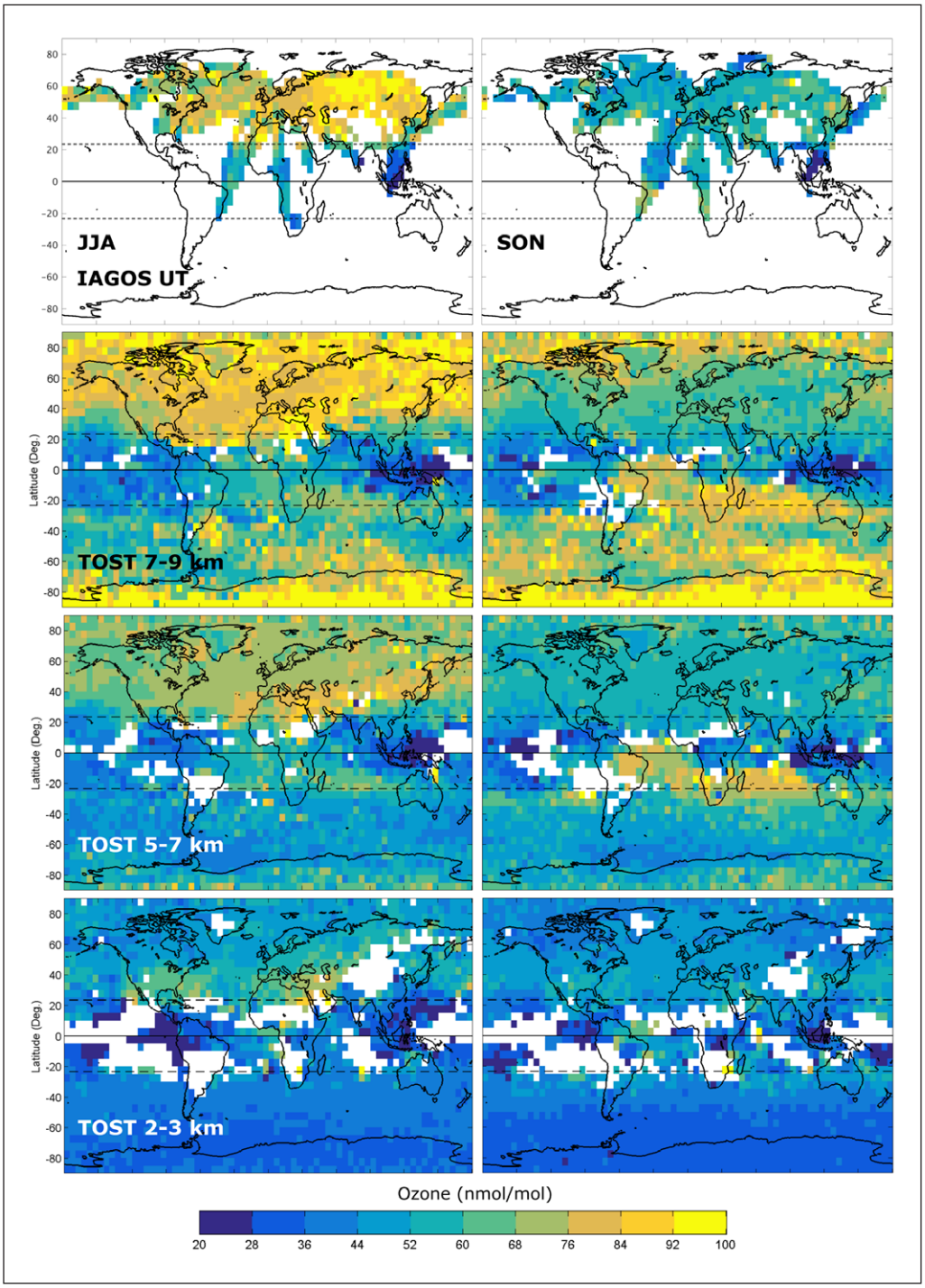

Figure 5: Seasonal mean ozone (nmol mol^{-1}) as measured by IAGOS commercial aircraft and by ozonesondes (TOST). As Figure 5 but for June–July–August (JJA, left) and September–October–November (SON, right). DOI: https://doi.org/10.1525/elementa.291.f5

In the extra-tropics (30°S–90°S and 30°N–90°N), the UT is considered to be a layer 15–75 hPa below the local tropopause, defined as the 2 pvu (pvu = potential vorticity units) potential vorticity surface extracted from the European Centre for Medium-Range Weather Forecasts (ECMWF) operational analyses and forecasts. In tropical regions (30°S–30°N), where the tropopause is typically above the aircraft cruising altitude, all observations above 8 km are assigned to the UT. Mean ozone is calculated on 5° × 5° cells containing at least 300 observations over the 2009–2013 period.

The seasonal distributions of ozone in the UT show a summer maximum that coincides with the maximum photochemical activity in the NH. Clear seasonal variations are highlighted in the northern extra-tropics, with maximum values (>100 nmol mol^{-1}) occurring in boreal summer, and minimum values in boreal winter (<60 nmol mol^{-1}). This is consistent with the seasonal pattern previously observed over Europe, eastern North America and the North Atlantic Ocean, based on 1994–2003 MOZAIC observations (Thouret et al., 2006). The highest ozone is observed over Eurasia (including the Middle East)

(>76 nmol mol^{-1}) and to a lesser extent over the North Atlantic Ocean and Europe, similar to the upper tropospheric ozone distribution observed by the TES satellite instrument (J. J. Liu et al., 2009). Intermediate values are measured above North America and the North Pacific Ocean, while lower values are found in the tropics (20–60 nmol mol^{-1}). Ozone is particularly low (20–40 nmol mol^{-1}) above Southeast Asia during boreal summer and autumn, likely due to deep convective uplift of low-ozone air masses (Ziemke et al., 2010; Cooper et al., 2013; Strode et al., 2017). While this analysis lacks observations above SE Asia during winter and spring, a recent IAGOS analysis of this region including observations through 2013 shows that upper tropospheric ozone peaks during the spring biomass burning season (40–50 nmol mol^{-1}) (Cohen et al., 2018). In the tropics, relatively high ozone is found above regions known to be impacted by biomass burning, particularly over South America in SON (Yamasoe et al., 2015), and West Africa in DJF (Sauvage et al., 2005).

Figures 4 and **5** also show seasonal mean ozone (nmol mol^{-1}) from the TOST ozonesonde climatology in the upper (7–9 km), mid- (5–7 km) and lower free troposphere (2–3 km). In comparison to the IAGOS UT climatology, the TOST 7–9 km layer generally has more ozone during DJF and MAM even though it is at a lower altitude. There are two reasons for this difference, 1) compared to IAGOS, ozonesondes are typically biased high by about 8% in the UT (*TOAR-Observations*, Tarasick et al., 2018); and 2) whereas the IAGOS product utilizes observations below the dynamical tropopause (defined as 2 pvu), TOST is based on the thermal (temperature lapse-rate) definition of the tropopause which is often located above the dynamical tropopause, with greater differences in the vicinity of the polar and subtropical jetstream (Bethan et al., 1996; Wirth, 2000). Therefore, TOST will often include additional ozone found between the thermal and dynamical tropopause at mid-latitudes, especially in winter and spring when jetstream activity is strongest. TOST shows a broad spring/summer ozone enhancement across northern mid-latitudes with a band of enhanced summertime ozone stretching from North Africa, across the Mediterranean Sea to East Asia at 5–7 km and 7–9 km. This broad feature has also been detected in the summertime UT by TES (Worden et al., 2009). The ozone enhancement above the eastern Mediterranean region and Middle East in summer appears to extend from the UT down to the lower free troposphere. Peak ozone in the SH occurs in the mid- and upper troposphere during SON (season of peak biomass burning), primarily in the tropics and subtropics stretching from South America eastwards across Africa and as far as Australia. The minimum ozone values at all three levels tend to occur over the tropical Pacific Ocean.

3.2.2. Diurnal variability

Frankfurt, Germany is the only location in the world where frequent IAGOS aircraft flights (21,000 for 1994–2012, i.e. 98 per month on average) are sufficient for building an almost complete diurnal profile of ozone throughout the depth of the troposphere (Petetin et al., 2016a). **Figure 6** shows the tropospheric ozone diurnal cycle during 1994–2012, at both the seasonal and annual scale, and at several pressure levels. Only observations within the troposphere are taken into account, although the methodology employed here includes fresh stratospheric intrusions. Based on ECMWF PV fields (see Section 3.2.1), the tropopause is defined as a 30 hPa layer centered on the 2 pvu potential vorticity surface. Data are binned by 3-hour time period, but the 0–3 UTC time period was omitted due to a small sample size.

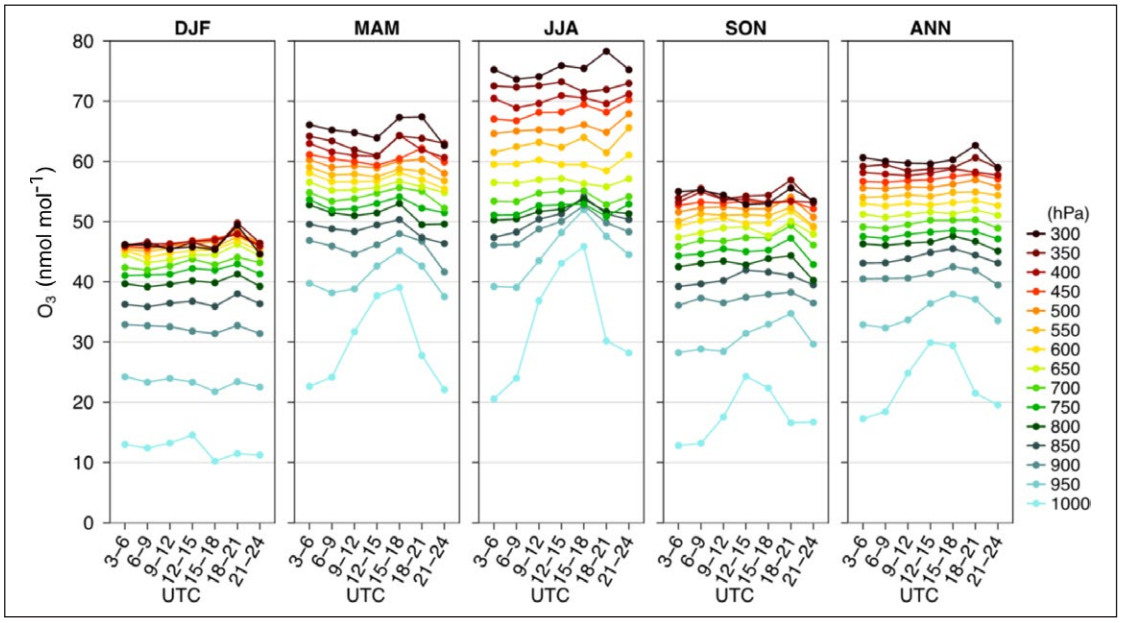

Figure 6: Diurnal variability of tropospheric ozone as measured by IAGOS commercial aircraft above Frankfurt. Diurnal variability of mean tropospheric ozone from the surface to the tropopause above Frankfurt between August 1994 and December 2012, by season and annually (ANN: annual). Reproduced with authorization from the authors of Petetin et al. (2016a). DOI: https://doi.org/10.1525/elementa.291.f6

In the boundary layer (BL), strong enhancements are observed during daytime. The coefficients of variation (standard deviation normalized by the mean) decrease from 10–30% close to the surface to less than 3% above 800 hPa. The figure clearly depicts the development of a deeper BL during summertime with ozone diurnal variations propagating up to 700 hPa (compared to 850 and 900 hPa in spring and autumn, respectively). In winter, the diurnal variation in the BL is very low due to limited photochemical activity. In the free troposphere, some fluctuations of ozone persist in the late afternoon and evening (15–24 UTC) in summer and autumn, likely due to the lower number of observations in comparison to the 3–15 UTC time interval. These results demonstrate the absence of ozone diurnal variations in the free troposphere and give evidence that all the free tropospheric products can be directly compared regardless of time of day.

3.3. Column ozone in the troposphere

3.3.1. Regional distribution of partial column ozone in the lower and upper troposphere

Figure 7 shows the seasonal means of two partial tropospheric ozone columns (surface-6 km and 6–12 km) over East Asia for 2010–2014 from IASI-LISA observations.

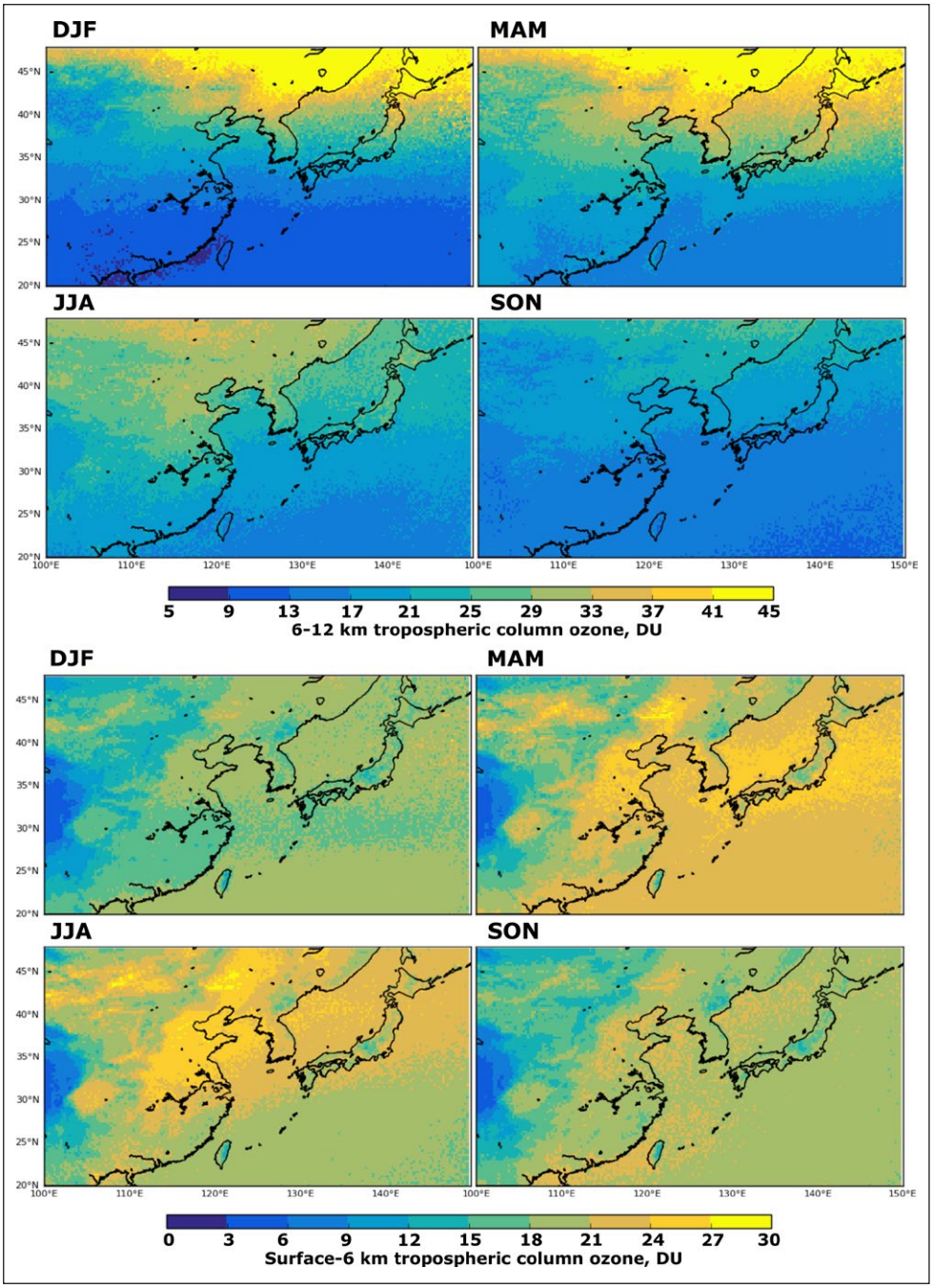

Figure 7: Seasonal mean partial ozone columns (DU) above East Asia from the IASI-LISA product for 2010–2014. Seasonal 6–12 km (top) and surface-6 km (bottom) partial ozone columns (DU) over East Asia, according to the IASI-LISA (TP) product for 2010–2014. The unit is in DU to be comparable with the other satellite products. DOI: https://doi.org/10.1525/elementa.291.f7

Ozone peaks in the upper layer north of 35°N in DJF (when the tropopause is lowest and this layer contains a greater amount of stratospheric air), and is at a minimum in SON. South of 35°N upper tropospheric ozone has a maximum in MAM with values almost as great as in JJA. In the lower troposphere ozone generally peaks in MAM, in agreement with surface observations and with TOST, except in the Beijing region where surface observations peak in JJA (**Figures 2** and **3**). Previous analysis of IASI observations has shown that the springtime maximum in the lower troposphere above East Asia has contributions from stratosphere-to-troposphere transport and from regional photochemical ozone production (Dufour et al., 2015). Ozone diminishes from MAM to JJA at low latitudes when the summer Asian monsoon advects ozone-depleted tropical air northwards (Dufour et al., 2010; Safieddine et al., 2016), but the decrease is not as pronounced as the seasonal cycle observed at surface sites in the same region (**Figures 2** and **3**).

Focusing on the year 2010 (currently available data), **Figure 8** illustrates the new capability of IASI+GOME-2 to provide the average mole fraction of ozone in the LMT (up to 3 km asl). The seasonal patterns from this remotely sensed product match the patterns revealed by the surface observational network (**Figures 2** and **3**), with ozone peaking in spring above southeastern China, South Korea and Japan, but peaking in summer above the Beijing region. The excellent spatial coverage of this LMT product shows that the surface summertime ozone peak observed with in situ measurements in the Beijing region extends across North and East China, where the atmospheric boundary layer typically reaches depths of 2 km (Ding et al., 2008). In absolute values, LMT ozone mole fractions derived from IASI+GOME-2 are 7 nmol mol^{-1} greater than surface observations, as expected due to the column integration of higher ozone values often found above the surface (Ding et al., 2008). The seasonal evolution of LMT ozone observed by IASI+GOME-2 and averaged over the region 30–43°N, 110–129°E (confined to the land areas of eastern China and South Korea in 2010) also agrees well with IAGOS aircraft profiles, within 1–5 nmol mol^{-1} in winter, spring and summer (Figure S-8).

Figure 9 shows an illustration over Europe (August 2009) of the new observations of ozone in the LMT (up to 3 km asl) derived from IASI+GOME-2. Similar to the surface observations (**Figures 2** and **3**) high ozone is observed across southern Europe and the Mediterranean basin in the LMT. High ozone is also observed in the mid-troposphere (Safieddine et al., 2014), in agreement with TOST (**Figures 4** and **5**). Downward transport from the stratosphere may contribute to the enhanced mid-tropospheric ozone over the North Atlantic Ocean (Wespes et al., 2012, Škerlak et al., 2014).

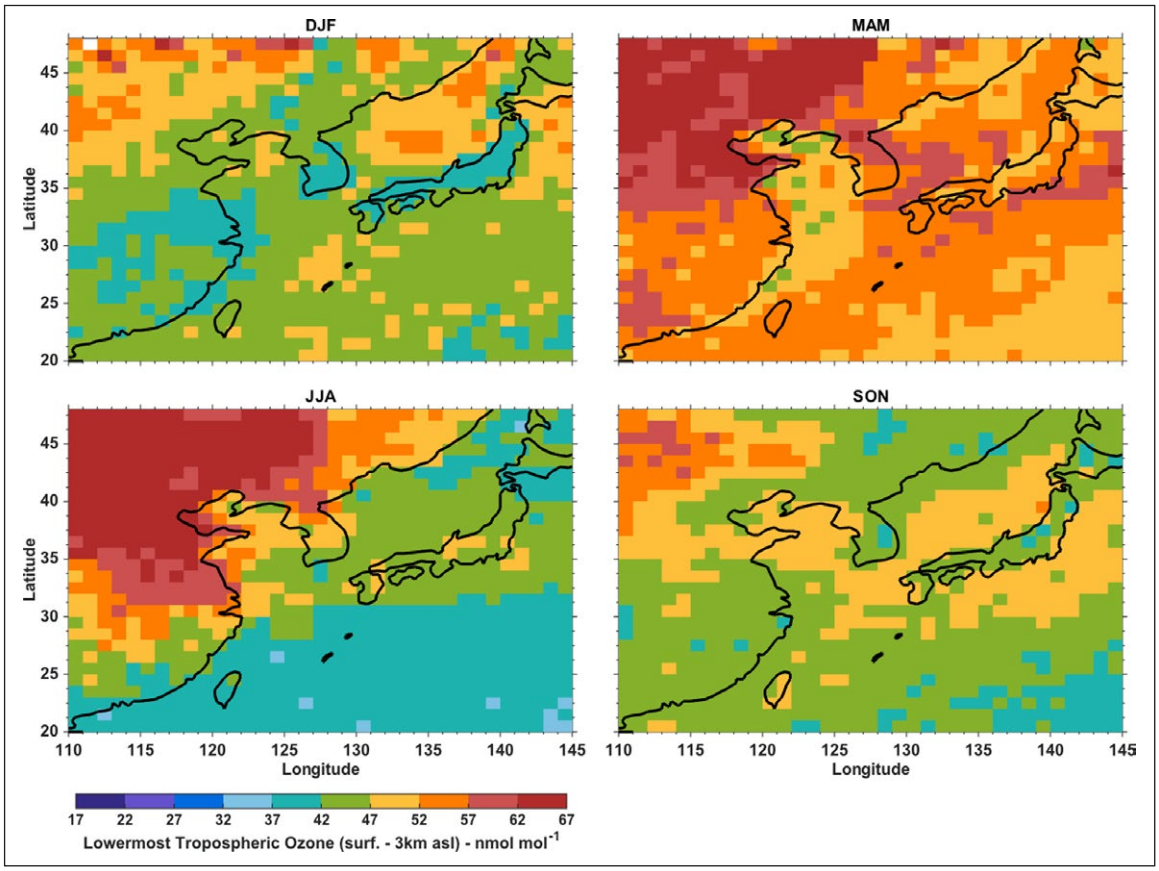

Figure 8: Seasonal mean lowermost tropospheric ozone (nmol mol^{-1}) above East Asia from IASI+GOME-2 product for 2010. IASI+GOME-2 (LISA) seasonal (2010) average ozone mole fraction (nmol mol^{-1}) over East Asia from the surface to 3 km. Horizontal resolution is 1° × 1°. The unit is nmol mol^{-1} to be comparable with surface observations. DOI: https://doi.org/10.1525/elementa.291.f8

3.3.2. Global distribution of tropospheric column ozone

Figure 10 shows TOST yearly mean TCO for the period 2008–2012 (top left panel), with similar plots for all four seasons shown in Figure S-9. TOST shows that the strongest TCO values are found in the NH subtropics, stretching from the Gulf of Mexico to eastern Africa, with the

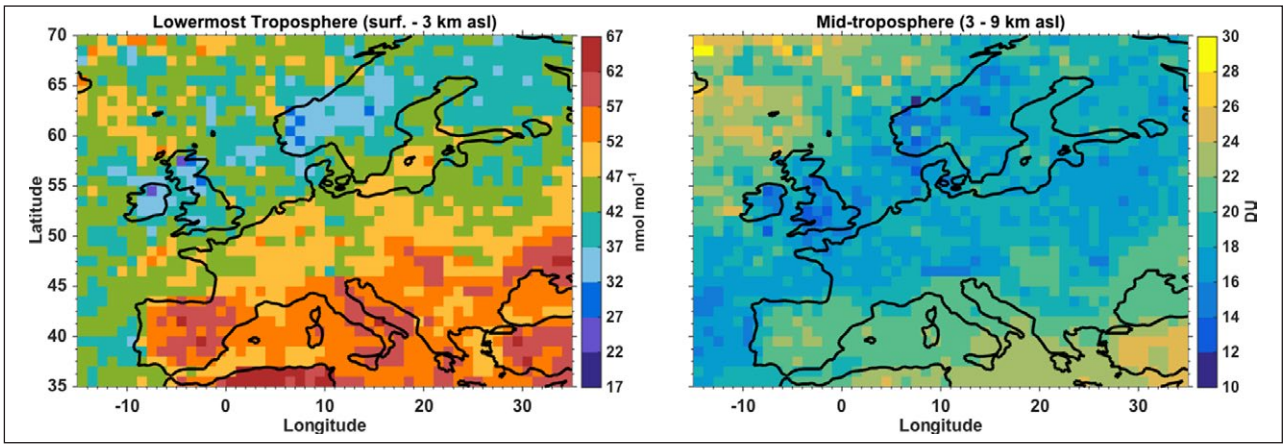

Figure 9: Monthly mean ozone above Europe from IASI+GOME-2 product for August 2009. IASI+GOME-2 (LISA) monthly average (August, 2009) mixing ratio (nmol mol^{-1}) from the surface to 3 km (left) and partial column ozone (DU) from 3 to 9 km (right) over Europe. Horizontal resolution is 0.5° × 0.5° and the data are smoothed using a horizontal moving average of 1.5°. DOI: https://doi.org/10.1525/elementa.291.f9

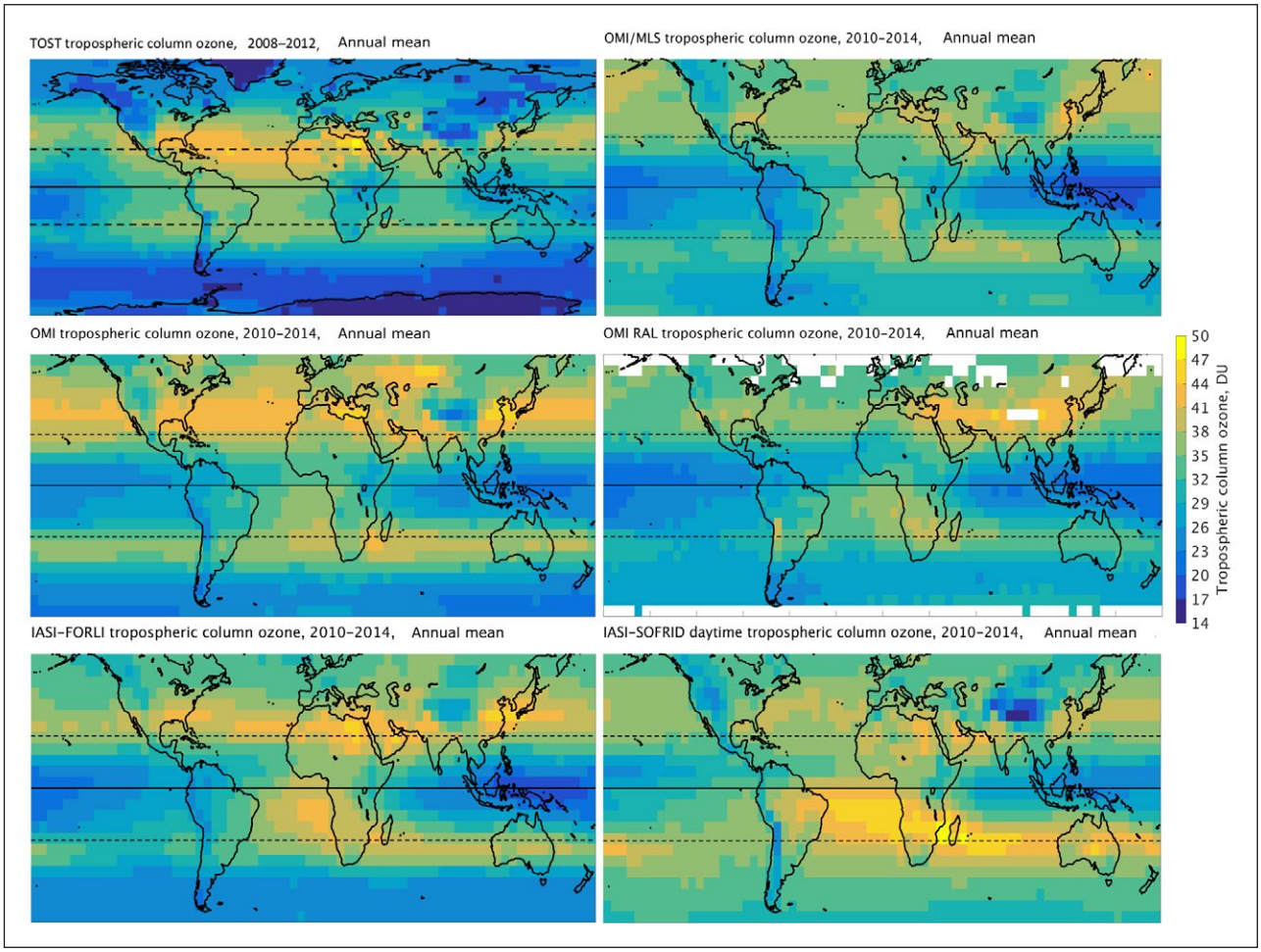

Figure 10: Maps of annual mean TCO (DU) from five satellite products and ozonesondes (TOST). Annual mean tropospheric column ozone (TCO) in Dobson unit (DU) as measured by TOST (top left), OMI/MLS (top right), OMI-SAO (middle left), OMI-RAL (middle right), IASI-FORLI (bottom left) and IASI-SOFRID (bottom right). The data are averaged over the period January 2010 through December 2014 and reported at 5° × 5° horizontal resolution, except for TOST, which covers the period 2008–2012. DOI: https://doi.org/10.1525/elementa.291.f10

maximum above Egypt. The seasonal plots show that the Egyptian maximum is strongest in JJA and is part of a broad enhancement that covers much of North Africa, the eastern Mediterranean region and the Middle East. The ozone enhancement above North Africa is due to extrapolation of the TOST values by trajectories and there are no independent ozone profiles above this region to evaluate this regional maximum. However, a large region of enhanced ozone above North Africa and the Middle East was detected by TES in July 2005 (J.J. Liu et al., 2009). The ozone maximum above the eastern Mediterranean has also been observed by IAGOS aircraft which show this feature to be the strongest in the NH mid-latitudes during JJA (Zbinden et al., 2013); further discussion of this feature can be found in Section 5.6. Other notable NH enhancements are found above northern Mexico (peak in MAM and JJA), the southeastern USA (peak in JJA), India and SE Asia (peak in MAM), the mid-latitude North Pacific Ocean (peak in MAM), much of the North Atlantic Ocean (Equator to 50°N with a peak in JJA), and the Arabian Sea (peak in MAM). The peak above India in MAM has been independently confirmed by a previous study (Lal et al., 2014). In the SH ozone peaks are lower than in the NH by roughly 10–20% and are confined to the tropics and subtropics above the South Atlantic Ocean and the South Indian Ocean. Peak seasonal TCO values in the SH are found above the South Indian Ocean from southern Africa to western Australia during SON, which is the SH peak season for biomass burning and stratosphere-to-troposphere transport (van der Werf et al., 2010; Fishman et al., 1991; J. Liu et al. 2016, 2017).

The remaining five panels in **Figure 10** show annual average TCO from five different satellite products, all for the period 2010–2014, which is more recent than the data currently available from the TOST product. Seasonal TCO maps for the satellite products are shown in Figures S-10–S-14. As discussed in Section 5.7 each satellite product follows a different method for retrieving ozone, resulting in different sensitivities to ozone in the lower, mid- and upper troposphere. Therefore, specific TCO features, such as the minimum above Indonesia or the enhancement over East Asia, display varying magnitudes across the five products. In the following we highlight the features that are common to the five satellite remote-sensing products and compare them to the in situ observations interpolated by TOST:

1) During DJF the satellite products tend to show a weak enhancement across the northern subtropics with a relative maximum above the Arabian Sea and western and northern India. TOST shows an ozone maximum in the same general region but its peak values of 41–44 DU are 3–6 DU greater than the satellite products.
2) During MAM TOST shows an ozone enhancement across Mexico and the Caribbean (44–47 DU), with a weaker extension across the North Atlantic Ocean. This feature is also detected by the satellites, but it is shifted further north by 5–10 degrees. Some products have similar TCO values while others are 3–6 DU less. During this season TOST also sees a broad enhancement stretching from North Africa across southern Asia into the western North Pacific Ocean, with a peak over northern India and southern China (47–50 DU). The satellites see this same general feature but with more distinctive enhancements above northern India and eastern China. We note that satellite observations, especially in the thermal infrared, have issues retrieving accurate TCO values over deserts because the associated albedo and reflection are not well-represented in radiative transfer codes.
3) During JJA all five satellite products show an ozone maximum at 30°–40°N above Asia. This feature also extends westward across the Mediterranean and the North Atlantic Ocean towards the eastern USA, but the relative intensity of this extension varies between products. TOST also sees enhanced ozone from the eastern USA eastwards across Asia, but it shows distinctive maxima above the eastern USA and the region from North Africa to the Middle East. The TOST maximum over North Africa extends southwards into the tropics, a feature not seen by any of the satellite products.
4) In the SH during JJA TOST sees enhanced ozone from Brazil across the South Atlantic Ocean and extending across southern Africa, Madagascar and the South Indian Ocean towards Australia. These same features are even stronger during SON with peak values of 41–44 DU above Madagascar. The satellite products show the same general pattern but with peak values 3–6 DU greater.

4. Global trends of tropospheric ozone

Several studies and reviews are available in the literature that describe the observational evidence for global increases of tropospheric ozone over the course of the 20th century. *TOAR-Observations* (Tarasick et al., 2018) provides a synthesis of these results and the reader is referred to this paper for a description of surface ozone observations prior to the 1970s. In this section, we focus on ozone trends since the 1970s.

4.1. Surface ozone trends

Spatially, global surface ozone trends are highly variable depending on time period, region, elevation and proximity to fresh ozone precursor emissions. We first examine long-term trends at mountaintop sites and focus on nighttime (20:00–8:00 local time) data when the stable atmosphere isolates the mountaintop from the air masses below, yielding ozone observations that are largely representative of the lower free troposphere (Price and Pales, 1963). There are eight mountaintop sites in the NH with data available through 2015 that can be examined for long-term nighttime ozone trends indicative of the lower free troposphere (**Table 4** and **Figure 11**). Long term trends at these important sites have been reported several times in recent years (Parrish et al., 2012, 2013, 2014;

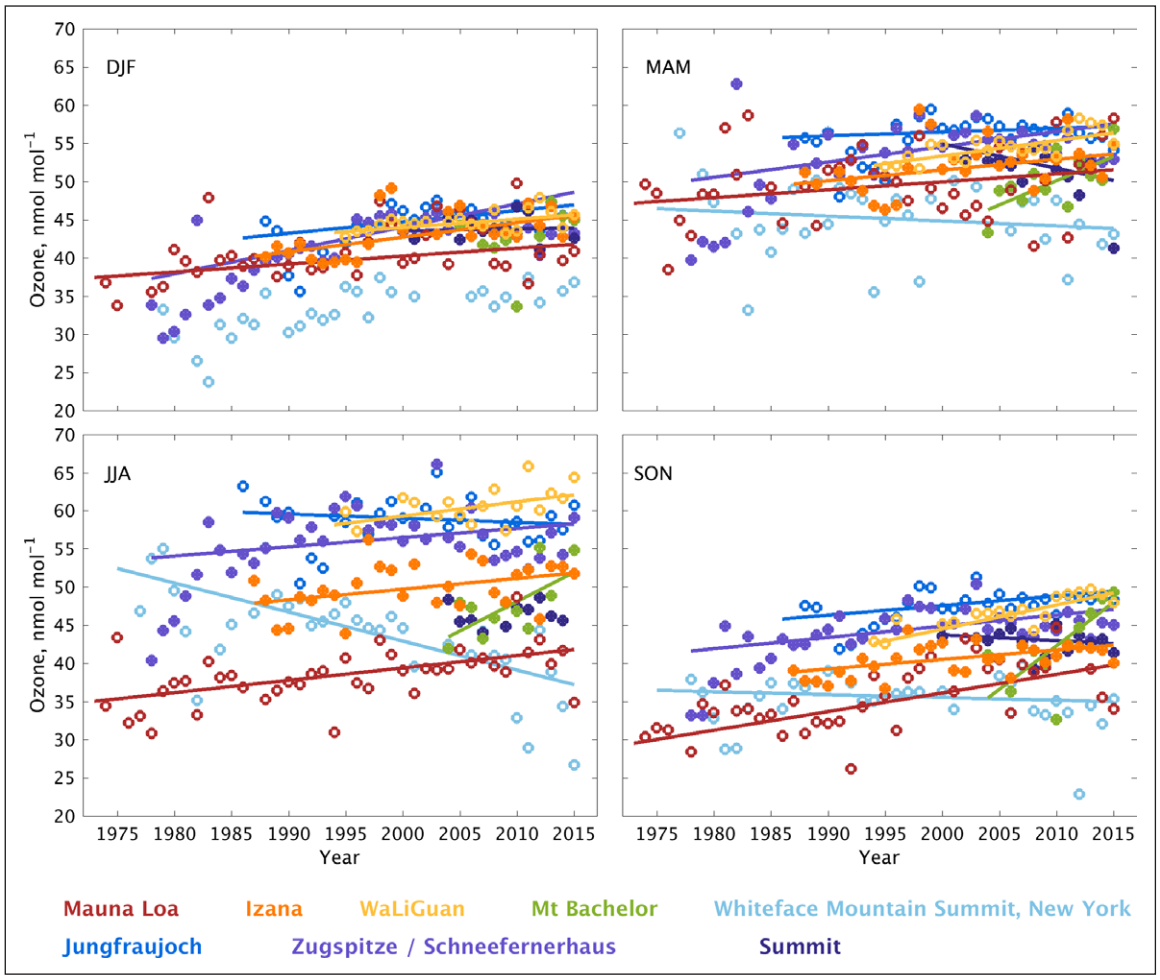

Figure 11: Nighttime ozone trends at eight Northern Hemisphere mountaintop sites by season. Trend values are given in Table 4. DOI: https://doi.org/10.1525/elementa.291.f11

Oltmans et al., 2013; Cuevas et al., 2013; Gratz et al., 2014; Xu et al., 2016), but here we provide an update through 2015. The longest record is Mauna Loa (43 years) and the shortest is Mt. Bachelor Observatory in the northwestern USA (12 years).

We begin with observations recorded continuously since 1973 from Mauna Loa Observatory (MLO). As described in Section 2.2, MLO is impacted by mid-latitude air masses which originate to the north and west and tropical air masses that originate to the south and east. Ozone is typically greater in the mid-latitude air masses and the long term trend at MLO is affected by the relative frequency of air mass transport from high and low latitudes in response to climate variability driven by ENSO and the Pacific Decadal Oscillation. Over shorter time periods the influence of climate variability introduces greater uncertainty on the trend, for example over 1973–2017 the ozone trend at MLO is 0.15 ± 0.05 nmol mol^{-1} yr^{-1} (p = 0.00) while over the most recent 18 years (2000–2017) the trend is 0.20 ± 0.21 nmol mol^{-1} yr^{-1} (p = 0.13) (p indicates the p-value, which is the probability under a specified statistical model that a statistical summary of the data would be equal to or more extreme than its observed value (Wasserstein and Lazar, 2016)) (**Figure 12a**). Reliable ozone observations were also made from MLO during 1957–1959 (Price and Pales, 1963), showing that ozone was much lower in the mid-twentieth century (annual nighttime mean and standard deviation of 30 ± 10 nmol mol^{-1}) compared to the present day (2010–2014 annual nighttime mean and standard deviation of 44 ± 14 nmol mol^{-1}).

Figure 12 shows the long-term (1973–2017) ozone trend at MLO based on monthly nighttime median values using all available data. The figure also shows the ozone trend calculated for the dry and moist air masses at the site, classified according to co-located dewpoint temperature observations. The frequency of the dry and moist air masses changes over time due to the variability of transport patterns. The dry air masses, with greater ozone values, tend to originate to the north and west and/or from higher altitudes (implying long-range transport) and have a trend of 0.23 ± 0.06 nmol mol^{-1} yr^{-1} (p=0.00), double the trend of the moist air masses that tend to originate to the south and east and/or from lower altitudes (0.11 ± 0.05 nmol mol^{-1} yr^{-1}; p = 0.00). Therefore, dry air masses that originate to the north and west make a greater contribution to the overall positive trend than the moist air masses. For the recent period of 2000–2017 ozone increased in dry air masses at the rate of 0.42 ± 0.20 nmol mol^{-1} yr^{-1} (p = 0.00), whereas the moist air masses do not show a statistically significant trend. Therefore, while the

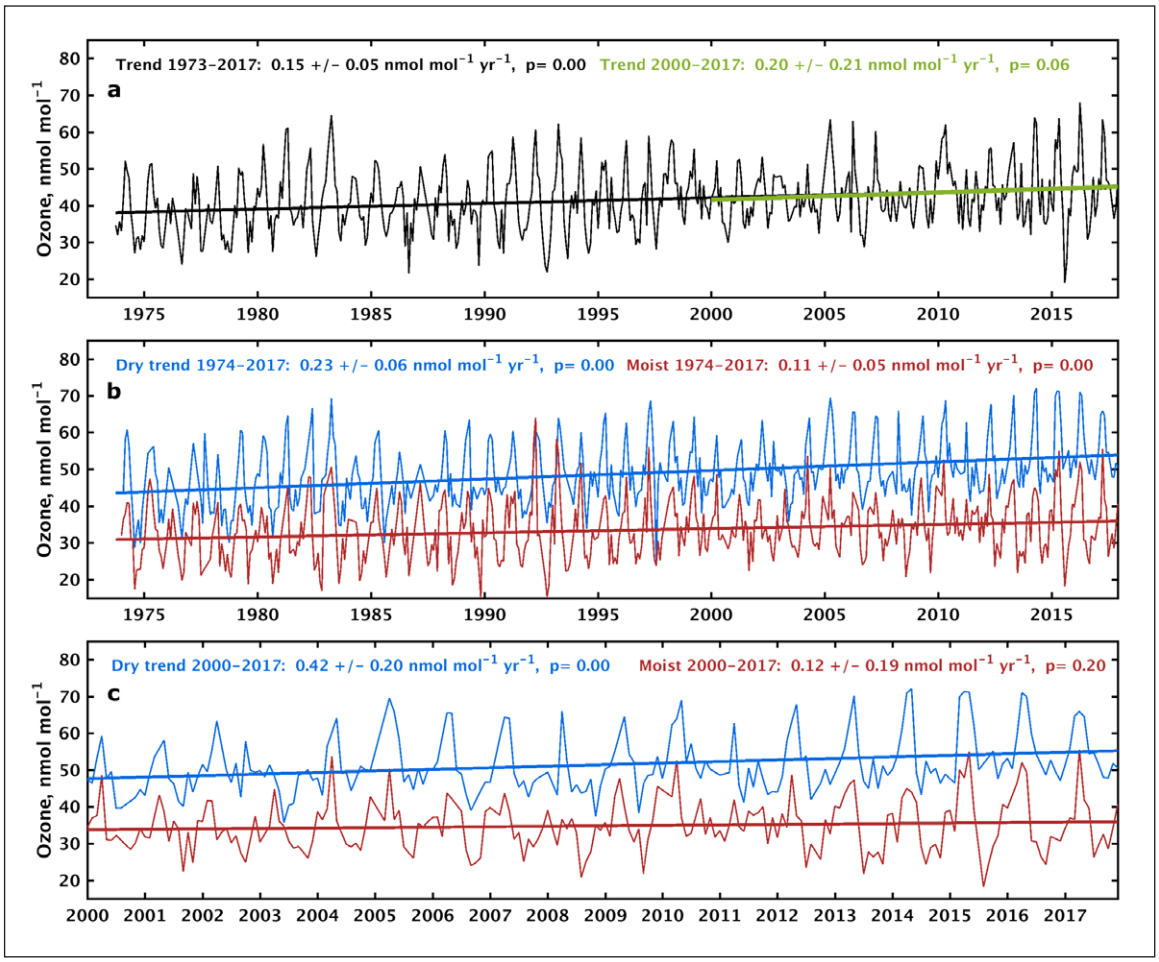

Figure 12: Nighttime monthly median ozone values at Mauna Loa Observatory. a) Nighttime monthly median ozone values at Mauna Loa Observatory calculated with all available data for months with at least 50% data availability, October 1973–December 2017. **b)** Same as in a) but for 1974-2017 data split into dry and moist categories. **c)** As in b) but for 2000–2017. Trends in this figure are based on least-squares linear regression fit through the monthly median values, and reported with 95% confidence intervals and p-values. DOI: https://doi.org/10.1525/elementa.291.f12

overall trend at MLO for the recent period of 2000–2017 does not exhibit a statistically significant trend, the dry air masses impacting the site have experienced a very strong trend with an increase of 7.1 ± 3.4 nmol mol^{-1}, or 14% since 2000. The implication is that the ozone increase in the dry air masses is most likely being driven by the increasing ozone observed across South and East Asia, as described below.

The two sites closest to MLO (seasonal ozone trends in the range of 0.1–0.2 nmol mol^{-1} yr^{-1}) are both at mid-latitudes but on either side of the North Pacific Ocean. Mt. Waliguan (3810 m), upwind of heavily populated eastern China shows seasonal ozone increases in the range of 0.1–0.3 nmol mol^{-1} yr^{-1} since 1994, in agreement with a recent in-depth analysis of this important baseline site (Xu et al., 2016). Mt. Bachelor (2763 m) has much stronger trends in the range of 0.6–1.1 nmol mol^{-1} yr^{-1} (for spring, summer and autumn), but over a much shorter period beginning in 2004 (Fischer et al., 2011; Gratz et al., 2014). In contrast to MLO the trends in moist and dry air masses at Mt Bachelor are similar (Figure S-15).

The only other remote site at low latitudes is Izaña (2367 m) in the eastern subtropical North Atlantic Ocean (Cuevas et al., 2013) with seasonal trends since 1987 in the range of 0.1–0.2 nmol mol^{-1} yr^{-1}. Over the full length of the record only the dry air masses have a significant positive trend, indicating that the observed ozone increase across all air masses is driven by air of mid-latitude origin (Figure S-16). However, since 2000, neither air mass type has a significant trend. Note that this station is influenced by significant air-mass variability on seasonal and inter-annual time scales (Rodríguez et al., 2004). This is particularly true in summertime, when transport variability affects the transport of the Saharan Air Layer (SAL) across the North Atlantic Ocean, allowing for the possibility of ozone interactions with mineral dust (Andrey et al., 2014). During winter-spring ozone can also be influenced by transport variability associated with the North Atlantic Oscillation (Cuevas et al., 2013).

Three sites are located within large industrialized regions. Whiteface Mountain Summit (1483 m) in upstate New York (Schwab et al., 2016) shows a strong decrease of ozone in summer, in agreement with many other rural monitoring sites in the northeastern USA (as shown below). In the Alps, Jungfraujoch (3580 m) (Cui et al.,

2011) shows significant increases in winter and autumn, while Zugspitze (2962 m) (Logan et al., 2012; Oltmans et al., 2013; Parrish et al., 2012) has significant increases in all seasons except summer. Attribution of ozone trends at these high Alpine sites is complicated by changing stratospheric ozone contributions (Trickl et al., 2010; 2014, and references therein). The only high latitude site is Summit, Greenland (3212 m) with no significant trend except for a strong decrease in spring.

Since 2000 significant ozone increases at the remote sites are limited to spring at MLO, spring and autumn at Mt. Waliguan and spring and autumn at Mt. Bachelor (**Table 4** and Figure S-17). Ozone at Izaña has been flat in all four seasons. In the northeastern USA ozone has decreased strongly in summer at Whiteface Mountain Summit. Significant decreases have occurred at Jungfraujoch and Zugspitze in spring for the period 2000–2015, with weaker and insignificant decreases in most other seasons,

Table 4: Nighttime ozone trends at eight mountaintop sites for winter (DJF), spring (MAM), summer (JJA) and autumn (SON)[a]. DOI: https://doi.org/10.1525/elementa.291.t4

Site name *lat. long. alt.(m a.s.l.)*	Years with data		Trend, full record	p-value	Trend, 2000–2015	p-value
Mauna Loa *19.5°N, 155.6°W 3397 m*	1973–2015	DJF	**0.10 (0.03, 0.21)**	**0.01**	–0.05 (–0.63, 0.33)	0.69
		MAM	0.10 (–0.04, 0.23)	0.15	**0.60 (0.09, 1.13)**	**0.04**
		JJA	**0.16 (0.09, 0.23)**	**0.00**	0.18 (–0.06, 0.40)	0.14
		SON	**0.24 (0.14, 0.34)**	**0.00**	–0.26 (–0.67, 0.29)	0.32
Izaña *28.3°N, 16.5°W 2367 m*	1987–2015	DJF	**0.19 (0.09, 0.28)**	**0.01**	0.00 (–0.16, 0.29)	1.00
		MAM	**0.14 (0.02, 0.27)**	**0.03**	0.07 (–0.20, 0.29)	0.62
		JJA	0.14 (–0.02, 0.28)	0.07	0.12 (–0.24, 0.42)	0.69
		SON	**0.13 (0.02, 0.21)**	**0.02**	0.06 (–0.16, 0.26)	0.89
Mt. Waliguan *36.3°N, 100.9°E 3810 m*	1994–2015	DJF	**0.11 (0.01, 0.20)**	**0.04**	0.08 (–0.10, 0.23)	0.69
		MAM	**0.20 (0.10, 0.32)**	**0.00**	0.18 (–0.03, 0.37)	0.06
		JJA	0.19 (–0.06, 0.37)	0.09	0.15 (–0.14, 0.48)	0.32
		SON	**0.32 (0.17, 0.36)**	**0.00**	**0.32 (0.15, 0.36)**	**0.00**
Mt Bachelor[b] *44.0°N, 121.7°W 2763 m*	2004–2015	DJF	too few data	–	too few data	–
		MAM	**0.64 (0.02, 1.24)**	**0.05**	**0.64 (0.02, 1.24)**	**0.05**
		JJA	0.77 (–0.11, 1.58)	0.09	0.77 (–0.11, 1.58)	0.09
		SON	**1.12 (0.83, 1.48)**	**0.00**	**1.12 (0.83, 1.48)**	**0.00**
Whiteface Mt Summit *44.4°N, 73.9°W 1483 m*	1975–2015	DJF	too few data	–	too few data	–
		MAM	–0.07 (–0.24, 0.08)	0.29	too few data	–
		JJA	**–0.38 (–0.49, –0.22)**	**0.00**	**–0.71 (–1.61, –0.07)**	**0.02**
		SON	–0.04 (–0.11, 0.05)	0.38	–0.29 (–0.85, 0.12)	0.13
Jungfraujoch *46.5°N, 8.0°E 3580 m*	1986–2015	DJF	**0.15 (0.04, 0.29)**	**0.01**	–0.07 (–0.21, 0.05)	0.26
		MAM	0.05 (–0.06, 0.19)	0.30	**–0.15 (–0.24, –0.01)**	**0.03**
		JJA	–0.05 (–0.16, 0.11)	0.42	–0.12 (–0.37, 0.17)	0.39
		SON	**0.13 (0.03, 0.23)**	**0.01**	0.03 (–0.09, 0.14)	0.56
Zugspitze *47.4°N, 11.0°E 2962 m*	1978–2015	DJF	**0.31 (0.19, 0.42)**	**0.00**	–0.08 (–0.25, 0.05)	0.12
		MAM	**0.20 (0.04, 0.35)**	**0.01**	**–0.27 (–0.34 –0.13)**	**0.01**
		JJA	0.12 (–0.02, 0.28)	0.08	–0.20 (–0.49, 0.13)	0.30
		SON	**0.15 (0.07, 0.26)**	**0.00**	–0.07 (–0.31, 0.10)	0.44
Summit *72.6°N, 38.5°W 3212 m*	2000–2015	DJF	0.02 (–0.26, 0.45)	0.85	0.02 (–0.26, 0.45)	0.86
		MAM	**–0.32 (–1.04, –0.05)**	**0.02**	**–0.32 (–1.04, –0.05)**	**0.02**
		JJA	too few data	–	too few data	–
		SON	–0.08 (–0.30, 0.14)	0.32	–0.08 (–0.30, 0.14)	0.32

[a] Boldface indicates trend values that are statistically significant at p-value < 0.05. Trend values in parentheses indicate the high and low trend values that bound the 95% confidence interval.

[b] The Mt. Bachelor data were updated in the TOAR Surface Ozone Database on February 22, 2018 to remove the hourly observations for Sept 1–Dec 31, 2006 and Sept 1– Dec 31, 2010 due to newly identified instrument problems during those time periods. The trends in this table were updated accordingly.

in general agreement with Mt Cimone in northern Italy, which has shown a levelling off or slight decrease in ozone since 2000 (Cristofanelli et al., 2015).

Beyond these mountaintop sites our knowledge of lower tropospheric ozone trends from surface observations comes from the many surface ozone monitoring networks and research sites around the world. Because these sites are not located at exceptionally high elevations compared to their immediate surroundings, they cannot provide information on the lower free troposphere at night. Therefore we examine daytime ozone values at non-urban sites (as defined in Section 2.2) to focus on the well-mixed atmospheric boundary layer and to avoid ozone depletion events that occur at night, especially in urban areas with fresh NO emissions. The focus on daytime non-urban sites also increases the likelihood that the observations will be regionally representative, which allows for more straightforward comparison to coarse resolution global atmospheric chemistry models.

Figure 13 shows 2000–2014 daytime ozone trends at all available non-urban sites during DJF and JJA. The vector direction indicates the ozone rate of change and the

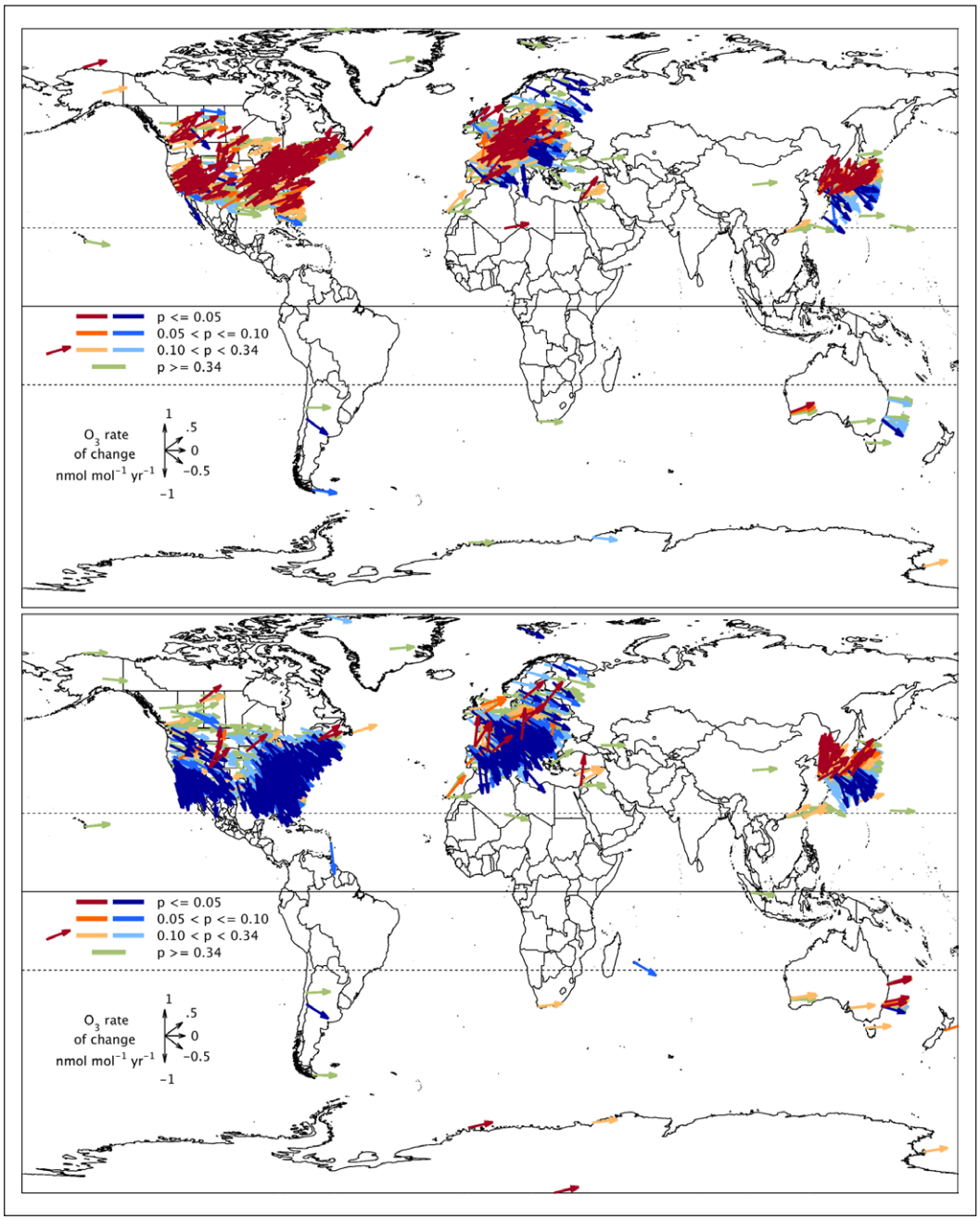

Figure 13: 2000–2014 trends of global daytime average ozone (nmol mol^{-1} yr^{-1}). 2000–2014 trends of daytime average ozone (nmol mol^{-1} yr^{-1}) at 1375 non-urban sites in December–January–February (top) and 1784 non-urban sites in June–July–August (bottom). The number of available sites is greater in June–July–August because many US sites only operate in the warm season. Vector colors indicate the p-values on the linear trend for each site: blues indicate negative trends, oranges indicate positive trends and green indicates weak or no trend; lower p-values have greater color saturation. DOI: https://doi.org/10.1525/elementa.291.f13

shading indicates the significance of the trend using the p-value on the linear trend. Vectors with p-values less than 0.05 are statistically significant, while vectors with p-values in the range of 0.05–0.10 give an indication of a trend. Vectors with p-values in the range of 0.10–0.34 provide a weak indication of change, and p-values greater than 0.34 indicate weak or no change. The vectors with p-values in the range of 0.05–0.34 are very useful for understanding regional trends as they typically follow the same pattern as the statistically significant vectors (Chang et al., 2017). Ozone changes across North America in DJF are largely positive while they are mixed in Europe and East Asia. The few sites available in the SH do not reveal any obvious pattern. During JJA sites in Europe and North America indicate broad regional decreases while trends in East Asia are mixed. In the SH results are mixed, but with positive values exceeding negative values by more than a factor of two. **Figures 14** and **15** provide additional information by focusing on North America, Europe and East Asia for all four seasons.

A separate analysis applied a sophisticated statistical model to the TOAR database to quantify regional ozone trends (Chang et al., 2017). For a given region, such as eastern North America, the generalized additive mixed model (GAMM) can determine the dependence of the mean ozone level on space and time by incorporating explanatory variables from the TOAR database: latitude, longitude, elevation, population density, NO_x emissions and OMI tropospheric column NO_2. As shown in Figure S-18.a, the analysis using all available sites finds overall decreasing trends of summertime (April–September) daytime average ozone across eastern North America and Europe, but increasing ozone over East Asia. The rate of change for rural sites in these three regions is –0.42, –0.17 and + 0.23 nmol mol^{-1} yr^{-1}, respectively. A regional increase of +0.20 nmol mol^{-1} yr^{-1} was also found for southeast Asia, using all available sites. Further details on this methodology are described by Chang et al. (2017).

Because East Asia is a major ozone precursor emission region, we also highlight ozone trends from two recent studies at sites that were not included in the TOAR database or used for the main TOAR analysis. Mt. Tai at 1.5 km above the North China Plain is ideally situated to monitor regional scale ozone levels. Summertime data from 2003–2015 reveal very strong significant positive ozone trends during daytime and nighttime conditions in the range of 1–2 nmol mol^{-1} yr^{-1} (Sun et al., 2016). Shangdianzi is a low elevation, rural Global Atmospheric Watch station northeast of Beijing. Observations from 2003-2014 show a strong and significant increase of maximum daily 8-hour average ozone of approximately 1.1 nmol mol^{-1} yr^{-1} (Ma et al., 2016).

4.2. Free tropospheric ozone trends from in situ and ground-based instruments

4.2.1. In situ observations

Exploratory and sporadic observations of free tropospheric ozone began in the first half of the 20th century using a variety of methods from aircraft and balloon platforms as described in *TOAR-Observations* (Tarasick et al., 2018). Routine observations using ozonesondes became established at a limited number of sites in the 1960s and 1970s, with additional sites established around the world in the 1980s and 1990s (Oltmans et al., 2013; *TOAR-Observations*, Tarasick et al., 2018). Ozonesonde measurement techniques have changed somewhat, becoming much more consistent in the 1980s with the improvements in ozonesonde preparation and the widespread adoption of ECC sondes (*TOAR-Observations*, Tarasick et al., 2018). In addition, routine profiles from commercial aircraft became available from the IAGOS program in 1994, while remotely sensed observations from ground-based lidars also became available in the 1990s.

Cooper et al. (2014) conducted a literature review of free tropospheric ozone trends based on data beginning in the 1970s or 1980s and extending through the early 2000s. Their summary is as follows: "Significant positive trends since 1971 have been observed using ozonesondes above Western Europe, Japan and coastal Antarctica (rates of increase range from 1–3 ppbv $decade^{-1}$), but not at all levels (Oltmans et al., 2013). In addition, aircraft have measured significant upper tropospheric trends in one or more seasons above the northeastern USA, the North Atlantic Ocean, Europe, the Middle East, northern India, southern China and Japan (Schnadt Poberaj et al., 2009). Insignificant free tropospheric trends were found above the Mid-Atlantic USA (1971–2010) (Oltmans et al., 2013) and in the UT above the western USA (1975–2001) (Schnadt Poberaj et al., 2009). While the available data in the free troposphere are limited, a notable finding from the existing literature is that no site or region has shown a significant negative ozone trend since the 1970s."

Focusing on more recent years, ozonesonde analyses have found a pattern of increases in the earlier part of long-term records over most of the NH, but a flattening or even a decline in recent decades (Oltmans et al., 2013, Logan et al., 2012). A recent analysis of Canadian trends, using reevaluated data, finds little change over the 50-year record (Tarasick et al., 2016). In the SH increases until about 2005 were found above midlatitudes, and little change over the entire record elsewhere (Oltmans et al., 2013). An update to the Lauder, New Zealand ozonesonde record (1987–2014) found increasing ozone at Lauder below 6 km, but decreasing ozone in the UT (Zeng et al., 2017).

In this section we focus on free-tropospheric trends since the mid-1990s due to the widespread availability of ozonesonde and commercial aircraft observations in the 1990s, and the improved consistency among ozonesonde profiles. The TOST product is a convenient near-global composite of tropospheric ozone based on profiles from dozens of ozonesonde sites around the world. TOST shows significant ozone increases from 1998–2012 in latitude bands from 30°S to 60°N, but not in the band 30°–60°S. Regional trends of TCO, as quantified by TOST, will be discussed in Section 4.3 where they are compared to five different satellite products.

As described in Section 2.3.3, IAGOS has provided accurate and consistent ozone observations from a fleet of instrumented commercial aircraft since 1994. A new analysis of trends in seven frequently sampled regions of the NH upper troposphere indicates a general increase

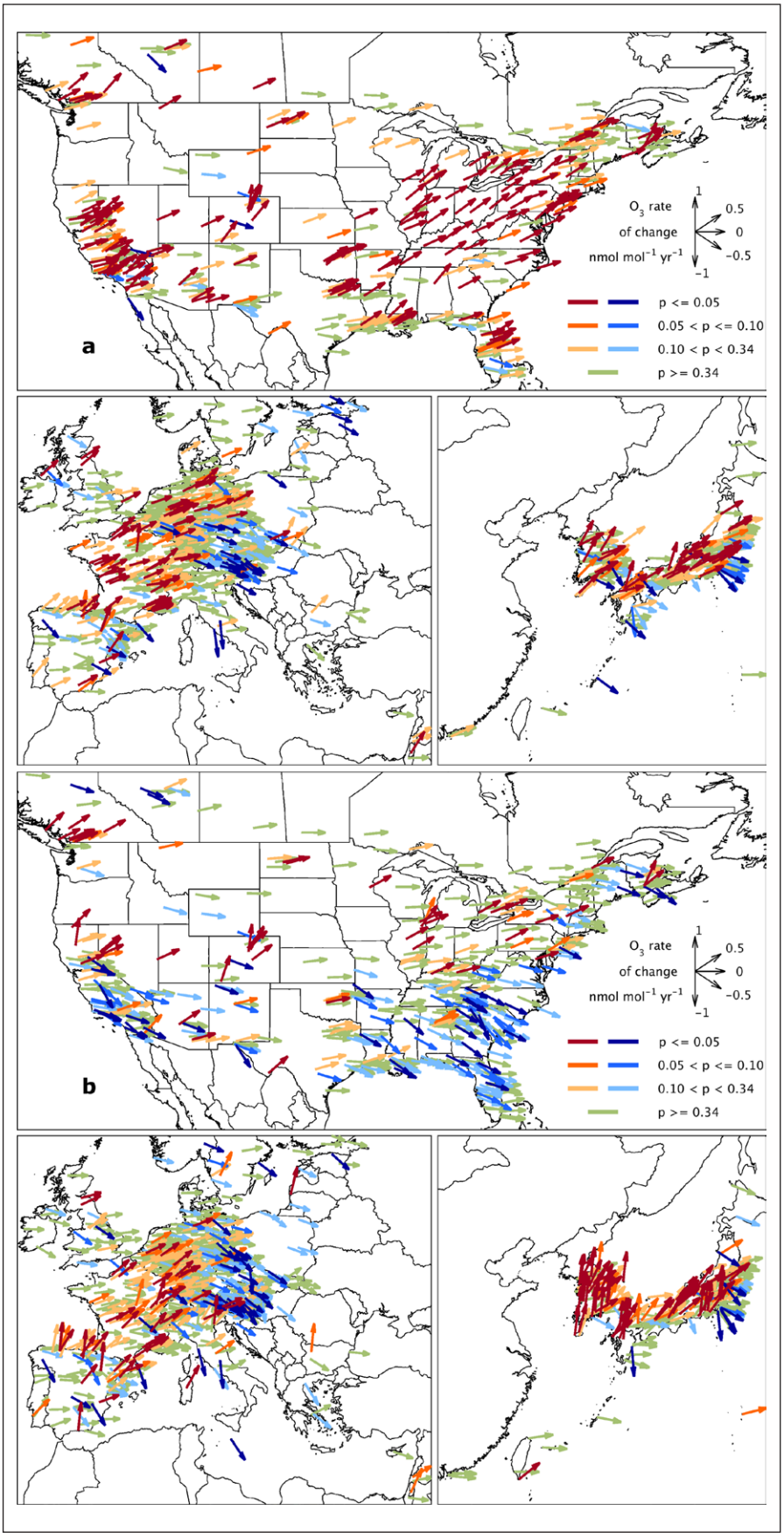

Figure 14: 2000–2014 trends of regional daytime average ozone (nmol mol^{-1} yr^{-1}). Regional trends (2000–2014) of daytime average ozone (nmol mol^{-1} yr^{-1}) at all available non-urban sites for December–January–February (DJF, **a)**, March–April–May (MAM, **b)**. Vector colors indicate the p-value on the linear trend for each site: blues indicate negative trends, oranges indicate positive trends and green indicates weak or no trend; lower p-values have greater color saturation. DOI: https://doi.org/10.1525/elementa.291.f14

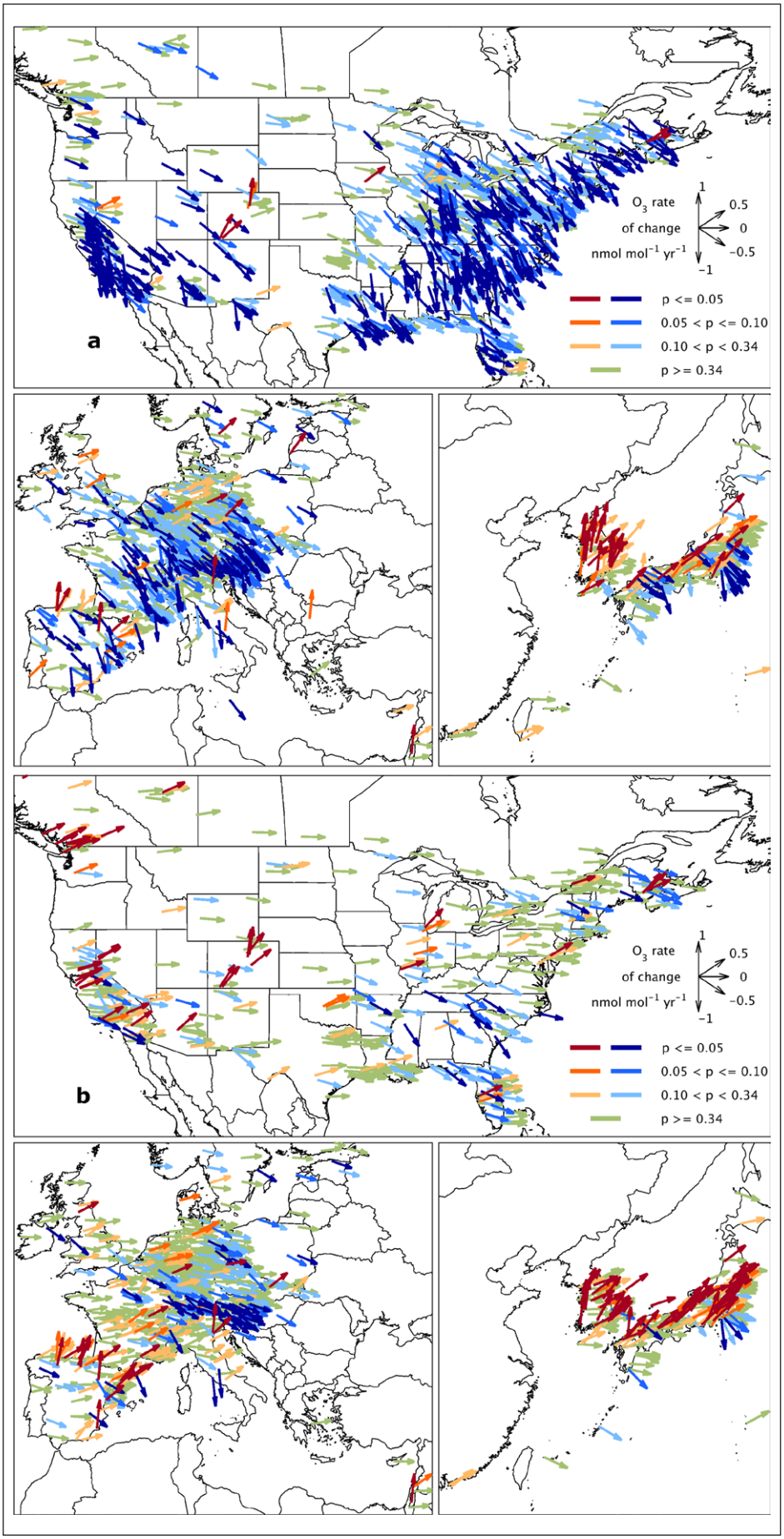

Figure 15: 2000–2014 trends of regional daytime average ozone (nmol mol^{-1} yr^{-1}). As Figure 14 but for June–July–August (JJA, **a)** and September–October–November (SON, **b)**. DOI: https://doi.org/10.1525/elementa.291.f15

of ozone (Cohen et al., 2018). Annual mean upper tropospheric observations from 1995–2013 show a significant increase of ozone across northern mid-latitudes (Eastern US, Europe, western Mediterranean, Middle East, Siberia, northeastern Asia) in the range of 0.24–0. 45 nmol mol^{-1} (Figure S-19). No significant trend was found above the North Atlantic Ocean. There is no seasonal dependence, but the overall trend is most likely driven by the lowest values of the distribution (5th percentile), which is increasing significantly in all seven study regions, in the range of 0.30–0.57 nmol mol^{-1}.

Regions where IAGOS profiles are sufficiently frequent for trend analysis from the surface to 200 hPa include Frankfurt, Germany, the eastern USA, south/central India, Southeast Asia and northeastern China/Korea. As reported previously (Petetin et al., 2016b), annual trends in the troposphere above Frankfurt remain insignificant over the period 1994–2012. However, seasonally, significant positive trends of about + 0.3 nmol mol^{-1} yr^{-1} are found at all levels in winter. Using one more year of data (2013), **Figure 16** shows the seasonal changes in ozone from the early part of the IAGOS record (1994–1999) until the most recently available 5-year period (2009–2013), based on a t-test and a 95% confidence interval. TCO (surface–300 hPa) increased by 11% in winter, 1% in spring and 5% in autumn. Ozone decreased by 2% in summer driven by decreases in the lower troposphere. This approach and that of Petetin et al. (2016b) agree that the strongest ozone increases above Frankfurt occur in winter.

On the other side of the North Atlantic Ocean a composite of IAGOS profiles above several cities in the northeastern USA (**Figure 17**) shows that ozone increased from 1994–2004 to the more recent period of 2005–2013 during winter (7%), spring (7%) and autumn (3%). Summer showed no net change despite a decrease of high ozone events in the lower troposphere.

IAGOS reveals stronger ozone increases above Asia from 1994–2004 to 2005–2014 in those regions where sufficient profiles are available (**Figure 18**), as first reported by Zhang et al. (2016). Above northeast China/Korea ozone has increased most strongly in the boundary layer with peak TCO increases (surface–200 hPa) of 15% in summer. Increases above south/central India are greater with a peak column increase of 31% in autumn. The strongest

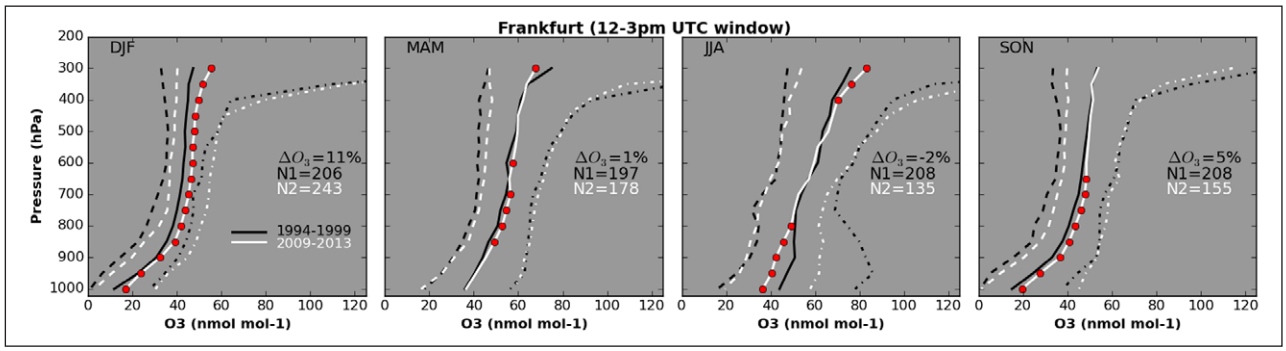

Figure 16: Seasonal change of ozone (nmol mol^{-1}) above Frankfurt (Germany), based on IAGOS commercial aircraft. Seasonal change in the 5th (dashed line), 50th (solid line) and 95th (dotted line) ozone percentiles above Frankfurt (Germany), based on IAGOS aircraft profiles from 1994–1999 (black lines) to 2009–2013 (white lines). Layers in which there is a statistically significant ozone difference between the two time periods are indicated by red dots, based on a t-test and a 95% confidence interval. Each panel indicates the change (ΔO_3, %) in the tropospheric ozone mass (1000–300 hPa) from the earlier to the later period, as well as the number (N1 and N2) of vertical profiles associated with each time period. DOI: https://doi.org/10.1525/elementa.291.f16

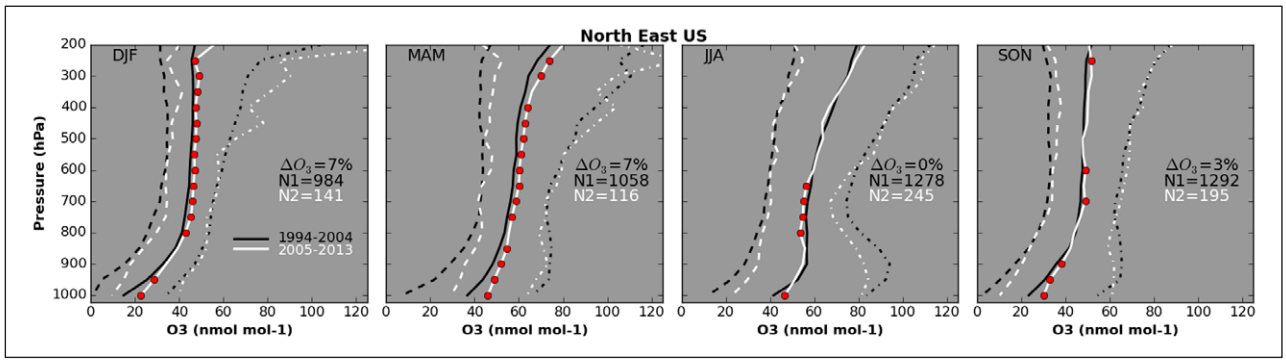

Figure 17: Seasonal change of ozone (nmol mol^{-1}) above northeastern USA, based on IAGOS commercial aircraft. Seasonal change in the 5th (dashed line), 50th (solid line) and 95th (dotted line) ozone percentiles above northeastern USA, based on IAGOS aircraft profiles from 1994–2004 (black lines) to 2005–2013 (white lines). Layers in which there is a statistically significant ozone difference between the two time periods are indicated by red dots, based on a t-test and a 95% confidence interval. Each panel indicates the change (ΔO_3, %) in the tropospheric ozone mass (1000–200 hPa) from the earlier to the later period, as well as the number (N1 and N2) of vertical profiles associated with each time period. DOI: https://doi.org/10.1525/elementa.291.f17

increases are found above Southeast Asia where summertime (JJA) TCO increased by 70%.

4.2.2. Ground-based instruments

Ozone trends in the atmospheric boundary layer and free troposphere can also be detected from ground-based ozone lidars, with long-term records available at Observatoire de Haute Provence (OHP) in southeastern France (Gaudel et al., 2015) and Table Mountain in southern California (Granados-Muñoz et al., 2016). TCO has changed little above OHP from 1994–2004 to 2005–2013 as determined from a combination of lidar and ozonesonde profiles (**Figure 19**). TCO increased by 3% in winter, driven by an increase in the UT, but during the other seasons ozone

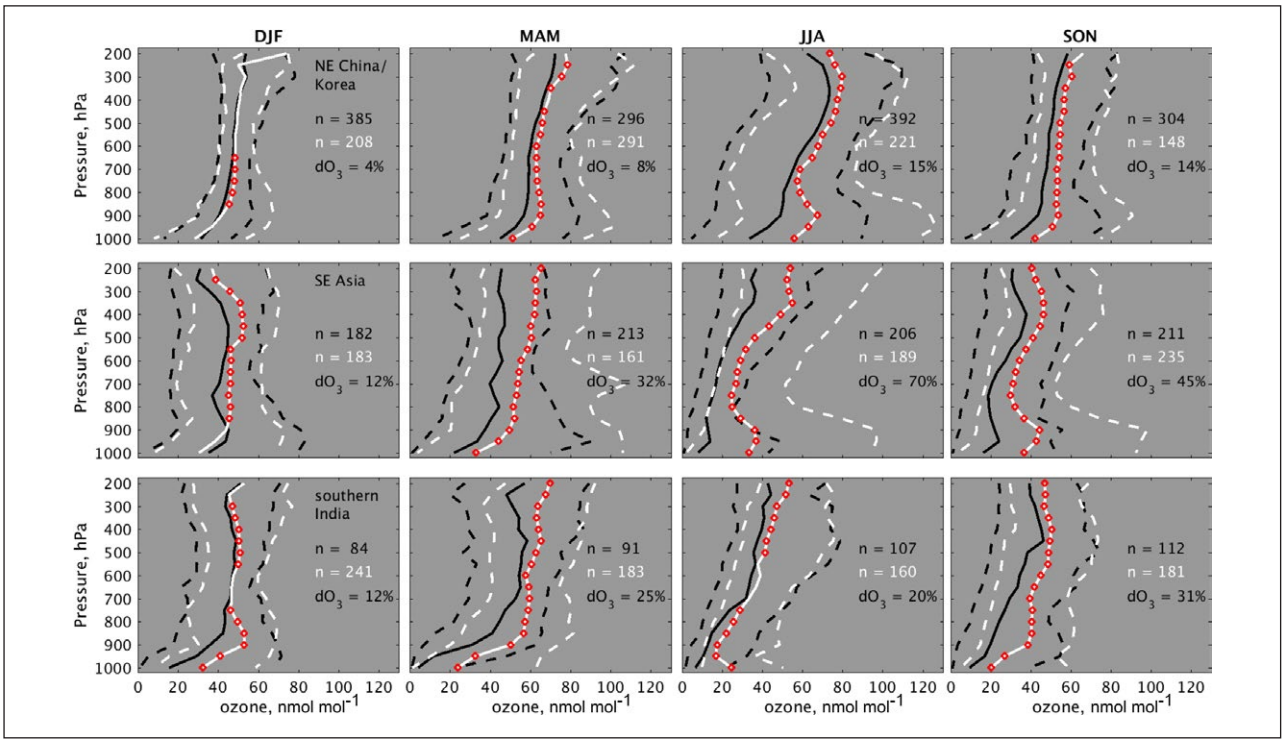

Figure 18: Seasonal change of ozone (nmol mol^{-1}) above northeastern China, Southeast Asia and south/central India, based on IAGOS and ozonesonde profiles. Seasonal change in the 5th (dashed line), 50th (solid line) and 95th (dashed line) ozone percentiles above northeastern China (NE China/Korea, 30°–43°N, 110°–129°E), Southeast Asia (SE Asia, 10°–24°N, 93°–115°E), and south/central India (southern India, 6°–24°N, 70°–89°E) based on IAGOS aircraft profiles from 1994–2004 (black) to 2005–2014 (white). In addition, Southeast Asia includes ozonesonde profiles from the SHADOZ station in Hanoi, Vietnam. Layers in which there is a statistically significant ozone difference between the two time periods are indicated by red circles, based on a t-test and a 95% confidence interval. Each panel indicates the change (ΔO_3, %) in the tropospheric ozone mass (1000–200 hPa) from the earlier to the later period, as well as the number (n) of vertical profiles associated with each region and time period. These results were first reported by Zhang et al. (2016). DOI: https://doi.org/10.1525/elementa.291.f18

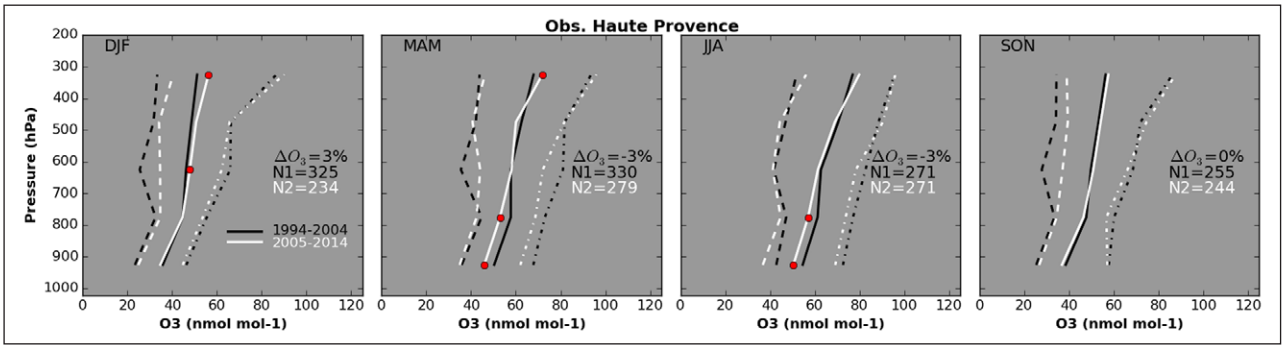

Figure 19: Seasonal change of ozone (nmol mol^{-1}) above Observatoire de Haute Provence (France), based on a combination of lidar and ozonesondes profiles. Seasonal change in the 5th (dashed line), 50th (solid line) and 95th (dotted line) ozone percentiles above Observatoire de Haute Provence, France, as measured by a combination of lidar and ozonesonde profiles from 1994–2004 (black lines) to 2005–2014 (white lines). Layers in which there is a statistically significant ozone difference between the two time periods are indicated by red dots, based on a t-test and a 95% confidence interval. Each panel indicates the change (ΔO_3, %) in the tropospheric ozone mass (surface-200 hPa) from the earlier to the later period, as well as the number (N1 and N2) of vertical profiles associated with each time period. An update to Gaudel et al. (2015). DOI: https://doi.org/10.1525/elementa.291.f19

decreased by 2–3%, largely driven by ozone decreases in the lower troposphere. Changes in ozone above Table Mountain are more variable with a 9% decrease in winter and a 7% increase in summer (**Figure 20**). Ozone also decreased by 5% in autumn, driven by the lower troposphere. Spring shows no net change due to decreases in the lower troposphere being offset by increases in the UT. This lack of change is in contrast to a springtime increase of ozone observed by a composite of observations across western North America for the period 1995–2014 (Lin et al. 2015). Differences could be due to different sampling strategies, with Table Mountain representing one location during March–April–May (2000–2015) while the 20-year composite covers most of western North America during April–May (1995–2014). Ozone time series in this region are strongly affected by shifts in transport patterns associated with climate variability, which affects the ozone trend, especially over shorter time periods (Lin et al., 2015).

FTIR and Umkehr instruments provide long-term TCO observations above 14 stations worldwide (**Figure 21**), with FTIR extending from the surface to 8 or 12 km, and Umkehr extending from the surface to 250 hPa. Because the two methods report different columns, a direct comparison between collocated instruments is challenging. Comparison of Umkehr to ozonesondes at OHP, France shows different trends between the instruments for the period 1991–2014, due to an overestimation of Umkehr data in the early 1990s (Figure S-20). Comparison of FTIR to ozonesondes, and Umkehr to ozonesondes at Lauder, New Zealand shows that both instruments are similar to the sondes for the period 2001–2016 (Figure S-21).

The three FTIR instruments in the Arctic indicate weak and insignificant decreases since 1996 while the sole Arctic Umkehr instrument finds a significant increase. At northern mid-latitudes, three Umkehr and one FTIR instrument detect no significant trends. In the northern subtropics, the FTIR instrument at Izaña (Schneider et al., 2005) indicates an increase although the trend is not statistically significant, while in the tropics, the Umkehr instrument at MLO records a significant increase from 1995 until 2016. At southern mid-latitudes the Umkehr and FTIR instruments at Lauder, New Zealand show increasing ozone although the trends are not statistically significant. The FTIR instrument at Wollongong, Australia indicates a weak ozone decrease while the Umkehr at Perth, Australia shows an increase. Finally, the FTIR at Arrival Heights, Antarctica shows no change. In summary, these broadly scattered instruments indicate no consistent picture of ozone changes around the world. Notably, none of these stations are in Asia where IAGOS aircraft profiles indicate strong ozone increases since the mid-1990s. The station closest to Asia is MLO which shows an increase of TCO, in agreement with the lower free-tropospheric ozone increases observed at MLO. Further ground-based instrument intercomparisons are possible at specific locations such as MLO and Boulder, Colorado, USA. Sites with co-located ground-based instruments could also be used for comparison to satellite data but these studies are beyond the scope of this paper.

4.3. The global view from satellites

The Tropospheric Ozone Residual (TOR) was the first satellite product to quantify tropospheric ozone, providing TCO values (1° × 1.25° resolution) across much of the globe (50°S–50°N) from 1979 through 2005 (Fishman et al., 2003). The product was derived by subtracting stratospheric column ozone measured by polar orbiting Solar Backscattered Ultraviolet (SBUV) instruments from coincident total ozone measured by Total Ozone Mapping Spectrometer (TOMS) instruments. The product was never fully evaluated to determine its accuracy for calculating trends (J. Fishman, personal communication) and, therefore, we will not attempt to draw conclusions on ozone trends over the TOR instrument record. However, we can use the product to gain insight regarding the relative tropospheric ozone maxima at the beginning of the satellite record. **Figure 22** shows TOR across the globe during JJA averaged over 1979–1983. In those days, there were four

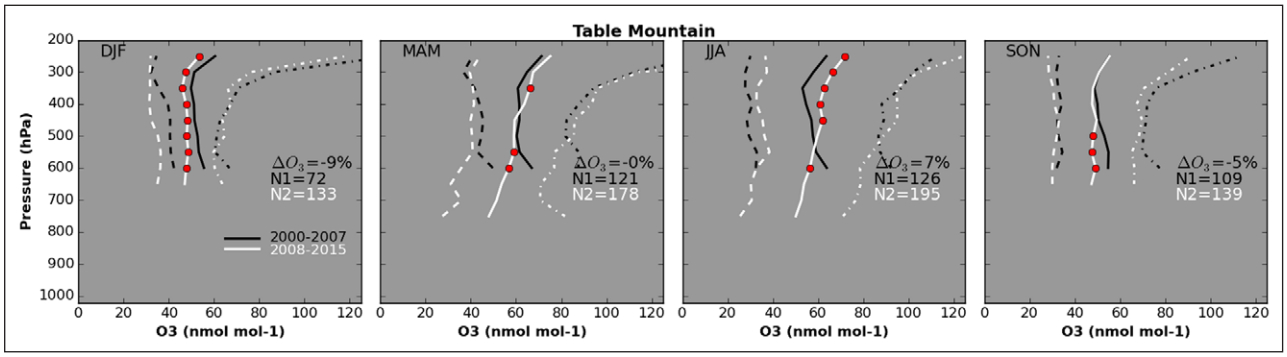

Figure 20: Seasonal change of ozone (nmol mol^{-1}) above Table Mountain Facility (Southern California, USA), based on lidar profiles. Seasonal change in the 5th (dashed line), 50th (solid line) and 95th (dotted line) ozone percentiles above Table Mountain Facility, Southern California, USA as measured by a combination of lidar and ozonesonde profiles from 2000–2007 (black lines) to 2008–2015 (white lines). Layers in which there is a statistically significant ozone difference between the two time periods are indicated by red dots, based on a t-test and a 95% confidence interval. Each panel indicates the change (ΔO_3, %) in the tropospheric ozone mass (surface-200 hPa) from the earlier to the later period, as well as the number (N1 and N2) of vertical profiles associated with each time period. An update to Granados-Muñoz et al. (2016). DOI: https://doi.org/10.1525/elementa.291.f20

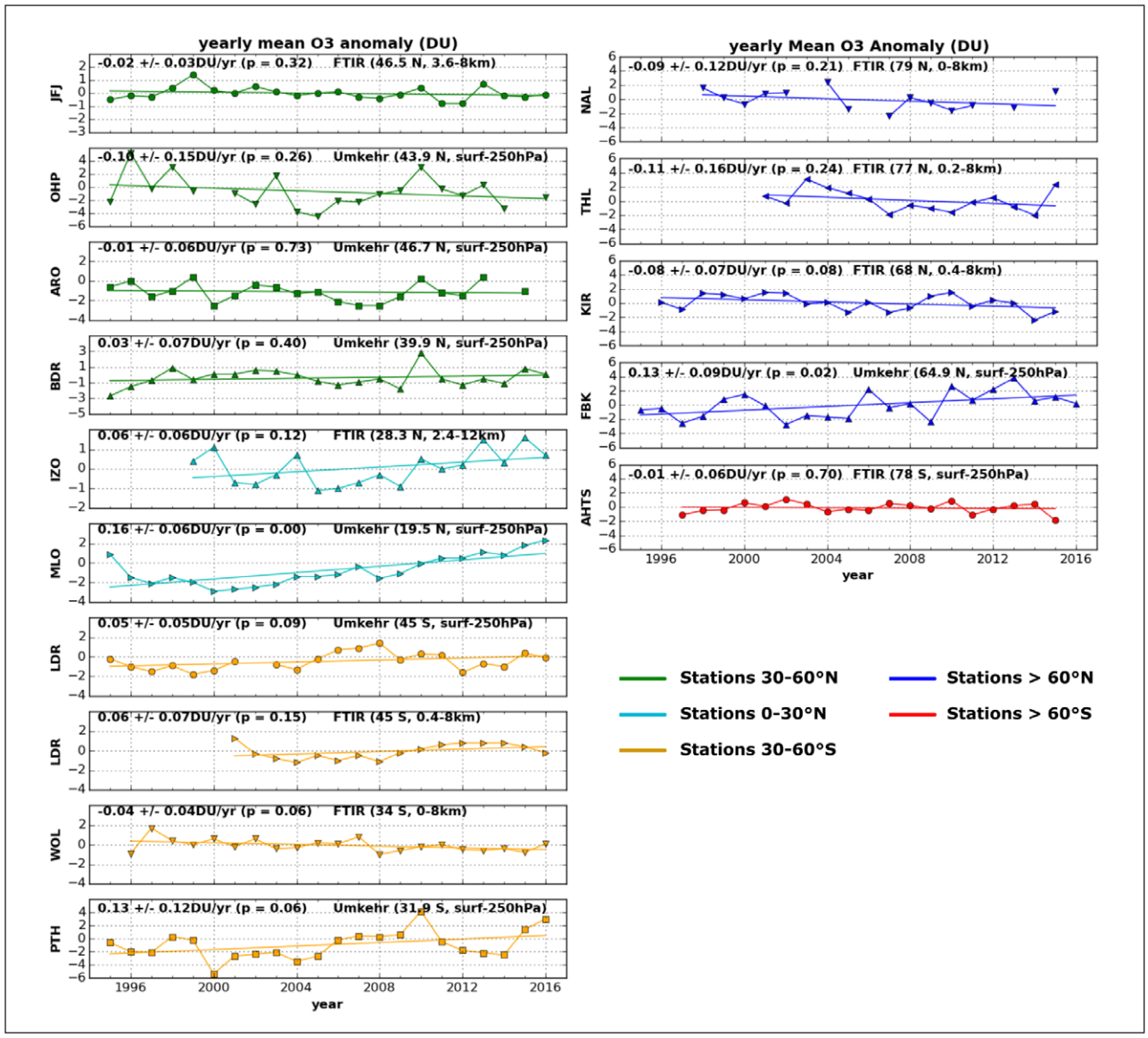

Figure 21: Trends of TCO anomalies (DU) measured by FTIR and Umkehr. Trends of tropospheric column ozone (TCO) anomalies in Dobson unit (DU) measured by FTIR and Umkehr above thirteen stations: Jungfraujoch (JFJ), Observatoire de Haute Provence (OHP), Boulder (BDR), Izaña (IZO), Mauna Loa (MLO), Lauder (LDR), Wollongong (WOL), Perth (PTH), Ny-Ålesund (NAL), Thule (THL), Kiruna (KIR), Fairbanks (FBK) and Arrival Heights (AHTS). Colors indicate the latitude bands in which stations are located. Time series of TCO anomalies for latitude bands above 60°N or 60°S are shown in the right panel. Here, TCO anomaly is defined as daily TCO minus monthly TCO over the time-series of the measurement. As a result, the seasonal cycle should not affect the trend. Linear trends are reported with 95% confidence intervals and p-values. DOI: https://doi.org/10.1525/elementa.291.f21

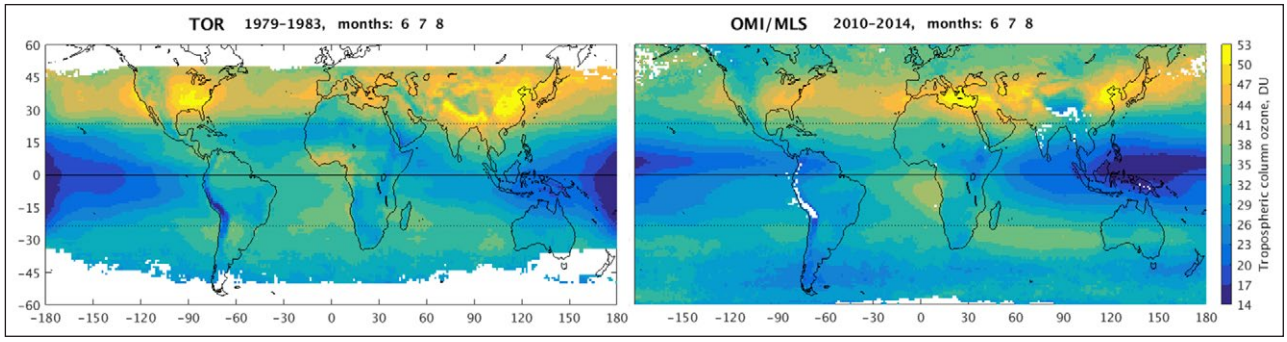

Figure 22: June–July–August mean TCO (DU) measured by TOR and OMI/MLS. June–July–August tropospheric column ozone (TCO) in Dobson unit (DU) as measured by the TOR product for 1979–1983 (left) and OMI/MLS for 2010–2014 (right). DOI: https://doi.org/10.1525/elementa.291.f22

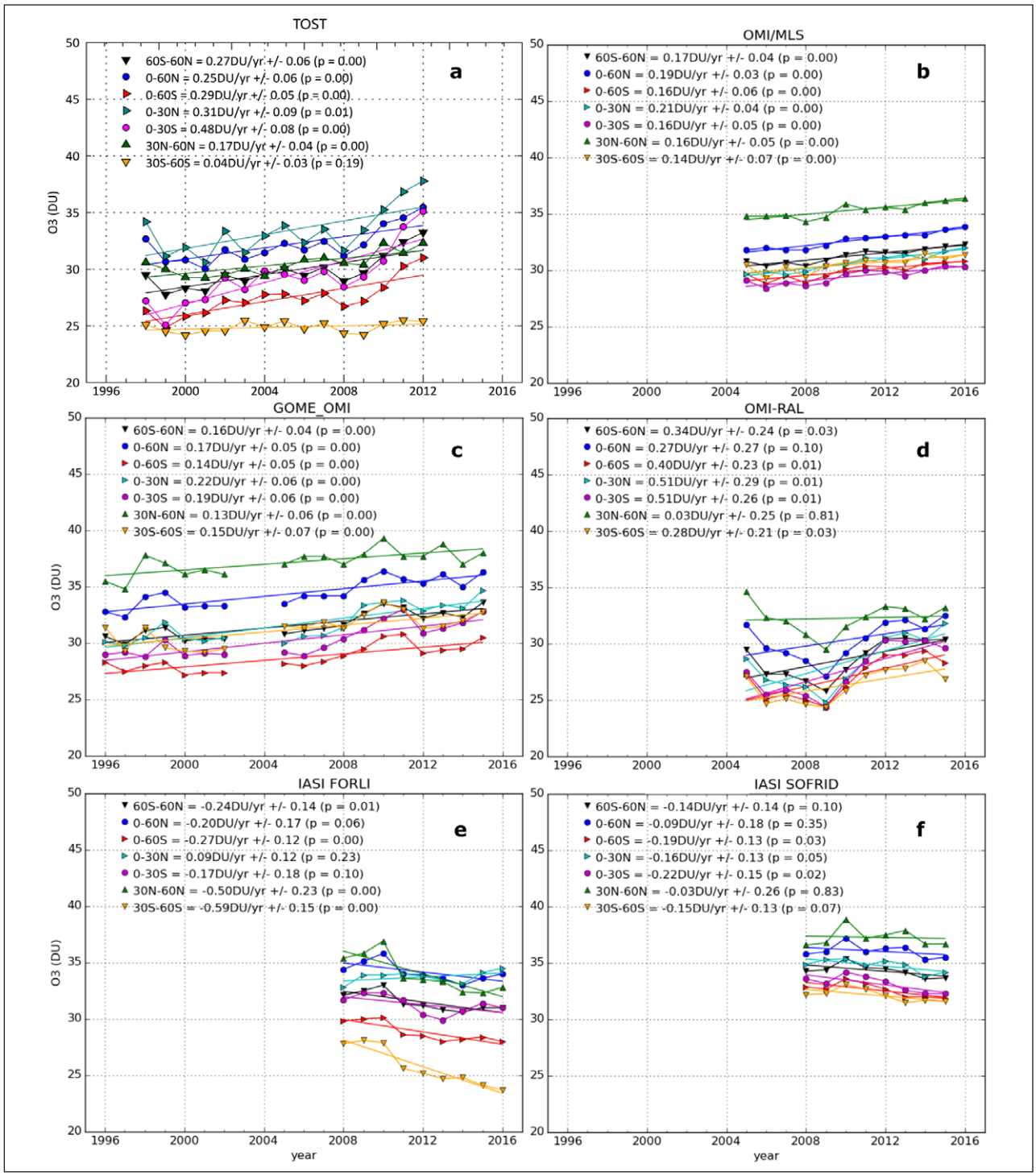

Figure 23: Trends of TCO (DU yr^{-1}) by latitude band from five satellite products and ozonesondes (TOST). Trends of tropospheric column ozone (TCO) in Dobson unit per year (DU yr^{-1}) by latitude band (60°N–60°S, 0–60°N, 0–60°S, 0–30°N, 0–30°S, 30–60°N, 30–60°S) as measured by **(a)** TOST, **(b)** OMI/MLS, **(c)** GOME/OMI-SAO, **(d)** OMI-RAL, **(e)** IASI-FORLI, and **(f)** IASI-SOFRID. Linear trends are reported with 95% confidence intervals and p-values. DOI: https://doi.org/10.1525/elementa.291.f23

relative ozone maxima in the NH: the North American west coast, eastern USA, northern India and eastern China. In contrast, the OMI/MLS TCO product shows only two present-day maxima: northeastern China and the Mediterranean. The two products are derived similarly, but because they are not intercalibrated we cannot say if the present-day ozone maxima stand out because of increasing ozone in those regions, or if the intensity of ozone production in the other regions declined.

To understand how the tropospheric ozone burden has changed since the mid-1990s we now compare TCO by latitude band from five different satellite products, plus the TOST composite ozonesonde product (**Figure 23**). Reported trends are based on linear regression. As described above, TOST shows significant ozone increases from 1998–2012 in latitude bands from 30°S to 60°N, with strongest increases in the tropics and no increase in southern mid-latitudes (30°–60°S). The OMI/MLS

product shows significant increases from 2005–2016 at all latitude bands between 60°S–60°N with strongest increases in the northern tropics and weakest trends in southern mid-latitudes (30°–60°S). The GOME/OMI-SAO product extends from 1996 to 2015 and shows significant increases in all latitude bands with the strongest trend in the northern tropics. The OMI-RAL product shows an increase from 2005 to 2015 between 60°S–60°N, with the strongest increases in the tropics. In contrast, the IASI-FORLI product shows a small decrease of ozone during 2008–2016 from 60°S–60°N, with the strongest decrease at southern mid-latitudes. The IASI-SOFRID product also indicates a decrease of ozone over the period 2008–2016 from 60°S–60°N, with the strongest decrease also occurring in the SH, but in the tropics rather than mid-latitudes.

To understand how products vary in their detection of regional trends, **Figure 24** compares annual trends at 5° × 5° resolution across the globe between TOST and the five satellite products (Figures S-22–S-27 provide seasonal comparisons). TOST, covering 2003–2012 shows strongest ozone increases above Brazil, northeastern Africa, the tropical Indian Ocean, East Asia and the western Pacific Ocean. Notable regions of ozone decreases are found over southern Africa and the Antarctic Peninsula. The satellite products span slightly different periods than TOST which may partially explain why they differ from TOST, yet the differences between satellite products can be as great as their differences from TOST. It is difficult to compare trends between satellite products with different measurement techniques and retrieval methods, as described in Section 2.5. **Figure 25** provides a simple assessment of the regions of the world where TOST and the five satellite products agree in their depiction of statistically significant annual ozone trends. We note that while each product is derived differently, the three products using OMI radiances are not fully independent of one another, nor are the two IASI products. The greatest agreement in terms of positive trends is found in the tropics with the region stretching from South America eastwards to the western Pacific Ocean containing many grid cells with at least 4 products with positive trends. Regions with at least five products in agreement are Southeast Asia, equatorial Brazil, central northern Africa, the tropical South Indian Ocean and northern Australia. Southeast Asia is the most extensive region with at least five products in agreement, including five grid cells showing agreement between all 6 products.

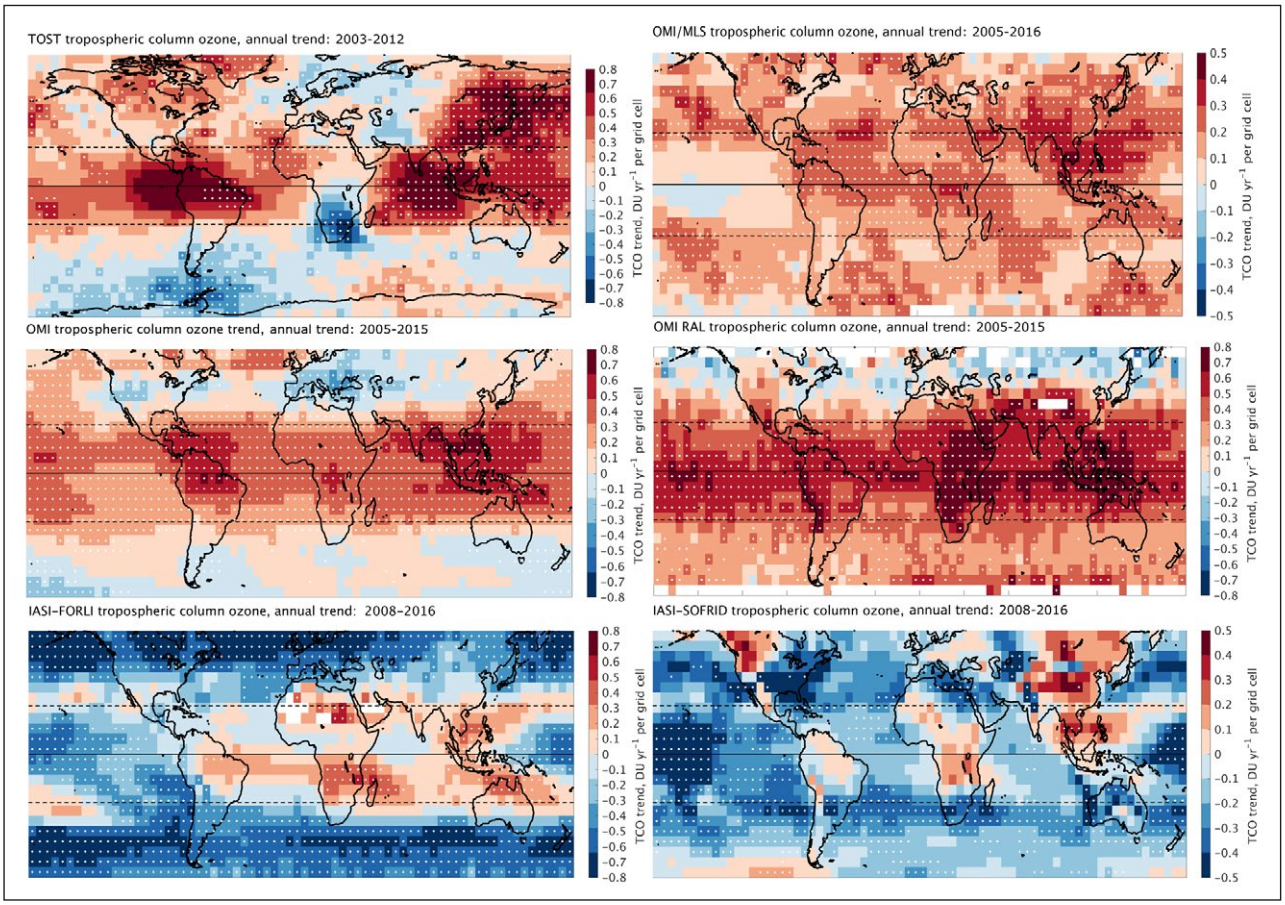

Figure 24: Maps of trends of TCO (DU yr^{-1}) from five satellite products and ozonesondes (TOST). (top left) 2003–2012 TOST ozonesonde annual tropospheric column ozone (TCO) trends in Dobson unit per year (DU yr^{-1}) for each 5° × 5° grid cell between 80°S–80°N. White dots indicate grid cells with statistically significant trends. Also shown are satellite products between 60°S–60°N: (top right) OMI/MLS, 2005–2016, (middle left) OMI-SAO, 2005–2016, (middle right) OMI-RAL, 2005–2015, (bottom left) IASI-FORLI, 2008–2016, and (bottom right) IASI-SOFRID, 2008–2015. Note that OMI/MLS and IASI-SOFRID have different color scales from the rest. Trends in this figure are based on least-squares linear regression and reported with 95% confidence intervals and p-values. DOI: https://doi.org/10.1525/elementa.291.f24

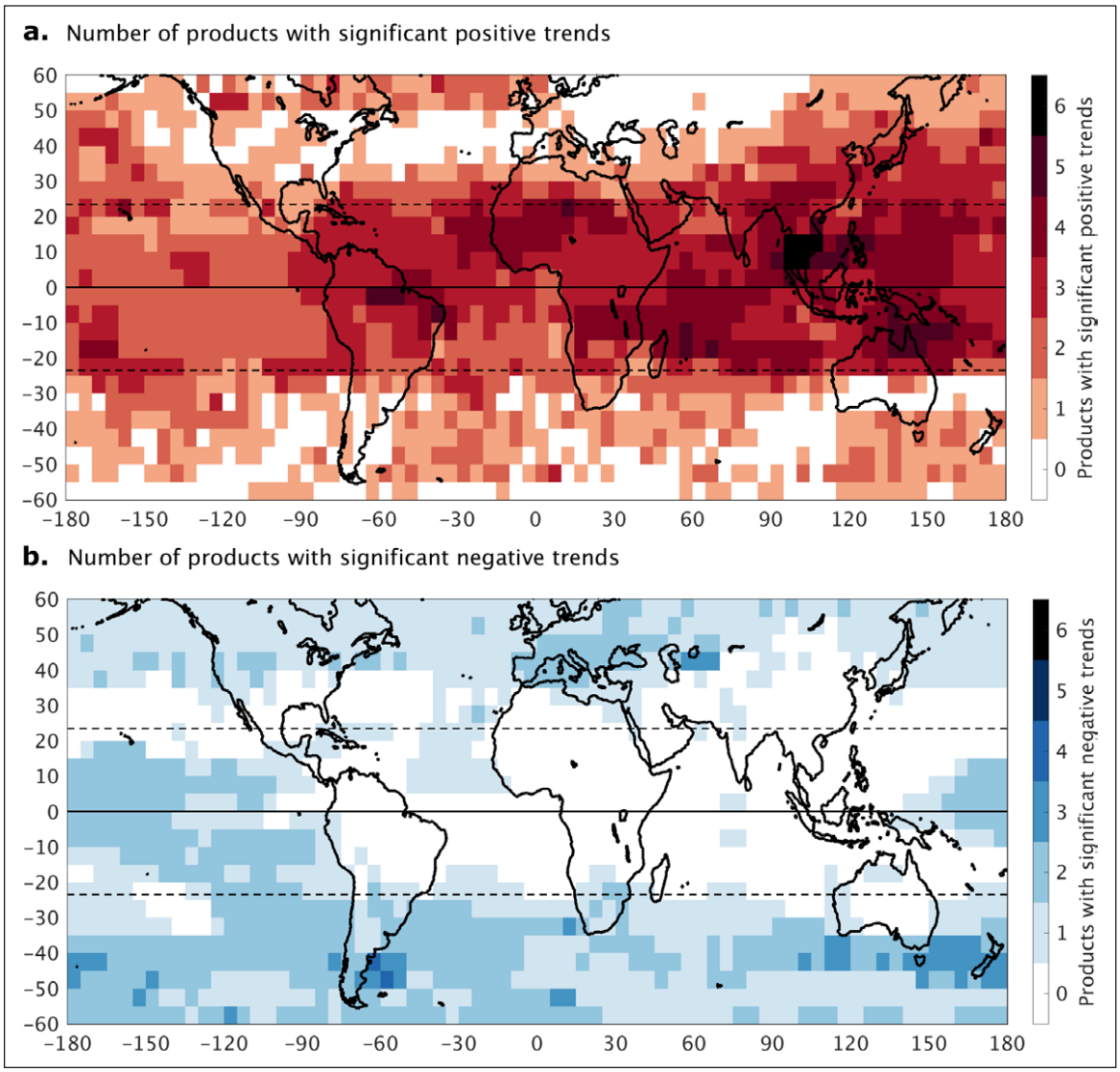

Figure 25: Number of products from Figure 24 with statistically significant positive and negative trends per grid cell. (a) Number of products from Figure 24 that indicate a statistically significant positive trend in each 5° × 5° grid cell. All six products shows significant ozone increases in five grid cells, all above Southeast Asia. **(b)** As in (a) but for statistically significant negative trends. DOI: https://doi.org/10.1525/elementa.291.f25

Figure 25 also shows the agreement between products in terms of statistically significant negative trends, which is weaker than the agreement for positive trends. In the tropical region from South America eastward to Indonesia most grid cells show no decrease and at most only one product per grid cell shows a decrease. No product shows a decrease above Southeast Asia or eastern China south of 40°N. There are only two regions where three or four products agree on significant decreases, located in the SH mid-latitudes above New Zealand and South America.

There are two other satellite products reported in the literature that provide information on TCO from the past decade, but are not part of the comparison described above. The first is derived from the now expired SCIAMACHY instrument which provided trend estimates for 70°S–70°N from 2003 to 2011 (Ebojie et al., 2016). Overall, the product found statistically insignificant increases between 50°S and 30°N and insignificant decreases between 30°N–70°N. On a regional basis, the strongest significant increase was a broad region above SE Asia, similar to the region of significant trends in **Figure 25**. The second product is a 20-year (1995–2015) composite of TCO above the tropics from the GOME, SCIAMACHY, OMI, GOME-2A and GOME-2B instruments (Heue et al., 2016). The 20-year tropical trend is 0.07 ± 0.01 DU yr^{-1}, less than half the rate of four products in **Figure 25** that show increasing tropical ozone (TOST, OMI/MLS, GOME/OMI-SAO and OMI-RAL). Regionally the strongest trends were found in a band from central northern Africa eastwards to SE Asia, and in a band stretching from northern Brazil eastwards to central Africa. In the near future, additional long-term (20-years or more) composites of tropical TCO using multiple satellite instruments will be available for tropical ozone trend quantification (Leventidou et al., 2016; J. Ziemke, personal communication).

5. Discussion and Conclusions

Sections 3 and 4 have provided an up-to-date overview of tropospheric ozone's present-day distribution and trends. Many factors, both anthropogenic and natural, influence

these ozone values (Monks et al., 2015; Neu et al., 2014), and a consideration of all of these processes is beyond the scope of this paper. However, *TOAR-Ozone Budget* (Archibald et al., 2018) provides a new review of these processes and *TOAR-Model Performance* (Young et al., 2018) discusses the present-day capabilities of global atmospheric chemistry models to simulate tropospheric ozone. To synthesize the findings from Sections 3 and 4 we focus our discussion on five regions that have experienced notable ozone changes since the 1990s at the surface and in the free troposphere: mid-latitude North America (Section 5.1), Western Europe (Section 5.2), East Asia (Section 5.3), the NH tropics (0°–30°N) (Section 5.4) and the SH tropics (0°–30°S) (Section 5.5). We also highlight the region across the Mediterranean and Middle East, not because we have firm evidence that ozone in this region is changing, but because it contains a strong summertime TCO maximum that has not been fully explored or monitored with in situ observations, especially across the Middle East (Section 5.6). The section concludes with an assessment of the tropospheric ozone burden (Section 5.7), and ozone's long-wave radiative effect (Section 5.8), followed by information for accessing the ozone datasets discussed by *TOAR-Climate* (Section 5.9).

In the discussion that follows, the peer-reviewed literature is relied upon to briefly place the observed trends in the context of current understanding of the processes that control ozone in each region. As ozone trends are strongly impacted by changes in precursor emissions, we summarize the latest findings on global emissions of the key ozone precursor, nitrogen oxides (NO_x). The Community Emissions Database System (CEDS) global bottom-up emission inventory (Hoesly et al., 2018) shows an increase in global anthropogenic NO_x emissions of roughly 17% from 2000 to 2010 with nearly constant emissions from 2010–2014. Over this period, emissions decreased in North America and western Europe and increased in Asia. The net result is a small decrease of about 5% in the 30°–90°N latitude band, and large increases of 60% in the NH tropics (0°–30°N) and a doubling of emissions in the SH tropics, with SH tropical emissions being only a quarter of NH tropical emissions. A recent top-down emission inventory using OMI-detected tropospheric column NO_2 indicates no net change in global NO_2 emissions from 2005 to 2014, but with decreases of NO_x emissions in North America and Western Europe and increases in India and China, although Chinese emissions have decreased since 2011 (Miyazaki et al., 2017).

5.1. Mid-latitude North America

Much has been written in recent years regarding the decrease of extreme surface ozone episodes across mid-latitude North America in response to decreasing domestic ozone precursor emissions (Lefohn et al., 2010; Cooper et al., 2012; Simon et al., 2015) as well as the impact of increasing Asian emissions offsetting some of the domestic ozone reductions (Jacob et al., 1999; Brown-Steiner and Hess, 2011; Huang et al., 2013; Strode et al., 2015; Verstraeten et al., 2015; Lin et al., 2017). Surface ozone reductions are clearly seen for daytime average ozone for June–July–August over the period 2000–2014 (**Figure 15**), however there is no clear mid-latitude decrease in spring or autumn, and winter shows a general increase. Free tropospheric ozone trends above North America are difficult to quantify due to a sparse sampling network with infrequent observations. The longest continuous records are from ozonesondes above Canada (Tarasick et al., 2016) and Wallops Island, Virginia (Oltmans et al., 2013) which show no overall change since the 1970s/1980s. Focusing on April–May, an analysis of all available ozone observations from multiple platforms above western North America found a significant increase of free tropospheric ozone (~0.3 nmol mol^{-1} yr^{-1}) for 1995–2014 (Lin et al., 2015). In *TOAR-Climate* analysis of high-frequency 2000-2015 lidar observations above Table Mountain in southern California (**Figure 20**) shows increases in summer, no change in spring and decreases in winter and autumn. Commercial aircraft observations above the northeast USA show ozone has increased since the 1990s during winter, spring and autumn with no change during summer (**Figure 17**). Focusing on the UT, commercial aircraft have also observed significant positive annual trends above the eastern US (Cohen et al., 2018). In terms of TCO, the ozonesonde and satellite products summarized in **Figure 25** indicate no clear trend. In summary, while clear ozone changes can be demonstrated for particular regions and seasons it is not possible to define an overall trend for mid-latitude North America.

5.2. Europe

As with mid-latitude North America, extensive air quality monitoring and analysis have shown that reductions in ozone precursor emissions have reduced extreme ozone levels across much of Europe at both rural and urban sites (Derwent et al., 2010; Simpson et al., 2014; EEA, 2016). A recent update to the baseline ozone record on the west coast of Ireland shows ozone increased during the 1980s and 1990s and has remained constant or even begun to decline since 2000 (Derwent et al., 2018). Focusing on just the annual mean of the maximum daily average 8-h ozone values, rural background sites across Europe were generally characterized by decreasing ozone while heavily urbanized sites showed ozone increases over 2000–2014 (EEA, 2016). Analysis of the surface sites from the TOAR database found similar results, but seasonal trends of daytime average ozone revealed that non-urban sites only showed broad decreases across Europe during summer months while increasing and decreasing trends varied widely across the region during other seasons (**Figures 14** and **15**). In the free troposphere ozonesonde and lidar observations from southern France show essentially no change from 1994 to 2013 (**Figure 19**). IAGOS commercial aircraft observations show increases above Frankfurt in winter and autumn with little or no change in spring and summer (**Figure 16**), with broad upper tropospheric ozone increases across Europe on an annual basis from 1995 to 2013 (Cohen et al., 2018). In terms of TCO there is no consistent trend among the ozonesonde and satellite products, and FTIR and Umkehr observations show no change between 1995 and 2016 in France and Switzerland (**Figure 21**). Similar to mid-

latitude North America, ozone changes vary across Europe both spatially and seasonally, precluding any generalized statement regarding ozone trends across this region.

5.3. East Asia

In this section East Asia refers to mainland China, Hong Kong, Taiwan, South Korea and Japan; the region of Southeast Asia (i.e. Vietnam, Malaysia and Thailand) will be discussed in Section 5.4 which focuses on the NH tropics. After decades of emissions increases (Zhao et al., 2013), several recent studies have documented the rapid reduction of NO_x emissions in some regions of China since about 2011, as observed by satellites (Duncan et al., 2016; Krotkov et al., 2016; Liu et al., 2016; Miyazaki et al., 2017; van der A et al. 2017), but from the limited in situ observations there is no evidence of a recent decrease of surface ozone in China, possibly due to ozone production being VOC limited in this region (Ma et al., 2016; Sun et al., 2016; Li et al., 2017; Wang et al., 2017). In the case of Hong Kong, expected ozone decreases due to local precursor emissions reductions have been countered by transport of increasing ozone from southern and eastern China over the period 2002–2013 (Xue et al., 2014). As described in Section 4.1 the three long-term monitoring sites available from mainland China show ozone increases since the 1990s and early 2000s. As shown in **Figures 14** and **15**, there are 3 non-urban sites in Hong Kong which show weak or no trends in all four seasons during 2000–2014, however analysis of daytime average ozone at these sites shows yearly ozone increases at two out of three sites. Trends across Taiwan, South Korea and Japan vary by season but positive trends outweigh negative trends, and during the warm months of April–September the overall spatially weighted trend at rural sites is positive (Chang et al., 2017). Trends in the free troposphere are generally positive since the 1970s and 1980s through 2010, as recorded by Japanese ozonesondes from Tsukuba and Sapporo (Oltmans et al., 2013), and positive since the 1990s as recorded by IAGOS commercial aircraft above eastern China and South Korea (Ding et al., 2008; see also **Figure 18**), as well as in the UT across a broad region of East Asia (Cohen et al., 2018). In terms of TCO, the TOST ozonesonde product shows widespread increases across east Asia between 2003 and 2012, however the 5 satellite products in **Figure 24** do not indicate a consistent trend; at most 4 of the 6 products (TOST, OMI/MLS, OMI-RAL, OMI-SOA) indicate positive trends over portions of south and east China (**Figure 25**), while only one product (IASI-FORLI) indicates negative trends, confined to Japan and portions of northern China. In contrast to mid-latitude North America and western Europe, the majority of observational evidence for East Asia points toward a general increase of ozone since the 1990s or the year 2000, however further research is required to assess the impact of recent ozone precursor reductions on long-term ozone trends.

5.4. Northern Hemisphere tropics

Outside of the southern United States there are very few surface ozone monitors in the NH tropics (here defined as 0°–30°N), and these sites give no indication of a clear surface trend across this latitude band in either summer or winter (**Figure 13**). In the free troposphere, IAGOS aircraft show strong ozone increases above India and Southeast Asia from the period 1994–2004 to 2005–2014 (**Figure 18**). Increases in the 0–12 km column reached as high as 70% above Southeast Asia during summer, however this apparently large increase should be kept in perspective because the initial ozone values during 1994–2004 were very low compared to other regions of the world, especially mid-latitudes. The TOST ozonesonde product shows widespread TCO increases from the Arabian Sea eastwards to the dateline (**Figure 24**). Ozone increases in this region are also detected by many of the satellite products, especially over Southeast Asia (**Figure 25**), with five grid cells above this region showing a significant positive trend by all six products in **Figure 24**. For the IASI-FORLI product the increase is tied to climate variability over its short record (2008–2016) associated with the well-known ENSO-related ozone fluctuations in this region (Ziemke et al., 2015; Wespes et al., 2017). However, for the products with longer records (OMI-RAL and OMI/MLS since 2005, TOST since 1998, and GOME/OMI since 1996) the increase persists over several ENSO cycles.

5.5. Southern Hemisphere tropics

Long-term surface ozone monitoring in the SH tropics is even more limited than in the NH tropics, with only American Samoa in the western South Pacific Ocean showing a significant increase in DJF and JJA (**Figure 13**). The TOST ozonesonde product across this region largely reflects observations from NASA's Southern Hemisphere ADditional OZonesondes (SHADOZ) network (Thompson et al., 2007; Thompson et al., 2012; Thompson et al., 2017; Witte et al., 2017) showing significant increases of TCO since 2003 above the Amazon and from Madagascar eastward to the dateline (**Figure 24**). SHADOZ ozonesondes from the sub-tropical Irene, South Africa site (1990–2007) and the tropical Réunion Island station (1992–2012) showed strong increases (25–40% per decade) in mid- and upper-tropospheric ozone during winter, JJA (Thompson et al., 2014). Back-trajectories from Réunion, in particular, suggested that air masses from Southeast Asia might contribute to this increase. No trend was found during the spring (SON) fire season (Thompson et al., 2014).

Most of the satellite products also show ozone increases across these same general regions but with a high degree of spatial variability. **Figure 25** shows that 4–5 out of the six ozonesonde and satellite products indicate increasing ozone above the Amazon, and much of the area from southern Africa eastward to the dateline. TCO decreases are indicated by 1–2 products above South Africa and the eastern South Pacific. The evidence seems to indicate a general increase of ozone across much of the SH tropics through 2016. Attribution analysis has not yet been conducted to investigate these recent trends but previous observational and modelling work provides insight into the dominant ozone sources. Enhanced ozone and ozone precursors above the tropical South Atlantic Ocean as well as adjoining regions of South America and Africa have

been observed and studied for the past 30 years (Logan et al., 1985, 1986; Fishman et al., 1991; Jacob et al., 1996; Moxim et al., 2000; Thompson et al., 2000, 2007; Swap et al., 2003; Sauvage et al., 2005, 2007). Very recent work has used an atmospheric chemistry model to quantify the contribution of the stratosphere, biomass burning and anthropogenic emissions on the SH ozone enhancements (J. Liu et al., 2016, 2017). Briefly, the enhancement centered on 30°S stretching from Africa to Australia (most prominent in SH spring (SON), see Figures S-9–S-14) is primarily due to ozone in the UT originating from stratosphere-troposphere exchange along the subtropical jet. These processes cause interannual variability of ozone, however further work is required to see if they are related to trends. The stratosphere also makes strong contributions to UT ozone across the South Atlantic Ocean from 20°–30°S, but stratospheric influence is much less north of 20°S (i.e. beyond the subtropical jet). Beyond these regions of stratospheric influence, the SH ozone enhancement is produced from ozone precursors of anthropogenic, biomass burning and lightning origins with relative contributions that vary seasonally. In the past, quantification of ozone changes in this region has been limited by spatially and temporally sparse in situ observations. However, the IAGOS program now has increased availability of flights from the NH to South America and Australia. These observations, when combined with SHADOZ ozonesondes, may provide a sufficient density of observations to allow for robust trend evaluation of both ozone and ozone precursors.

5.6. Mediterranean and Middle East summertime ozone maximum

Some of the world's greatest summertime TCO values are found above the Mediterranean basin (Zbinden et al., 2013; see also **Figure 22** and Figures S-9–S-14), especially over the eastern half, with an extension towards the Persian Gulf. A more detailed view of satellite-detected ozone across the Mediterranean is also available from TES, GOME-2 (J. J. Liu et al., 2009; Worden et al., 2009; Richards et al., 2013) and IASI (Safieddine et al., 2014; Doche et al., 2014). Aircraft profiles above the eastern Mediterranean show that summertime ozone has typical values of 36, 51 and 67 nmol mol^{-1} (10^{th}, 50^{th} and 90^{th} percentiles, respectively) at the surface, increasing to 40, 65 and 110 nmol mol^{-1} (respectively) at 300 hPa (Kalabokas et al., 2007). Similarly, lidar/ECC profiles at OHP on the western side of the Mediterranean summer maximum show typical values of 35, 50, 70 nmol mol^{-1} (5^{th}, 50^{th}, 95^{th} percentiles) at the surface, increasing to 55, 80, 95 nmol mol^{-1} (**Figure 19**) at 300 hPa. Previous research has characterized the summertime Mediterranean region (Lelieveld et al., 2002), as well as the adjoining Middle East (Li et al., 2001), as a crossroads where ozone from many different sources can accumulate. Much of this understanding was derived from the August, 2001 Mediterranean INtensive Oxidant Study (MINOS), a time when NH ozone precursor emissions were much different from today (Hoesly et al., 2018). Scientists determined that Asia, particularly India and Southeast Asia, was a source for upper tropospheric pollution above the eastern Mediterranean (Scheeren et al., 2003). This pollution was linked to the Asian summer monsoon followed by transport across northern Africa and a southerly approach to the Mediterranean. In spite of high pollution levels in the Asian plume over the eastern Mediterranean, ozone was relatively low (55 nmol mol^{-1}) compared to the seasonal median, but similar to ozone observed in the UT above South and Southeast Asia during 1994–2004. Ozone in the Asian plume showed no clear relationship with higher hydrocarbons, suggesting a NO_x-limited photochemical regime (Scheeren et al., 2003), but modeling indicated that the quantity of ozone from South and Southeast Asia would increase over time with increasing emissions. Ozone enhancements in the mid-troposphere were much greater, with a variety of sources including the stratosphere, lightning NO_x and North America (Roelofs et al., 2003). The model-estimated TCO above the eastern Mediterranean was 50 DU (similar to present-day satellite retrievals) with contributions from the stratosphere (30%), lightning (13%), Asia (7%), North America (8%) and Europe (14%).

In the boundary layer, the area is influenced by western and eastern European pollution via frequent northerly flow. Model experiments show that lower tropospheric summertime ozone throughout the region has greatest sensitivity to locally emitted NO_x, particularly in the west. High summertime rural surface ozone can occur over the eastern Mediterranean, especially on its eastern edge, affecting the air quality of major urban centers in the area (Zerefos et al., 2002; Kalabokas and Repapis, 2004). Analysis of IAGOS aircraft ozone profiles reveals that ozone is strongly influenced by synoptic meteorology (Kalabokas et al., 2007; Kalabokas et al., 2013; Kalabokas et al., 2015). During the highest ozone days over the eastern Mediterranean a large surface anticyclone is centered over N. Africa, extending over central and western Europe. In addition, strong summer anticyclonic subsidence in the lower troposphere, leading to enhanced ozone, has been reported over the eastern Mediterranean (Eremenko et al., 2008; Foret et al., 2009; Liu et al., 2009; Coman et al., 2012; Richards et al., 2013; Doche et al., 2014; Kleanthous et al., 2014; Safieddine et al., 2014; Zanis et al., 2014; Tombrou et at., 2015). Summer anticyclones in the area are also associated with the downward transport of UT ozone, especially at the interface with adjacent low pressure systems located over the eastern Mediterranean and Middle East (Kalabokas et al., 2013; Zanis et al., 2014; Tyrlis et al., 2014; Kalabokas et al., 2015). Summertime stratospheric intrusions are also common events above this region influencing both the upper and mid-troposphere (Stohl et al., 2003, Škerlak et al., 2014; Akritidis et al., 2016), as found for other seasons (Galani et al., 2003). In addition, a frequent midsummer peak of UT ozone is observed above northern Europe and the adjacent North Atlantic Ocean (Thouret et al., 2006; see also Fig. 3.2.1), which could serve as an ozone reservoir for the lower troposphere and boundary layer over the eastern Mediterranean through large-scale subsidence. Similarly, enhanced ozone during anticyclonic conditions has also been observed at rural locations in the central and western Mediterranean region (Kalabokas

et al., 2008; Sànchez et al., 2008; Schurmann et al., 2009; Velchev et al., 2011; Cristofanelli et al., 2013, 2015, 2017; Kalabokas et al., 2017), where summer subsidence seems to be weaker than over the eastern Mediterranean, but where frequent stagnant conditions enhance local photochemical ozone production. These conditions are often associated with heat-waves (Cristofanelli et al., 2015).

TOAR-*Climate* has no clear evidence for a trend in the summertime ozone maximum across the Mediterranean and the Middle East. The five ozonesonde and satellite products (Figures S-23–S-27) with trends calculated for summertime show no consensus on the sign or magnitude of the ozone change. Surface ozone monitoring is limited across the Mediterranean with the few available sites generally showing decreasing ozone along the northern edge of the region and decreasing ozone at Cyprus (**Figure 15a**). Of the five sites in the eastern Mediterranean one shows a significant increase of ozone and the other four show no sign of a significant decrease. There are no sites available for trend evaluation east of Israel and the West Bank. Improved understanding of the magnitude, extent and trends of this ozone feature would require additional surface ozone monitoring in Egypt and in the Middle Eastern nations east of Israel. In the free troposphere IAGOS aircraft profiles are too infrequent for the exploration of trends, and routine profiling would be required to assess long term trends.

5.7. Tropospheric ozone burden

The Atmospheric Chemistry and Climate Model Intercomparison Project (ACCMIP) calculated the present-day radiative forcing due to tropospheric ozone using a model ensemble of global ozone simulations for the years 1850 and 2000 (Young et al., 2013). The 15-model mean of the year 2000 global tropospheric ozone burden (TOB) was 337 Tg, with a range of 302–378 Tg. Model performance for the present-day (2000) horizontal TCO distribution (and for TOB) was evaluated using only the OMI/MLS product. Through TOAR we now have 6 products (TOST and the five satellite products) for quantifying present-day TOB. **Figure 26** compares TOB (60°S–60°N) among the five satellite products discussed above with the addition

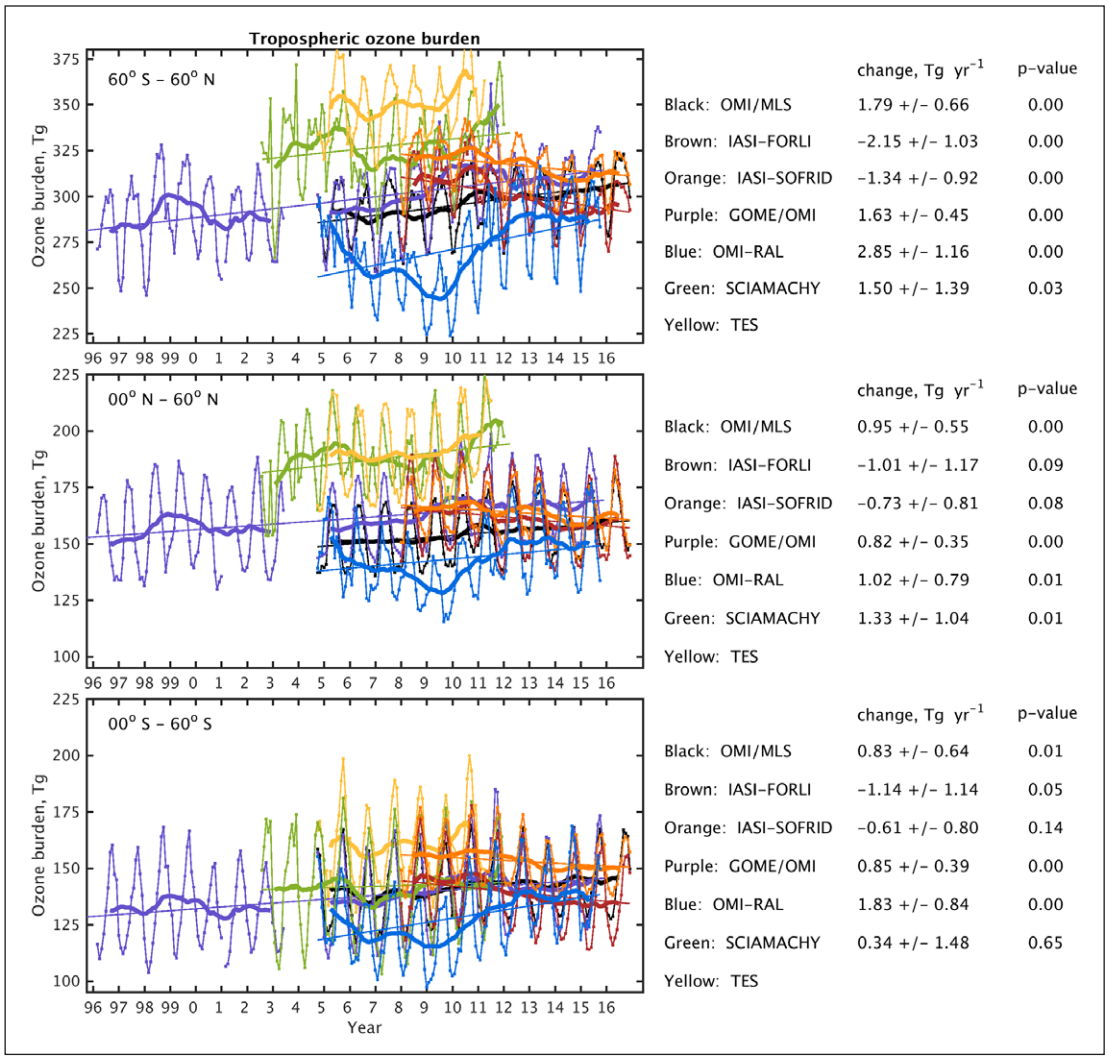

Figure 26: Monthly TOB (Tg) per latitude band. Monthly tropospheric ozone burden (TOB) (thin curves) for 60°S–60°N (top), 00°N–60°N (middle), and 00°S–60°S (bottom), for seven different satellite products. Thick curves are the 12-month running means and the thin straight lines are the least square linear fits. Trends (Tg yr^{-1}) in this figure are based on least-squares linear regression and reported with 95% confidence intervals and p-values. DOI: https://doi.org/10.1525/elementa.291.f26

of SCIAMACHY (2002–2012) and GOME (1996–2003) to provide as much information as possible on ozone prior to the operational periods of OMI and IASI. Across the globe and in both hemispheres (see also Figures S-28 and S-29) the products come into closer agreement after 2014.

Present-day TOB estimation: Table 5 shows TOB for 2010–2014 (corresponding to **Figure 10**) in the latitude range of 60°S–60°N. The mean of the six products (including TOST) is 302 Tg with a range of 281–318 Tg, or roughly ± 6%. The mean of just the five satellite products is 301 Tg with a range of 281–318 Tg, or roughly ± 6%. The ozone burden from the five satellite products for the most recent period of 2014–2016 is 300 Tg, with an even narrower range of 287–311 Tg, or ± 4%.

The TOB results discussed so far are limited to the 60°S–60°N latitude range and therefore do not provide estimates of the true global TOB. However, TOST covers the polar regions and provides a full global TOB estimate of 337 Tg (for 2010–2012), which means the TOST estimate of TOB in the range of 60°S–60°N is 91% of the global TOB. Therefore, the polar regions, although they represent 13% of the globe, contain 9% of the global TOB. The IASI-SOFRID and IASI-FORLI products provide polar coverage and their full latitude range TOB values are 333 and 345 Tg, respectively, but these results are underestimates as only daytime IASI retrievals are used in this study, which excludes regions under polar night conditions (see Section 2.5.5). Despite potentially large differences for different satellite observations of a single air mass, as described in section 2.5, the global TOB estimates in **Table 5** are remarkably consistent.

TOB trends estimation: While the satellite products have excellent agreement for the present-day TOB, they differ in their quantification of TOB trends. The OMI/MLS, GOME/OMI and OMI-RAL products indicate an increase of TOB through 2015–2016, while IASI-FORLI and IASI-SOFRID indicate a decrease. As described below, the satellite products have differing vertical sensitivities and therefore the trends reflect ozone changes at different levels of the troposphere. At this time, we are unable to provide a definitive statement regarding the change in TOB over the past decade and future work is required to reconcile the different satellite products. However many of the products indicate TCO increases across the portion of the tropics stretching from South America eastwards to the western Pacific Ocean, a region that deserves further investigation as it has experienced rapid changes in ozone precursor emissions and is sensitive to dynamical controls (e.g, ENSO) on ozone interannual variability.

Trend determination can have errors due to time-varying instrument biases that are not completely removed, if at all, by time dependent corrections in the retrievals. Understanding the contribution of instrument biases to trend differences requires further validation using in-situ

Table 5: Multi-year mean tropospheric ozone burden (Tg) as measured by ozonesondes and satellites[a]. DOI: https://doi.org/10.1525/elementa.291.t5

	60°S–60°N			Full latitude range		
	2000	**2010–2014**	**2014–2016**	**2000**	**2010–2014**	**2014–2016**
TOST		306	NA		337 90°S–90°N	NA
OMI/MLS		300	304		–	–
OMI-SAO		305	303			
OMI-RAL		281	287			
IASI-FORLI		301	293		333 90°S–90°N	324 90°S–90°N
IASI-SOFRID		318	311		345 75°S–75°N	338 75°S–75°N
Mean (range), all six products		302 (281–318)				
Mean (range), five satellite products		301 (281–318)	300 (287–311)			
ACCMIP model ensemble	299 ± 21[b]			337 ± 23 90°S–90°N		

[a] Also shown is the mean and standard deviation of TOB from the ACCMIP model ensemble for the year 2000 (Young et al., 2013). IASI-FORLI and IASI-SOFRID TOB values for their full latitude range are underestimates due to missing data during polar night.

[b] Personal communication from Paul Young, Lancaster University.

observations with sufficiently long records, as has been done with ozonesondes for the stratosphere (Steinbrecht et al., 2017). Differences in vertical sensitivity and sampling will also affect trend estimation. For example, TCO observations with greater sensitivity to the UT have trends with greater influence from this region. This sensitivity difference might help to explain the trend differences observed for UV and thermal infrared measurements (see **Figures 23** and **26**). Resolving trend differences due to these measurement traits requires characterizing the effects of sampling and vertical sensitivity on trend estimates. This can be taken into account by sampling and applying the AKs of each measurement type to a common model simulation with a known trend in TCO to find the resulting trend bias, if any. These validation and model sampling exercises will be the focus of future intercomparisons of remotely sensed TCO data products.

5.8 Tropospheric ozone's long-wave radiative effect

TOAR-Climate concludes with a presentation of tropospheric ozone's top-of-atmosphere (TOA) long-wave radiative effect (LWRE), as estimated by the IASI instrument (**Figure 27**) (Doniki et al., 2015). LWRE quantifies the present day tropospheric ozone greenhouse effect, and its spatial variability is due to variations in tropospheric ozone combined with other factors that affect the sensitivity of TOA radiance to ozone absorption such as surface temperature, atmospheric temperature and water vapor (Worden et al., 2008; Worden et al., 2011; Doniki et al., 2015; Kuai et al., 2017). The spatial variation of LWRE in **Figure 27**, indicates that the highest values, combining both tropospheric ozone and TOA sensitivity to tropospheric ozone, are over land and in the Northern Hemisphere (NH). Satellite-detected ozone LWRE is a key benchmark for the atmospheric chemistry models used to calculate tropospheric ozone's radiative forcing, and it can also be used with models to understand the radiative impact of changes in ozone precursor emissions (Bowman and Henze, 2012). The LWRE depicted in **Figure 27** is calculated from the IASI-FORLI tropospheric ozone product and we note that LWRE will vary somewhat depending on which satellite product in **Figure 10** is used in its calculation due to sampling, time of day and retrieval differences. Because LWRE is sensitive to the vertical and horizontal distribution of ozone (Worden et al., 2008; Worden et al., 2011; Doniki et al., 2015; Kuai et al., 2017) satellite estimates of LWRE can be evaluated and improved with high frequency in situ tropospheric ozone profiles if they can provide a detailed view of the vertical ozone gradient on seasonal time scales. According to **Figure 27** the strongest LWRE values are found above tropical and subtropical regions, which have limited ozone observations at the surface (compare **Figure 27** to **Figure 1**) and in the free troposphere (TOAR-*Observations*, Tarasick et al., 2018). Presently, routine ozonesondes are launched by NASA's Southern Hemisphere ADditional OZonesondes (SHADOZ) network (Thompson et al., 2007; Witte et al., 2017) with thirteen sites that provide observations across the northern and southern tropics, but no measurements above northern Africa, the Middle East or western Australia. The IAGOS commercial aircraft program does provide flights in the UT across northern Africa and the Middle East as well as other regions of the tropics. Most of the data are limited to the 11–12 km cruise altitude of the aircraft, but frequent vertical profiles are now available from several Middle Eastern airports and to a lesser extent, India. When combined, the IAGOS and SHADOZ programs provide crucial data for evaluating satellite retrievals of TCO and

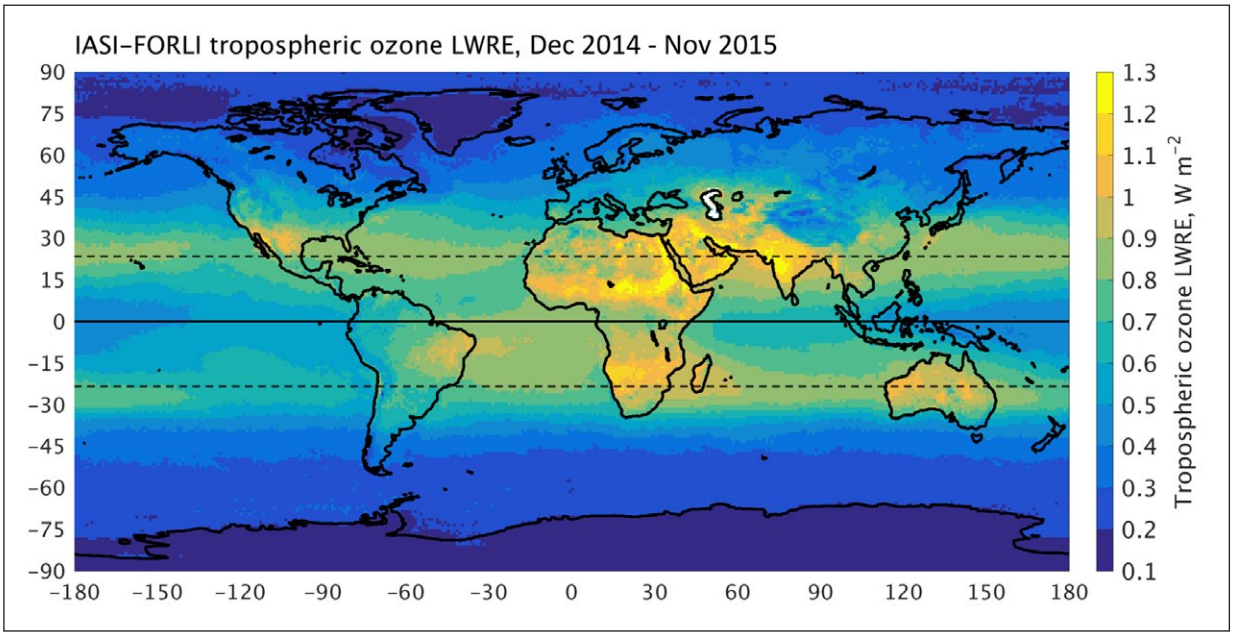

Figure 27: Clear-Sky (cloud cover <13%) ozone long wave radiative effect (LWRE). Clear-sky (cloud cover < 13%) ozone LWRE (W m^{-2}) as estimated from IASI measurements shows the present day greenhouse effect of tropospheric ozone. The spatial variability of LWRE is due to variations in tropospheric ozone, surface temperature, atmospheric temperature and water vapor. Data are averaged from December 2014 to November 2015 on a 1° × 1° grid. DOI: https://doi.org/10.1525/elementa.291.f27

Table 6: Availability of all data sets presented in TOAR-Climate. DOI: https://doi.org/10.1525/elementa.291.t6

In situ observations	
Surface ozone observations	The surface ozone values and trends shown in Figures 1, 2, 3, 13, 14, 15 (as well as the figures themselves) can be downloaded from: Schultz, MG; Schröder, S; Lyapina, O et al. (2017): Tropospheric Ozone Assessment Report, links to datasets https://doi.pangaea.de/10.1594/PANGAEA.876108
TOST ozonesonde product	The global monthly gridded product is available from the World Ozone and Ultraviolet Radiation Data Centre (WOUDC): http://woudc.org/archive/products/ozone/vertical-ozone-profile/ozonesonde/1.0/tost/
IAGOS commercial aircraft	High resolution IAGOS observations can be downloaded from the IAGOS Data Portal: http://iagos.sedoo.fr/
Mauna Loa Observatory ozone and meteorology	Hourly ozone and meteorological data shown in Figure 12 are available from NOAA's Global Monitoring Division: https://www.esrl.noaa.gov/gmd/dv/ftpdata.html
Lauder, NZ ozonesondes	The ozonesonde data at Lauder are part of WOUDC and the Network for the Detection of Atmospheric Composition Change (NDACC) and are publicly available: http://woudc.org/data/explore.php, ftp://ftp.cpc.ncep.noaa.gov/ndacc/station/lauder/ames/o3sonde/.
Surface-based remote sensing	
Table Mountain lidar	Data used in this publication are archived with NDACC and are publicly available (see http://www.ndacc.org; Leblanc, 2016). For additional data or information please contact the authors. Leblanc, T.: TMO lidar data at NDACC database, available at: ftp://ftp.cpc.ncep.noaa.gov/ndacc/station/tmo/ames/lidar/, last access: 25 July 2016.
OHP ozonesondes and lidar	Data used in this publication are archived with NDACC and are publicly available: http://www.ndacc.org
FTIR	Profiles with 40–50 levels archived at NDACC database: http://www.ndsc.ncep.noaa.gov/data/ , https://www2.acom.ucar.edu/irwg
Umkehr	http://www.woudc.org/, stray light corrected monthly averaged data from six Umkehr stations are provided by NOAA/ESRL/GMD at ftp://aftp.cmdl.noaa.gov/data/ozwv/DobsonUmkehr/Stray%20light%20corrected/monthlymean/
Satellite products	
OMI/MLS	Monthly gridded data at 1° × 1.25° resolution available from NASA Goddard Space Flight Center: https://acd-ext.gsfc.nasa.gov/Data_services/cloud_slice/
GOME and OMI from SAO	Monthly GOME gridded data are available at https://www.cfa.harvard.edu/~xliu/res/gmtrop.htm. Monthly gridded data at 1° × 1.25° resolution are derived from OMI OMPROFOZ data. OMI OMPROFOZ data are available from Aura Validation Data Center, NASA Goddard Space Flight Center: https://avdc.gsfc.nasa.gov/index.php?site=1389025893&id=74
OMI-RAL	Data are available at http://www.ceda.ac.uk/ and in a near future at http://climate.copernicus.eu/climate-data-store
IASI-FORLI	http://cds-espri.ipsl.upmc.fr/etherTypo/index.php?id=1719&L=1
IASI-SOFRID	v1.5 ozone data are available online at http://thredds.sedoo.fr/iasi-sofrid-o3-co/
SCIAMACHY	Data are available from the Institute of Environmental Physics, University of Bremen on request
IASI LWRE	Archive under development
IASI-LISA	Data are available from the Laboratoire Interuniversitaire des Systèmes Atmosphériques (LISA, CNRS-UPEC-UPD) upon request. Contact: cuesta@lisa.u-pec.fr
IASI+GOME-2, LISA	These data are now being produced routinely and will soon be available at http://www.aeris-data.fr. Until then, the data will be made available from the Laboratoire Interuniversitaire des Systèmes Atmosphériques (LISA, CNRS-UPEC-UPD) upon request. Contact: cuesta@lisa.u-pec.fr
TES	Ozone vertical profiles, total column, tropospheric column for single observations with 5 km × 8 km horizontal resolution (L2) and daily/monthly averaged, gridded (L3) products. Global observations for 2004–2009; Megacity and other regions of interest for 2010-present. available at: https://eosweb.larc.nasa.gov/project/tes/tes_table
TOR (Tropospheric Ozone Residual satellite product)	Monthly gridded data at 1° × 1.25° resolution available from NASA Langley Research Center: https://science.larc.nasa.gov/TOR/

refining LWRE estimates above many sites in the tropics and subtropics, but large data gaps still remain, especially above northern Africa and western Australia.

5.9. Data Availability

The goal of *TOAR-Climate* is to assess the present-day distribution and trends of tropospheric ozone for the purposes of quantifying TOB and to identify additional observations well-suited for the evaluation of global atmospheric chemistry models. Our current observation-based knowledge of ozone's distribution and trends has been covered as succinctly as possible in Sections 3, 4 and 5 and those findings will not be repeated here. Instead we highlight the fact that the global ozone observational network has enormous spatial gaps with respect to surface observations and in situ vertical profiles (Laj et al., 2009; Sofen et al., 2016). While several new satellite products now provide near global coverage of TCO further work is required to determine why the satellite products differ with regard to trends. Therefore, global atmospheric chemistry models will continue to be critical tools for our understanding of not only the global distribution of tropospheric ozone but also the photochemical and dynamical processes that drive photochemical ozone production and loss, surface deposition and stratosphere-troposphere exchange (see *TOAR-Model Performance*, Young et al., 2018). The ozone data sets described in *TOAR-Climate* are ideal for evaluating the performance of global atmospheric chemistry models and access to these valuable data is described in **Table 6**.

Data Accessibility Statements

Information to access all datasets used in the TOAR-Climate analyses can be found in Table 6.

Supplemental Files

The supplementary files for this article can be found as follows:

- **Figures S1–S29.** Tropospheric Ozone Assessment Report: Present-day distribution and trends of tropospheric ozone relevant to climate and global atmospheric chemistry model evaluation. Doc. DOI: https://doi.org/10.1525/elementa.291.s1

Acknowledgements and Funding information

The TOST ozonesonde product relies on observations made by many institutions, including NASA's Southern Hemisphere ADditional OZonesondes (SHADOZ) network, with data made available by Anne Thompson and Jacquie Witte, NASA GSFC: https://tropo.gsfc.nasa.gov/shadoz/. The TOST team gratefully acknowledges the NOAA Air Resources Laboratory for the provision of the HYSPLIT trajectory model (Hybrid Single Particle Lagrangian Integrated Trajectory Model) (http://www.arl.noaa.gov/ready.html), and the NOAA Physical Sciences Division for the NCEP/NCAR reanalysis data (www.esrl.noaa.gov/psd/data/reanalysis/reanalysis.shtml). Jack Fishman, St. Louis University, provided the 1979–1983 Tropospheric Ozone Residual product. The MLS, OMI and TES projects are supported by the National Aeronautics and Space Administration (NASA) Earth Observing System (EOS) Aura Program. IASI is a joint mission of EUMETSAT and the Centre National d'Etudes Spatiales (CNES, France). The IASI L1 data are distributed in near-real time by EUMETSAT through the EumetCast distribution system. LATMOS and ULB acknowledge support from the C3S-O_3 project funded by ECMWF and from the AC-SAF project funded by EUMETSAT. LISA acknowledges the support from CNES (Centre National des Etudes Spatiales)/TOSCA (Terre Océan Surface Continentale Atmosphère), PNTS (Programme National de Télédétection Spatiale) and ANR (Agence Nationale de la Recherche – project: ANR-15-CE04-0005) for the development and production of ozone observations from IASI+GOME-2 and IASI. CMIP6 global NO_x emissions data were provided by CEDS (Community Emissions Data System): http://www.globalchange.umd.edu/ceds/.

Competing interests

The authors have no competing interests to declare.

Author contributions

- **Contributed to conception and design**: AG, ORC, MGS, DWT
- **Contributed to acquisition of data**: MGS, JPB, AMT, DJ, JJS, RQ, GZ, CV, ELF, MS, JL, DH, PFC, MP, FH, JWH, EM, OG, NJ, DS, CV, GA, VT, HP, BB, JC, DWT, AB, EC, GD, GH, BK, SK, BL, TL, WL, XL, AMB, MO, IP, NR, AR, JS, RS, HT, TT, CW, XX, GZ, JZ
- **Contributed to analysis and interpretation of data**: AG, ORC, MGS, JPB, PK, DJ, CV, DH, PFC, CW, CC, AB, NR, AR, JL, MJGM, MP, FH, JWH, EM, OG, NJ, DS, CV, FE, GA, VT, HP, BB, GD, JC, BH, DWT, EW, HW, EC, SD, GH, BK, BL, TL, XL, IP, RQ, TT, CW, XX, GZ, JZ
- **Drafted and/or revised the article**: AG, ORC, MGS, PK, MS, CW, CC, NR, AR, JL, MJGM, CV, FE, GA, VT, HP, BB, GD, JC, JLN, BH, DWT, HW, GF, GH, DJ, BK, TL, XL, IP, TT, CW, XX, JZ

References

Akritidis, D, et al. 2016. On the role of tropopause folds in summertime tropospheric ozone over the eastern Mediterranean and the Middle East. *Atmos. Chem. Phys.* **16**: 14025–14039. DOI: https://doi.org/10.5194/acp-16-14025-2016

Ancellet, G and **Beekmann, M.** 1997. Evidence for changes in the ozone concentrations in the free troposphere over Southern France from 1976 to 1995. *Atmos. Environ.* **31**: 2835–851. DOI: https://doi.org/10.1016/S1352-2310(97)00032-0

Andrey, J, Cuevas, E, Parrondo, MC, Alonso-Pérez, S, Redondas, A and **Gil-Ojeda, M.** 2014. Quantification of ozone reductions within the Saharan air layer through a 13-year climatologic analysis of ozone profiles. *Atmospheric Environment* **84**: 28–34. DOI: https://doi.org/10.1016/j.atmosenv.2013.11.030

Archibald, A, Elshorbany, Y, et al. 2018. Tropospheric Ozone Assessment Report: Critical review of the present-day and near-future tropospheric ozone budget. Manuscript in preparation.

Attmannspacher, W and **Dütsch, HU.** 1970. International ozone sonde intercomparison at the observatory Hohenpeissenberg 19 January–5 February 1970, Offenbach am Main Selbstverl. des Dt. Wetterdienstes, 11, 74 S.–Berichte des Deutschen Wetterdienstes 120, MAB0014.001: MOP Per **18**(120). MAB0455.001: 120, ISBN:3881480951.

August, T, et al. 2012. IASI on Metop-A: Operational Level 2 retrievals after five years in orbit. *Journal of Quantitative Spectroscopy and Radiative Transfer* **114**(11): 1340–1371. DOI: https://doi.org/10.1016/j.jqsrt.2012.02.028

Balashov, NV, Thompson, AM, Piketh, SJ and **Langerman, KE.** 2014. Surface ozone variability and trends over the South African Highveld from 1990 to 2007. *J. Geophys. Res. Atmos.* **119**: 4323–4342. DOI: https://doi.org/10.1002/2013JD020555

Banerjee, A, et al. 2016. Drivers of changes in stratospheric and tropospheric ozone between year 2000 and 2100. *Atmos. Chem. Phys.* **16**: 2727–2746. DOI: https://doi.org/10.5194/acp-16-2727-2016

Barnes, EA, Fiore, AM and **Horowitz, LW.** 2016. Detection of trends in surface ozone in the presence of climate variability. *J. Geophys. Res. Atmos.* **121**: 6112–6129. DOI: https://doi.org/10.1002/2015JD024397

Barret, B, Le Flochmoen, E, Sauvage, B, Pavelin, E, Matricardi, M and **Cammas, JP.** 2011. The detection of post-monsoon tropospheric ozone variability over south Asia using IASI data. *Atmos. Chem. Phys.* **11**: 9533–9548. DOI: https://doi.org/10.5194/acp-11-9533-2011

Beer, R, et al. 2001. Tropospheric emission spectrometer for the Earth Observing System's Aura satellite. *Appl. Opt.* **40**: 2356–2367. DOI: https://doi.org/10.1364/AO.40.002356

Berntsen, TK, Isaksen, ISA, Myhre, G, Fuglestvedt, J, Stordal, F, Larsen, T, Freckleton, R and **Shine, KP.** 1997. Effects of anthropogenic emissions on tropospheric ozone and its radiative forcing. *J. Geophys. Res.* **102**: 28101–28126. DOI: https://doi.org/10.1029/97JD02226

Bethan, S, Vaughan, G and **Reid, SJ.** 1996. A comparison of ozone and thermal tropopause heights and the impact of tropopause definition on quantifying the ozone content of the troposphere. *Q. J. Royal Met. Soc.* **122**: 929–944. DOI: https://doi.org/10.1002/qj.49712253207

Blunden, J and **Arndt, DS.** (eds) 2017. State of the Climate in 2016. Bull. *Amer. Meteor. Soc.* **98**(8): Si–S277. DOI: https://doi.org/10.1175/2017BAMSStateoftheClimate.1

Borbas, EE and **Ruston, BC.** 2010. The RTTOV UWiremis IR land surface emissivity module, AS Mission Report NWPSAF-MO-VS-042, EUMETSAT Numerical Weather Prediction Satellite Applications Facility, Met Office, Exeter, U.K.

Bovensmann, H, Burrows, JP, Buchwitz, M, Frerick, J, Noël, S, Rozanov, VV, Chance, KV and **Goede, APH.** 1999. SCIAMACHY: mission objectives and measurement modes. *J. Atmos. Sci.* **56**: 127–150. DOI: https://doi.org/10.1175/1520-0469(1999)056<0127:SMOAMM>2.0.CO;2

Bowman, K and **Henze, DK.** 2012. Attribution of direct ozone radiative forcing to spatially resolved emissions. *Geophys. Res. Lett.* **39**(L2): 2704. DOI: https://doi.org/10.1029/2012GL053274

Bowman, KW. 2013. Toward the next generation of air quality monitoring: *Ozone. Atmos. Environ.* **80**: 571–583. DOI: https://doi.org/10.1016/j.atmosenv.2013.07.007

Bowman, KW, et al. 2013. Evaluation of ACCMIP outgoing longwave radiation from tropospheric ozone using TES satellite observations. *Atmos. Chem. Phys.* **13**: 4057–4072. DOI: https://doi.org/10.5194/acp-13-4057-2013

Boynard, A, et al. 2016. Seven years of IASI ozone retrievals from FORLI: validation with independent total column and vertical profile measurements. *Atmos. Meas. Tech.* **9**: 4327–4353. DOI: https://doi.org/10.5194/amt-9-4327-2016

Boynard, A, Hurtmans, D, Garane, K, Goutail, F, Hadji-Lazaro, J, Koukouli, ME, Wespes, C, Keppens, A, Pommereau, J-P, Pazmino, A, Balis, D, Loyola, D, Valks, P, Coheur, P-F and **Clerbaux, C.** 2018. Validation of the IASI FORLI/Eumetsat ozone products using satellite (GOME-2), ground-based (Brewer-Dobson, SAOZ) and ozonesonde measurements. *Atmos. Meas. Tech. Discuss.*, in review. DOI: https://doi.org/10.5194/amt-2017-461

Brasseur, GP and **Prinn, RG.** 2003. Atmospheric Chemistry in a Changing World: An Integration and Synthesis of a Decade of Tropospheric Chemistry Research; the International Global Atmospheric Chemistry Project of the International Geosphere-Biosphere Programme. *Springer Science & Business Media.* DOI: https://doi.org/10.1007/978-3-642-18984-5

Brown-Steiner, B and **Hess, P.** 2011. Asian influence on surface ozone in the United States: A comparison of chemistry, seasonality, and transport mechanisms. *J. Geophys. Res.* **116**(D17): 309. DOI: https://doi.org/10.1029/2011JD015846

Burrows, JP, et al. 1999. The Global Ozone Monitoring Experiment (GOME): Mission concept and first scientific results. *J. Atmos. Sci.* **56**(2): 151–175. DOI: https://doi.org/10.1175/1520-0469(1999)056<0151:TGOMEG>2.0.CO;2

Burrows, JP, Hölzle, E, Goede, A, Visser, H and **Fricke, W.** 1995. SCIAMACHY–scanning imaging absorption spectrometer for atmospheric chartography. *Acta Astronaut.* **35**: 445–451. DOI: https://doi.org/10.1016/0094-5765(94)00278-T

Burrows, JP, Platt, U and **Borrell, P.** 2011. Tropospheric Remote Sensing from Space. In: *The Remote Sensing of Tropospheric Composition from Space.* Springer: Berlin Heidelberg, 1–65. DOI: https://doi.org/10.1007/978-3-642-14791-3_1

Chang, K-L, Petropavlovskikh, I, Cooper, OR, Schultz, MG and **Wang, T.** 2017. Regional trend analysis

of surface ozone observations from monitoring networks in eastern North America, Europe and East Asia. *Elem Sci Anth.* **5**(50). DOI: https://doi.org/10.1525/elementa.243

Clerbaux, C, Boynard, A, Clarisse, L, George, M, Hadji-Lazaro, J, Herbin, H, Hurtmans, D, Pommier, M, Razavi, A, Turquety, S, Wespes, C and **Coheur, P-F.** 2009. Monitoring of atmospheric composition using the thermal infrared IASI/MetOp sounder. *Atmos. Chem. Phys.* **9**: 6041–6054. DOI: https://doi.org/10.5194/acp-9-6041-2009

Cohen, Y, et al. 2018. Climatology and long-term evolution of ozone and carbon monoxide in the UTLS at northern mid-latitudes, as seen by IAGOS from 1995 to 2013. *Atmos. Chem. Phys.*, **18**: 5415–5453. DOI: https://doi.org/10.5194/acp-18-5415-2018

Coman, A, Foret, G, Beekmann, M, Eremenko, M, Dufour, G, Gaubert, B, Ung, A, Schmechtig, C, Flaud, J-M and **Bergametti, G.** 2012. Assimilation of IASI partial tropospheric columns with an Ensemble Kalman Filter over Europe. *Atmos. Chem. Phys.* **12**: 2513–2532. DOI: https://doi.org/10.5194/acp-12-2513-2012

Cooper, M, Martin, RV, Livesey, NJ, Degenstein, DA and **Walker, KA.** 2013. Analysis of satellite remote sensing observations of low ozone events in the tropical upper troposphere and links with convection. *Geophys. Res. Lett.* DOI: https://doi.org/10.1002/grl.50717

Cooper, OR, Gao, R-S, Tarasick, D, Leblanc, T and **Sweeney, C.** 2012. Long-term ozone trends at rural ozone monitoring sites across the United States, 1990–2010. *J. Geophys. Res.* **117**(D22): 307 DOI: https://doi.org/10.1029/2012JD018261

Cooper, OR, Parrish, DD, Ziemke, J, Balashov, NV, Cupeiro, M, Galbally, IE, Gilge, S, Horowitz, L, Jensen, NR, Lamarque, J-F, Naik, V, Oltmans, SJ, Schwab, J, Shindell, DT, Thompson, AM, Thouret, V, Wang, Y and **Zbinden, RM.** 2014. Global distribution and trends of tropospheric ozone: An observation-based review. *Elementa: Science of the Anthropocene* **2**. DOI: https://doi.org/10.12952/journal.elementa.000029

Cristofanelli, P, et al. 2015. Long-term surface ozone variability at Mt. Cimone WMO/GAW global station (2165 m a.s.l., Italy). *Atmos. Environ.* **101**: 23–33. DOI: https://doi.org/10.1016/j.atmosenv.2014.11.012

Cristofanelli, P, Busetto, M, Calzolari, F, Ammoscato, I, Gullì, D, Dinoi, A, et al. 2017. Investigation of reactive gases and methane variability in the coastal boundary layer of the central Mediterranean basin. *Elem Sci Anth.* **5**: 12. DOI: https://doi.org/10.1525/elementa.216

Cristofanelli, P, Fierli, F, Marinoni, A, Calzolari, F, Duchi, R, Burkhart, J, Stohl, A, Maione, M, Arduini, J and **Bonasoni, P.** 2013. Influence of biomass burning and anthropogenic emissions on ozone, carbon monoxide and black carbon at the Mt. Cimone GAW-WMO global station (Italy, 2165 m a.s.l.). *Atmos. Chem. Phys.* **13**: 15–30. DOI: https://doi.org/10.5194/acp-13-15-2013

Cuesta, J, Eremenko, M, Liu, X, Dufour, G, Cai, Z, Höpfner, M, von Clarmann, T, Sellitto, P, Foret, G, Gaubert, B, Beekmann, M, Orphal, J, Chance, K, Spurr, R and **Flaud, J-M.** 2013. Satellite observation of lowermost tropospheric ozone by multispectral synergism of IASI thermal infrared and GOME-2 ultraviolet measurements over Europe. *Atmos. Chem. Phys.* **13**: 9675–9693. DOI: https://doi.org/10.5194/acp-13-9675-2013

Cuevas, E, González, Y, Rodríguez, S, Guerra, JC, Gómez-Peláez, AJ, Alonso-Pérez, S, Bustos, J and **Milford, C.** 2013. Assessment of atmospheric processes driving ozone variations in the subtropical North Atlantic free troposphere. *Atmos. Chem. Phys.* **13**: 1973–1998. DOI: https://doi.org/10.5194/acp-13-1973-2013

De Wachter, E, Barret, B, Le Flochmoen, E, Pavelin, E, Matricardi, M, Clerbaux, C, Hadji-Lazaro, J, George, M, Hurtmans, D, Coheur, PF, Nedelec, P and **Cammas, JP.** 2012. Retrieval of MetOp-A/IASI CO profiles and validation with MOZAIC data. *Atmos. Mes. Tech.* **5**: 2843–2857. DOI: https://doi.org/10.5194/amt-5-2843-2012

Derwent, RG, et al. 2010. Ozone in Central England: the impact of 20 years of precursor emission controls in Europe. *Environ. Sci. Technol.* **13**: 195–204. DOI: https://doi.org/10.1016/j.envsci.2010.02.001

Derwent, RG, Manning, AJ, Simmonds, PG, Spain, TG and **O'Doherty, S.** 2018. Long-term trends in ozone in baseline and European regionally-polluted air at Mace Head, Ireland over a 30-year period. *Atmos. Environ.* **179**: 279–287. DOI: https://doi.org/10.1016/j.atmosenv.2018.02.024

Ding, AJ, et al. 2008. Tropospheric ozone climatology over Beijing: analysis of aircraft data from the MOZAIC program. *Atmos. Chem. Phys.* **8**: 1–13. DOI: https://doi.org/10.5194/acp-8-1-2008

Dobson, GMB. 1968a. The evaluation and elimination of errors in the measurement of total ozone when the sun is low, Atmospheric Physics, Clarendon Laboratory. Available at: http://www.atm.ox.ac.uk/user/barnett/Dobsonpapers/DobsonAtmosMemorandum68pt6November1968.pdf.

Dobson, GMB. 1968b. Forty Years: Research on Atmospheric Ozone at Oxford: a History. *Appl. Optics* **7**: 387–405. DOI: https://doi.org/10.1364/AO.7.000387

Doche, C, Dufour, G, Foret, G, Eremenko, M, Cuesta, J, Beekmann, M and **Kalabokas, P.** 2014. Summertime tropospheric-ozone variability over the Mediterranean basin observed with IASI. *Atmos. Chem. Phys.* **14**: 10589–10600. DOI: https://doi.org/10.5194/acp-14-10589-2014

Doherty, RM, Orbe, C, Zeng, G, Plummer, DA, Prather, MJ, Wild, O, Lin, M, Shindell, DT and **Mackenzie, IA.** 2017. Multi-model impacts of climate change on pollution transport from global emission source regions. *Atmospheric Chemistry and Physics*, **17**(23): 14219. DOI: https://doi.org/10.5194/acp-17-14219-2017

Doniki, S, Hurtmans, D, Clarisse, L, Clerbaux, C, Worden, HM, Bowman, KW and **Coheur, P-F.** 2015. Instantaneous longwave radiative impact of ozone: an application on IASI/MetOp observations. *Atmos. Chem. Phys.* **15**: 12971–12987. DOI: https://doi.org/10.5194/acp-15-12971-2015

Draxler, RR and **Hess, GD.** 1998. An overview of the HYSPLIT_4 modeling system for trajectories, dispersion and deposition. *Aust. Met. Mag.* **47**: 295–308.

Dufour, G, Eremenko, M, Cuesta, J, Doche, C, Foret, G, Beekmann, M, Cheiney, A, Wang, Y, Cai, Z, Liu, Y, Takigawa, M, Kanaya, Y and **Flaud, J-M.** 2015. Springtime daily variations in lower-tropospheric ozone over east Asia: the role of cyclonic activity and pollution as observed from space with IASI. *Atmos. Chem. Phys.* **15**: 10839–10856. DOI: https://doi.org/10.5194/acp-15-10839-2015

Dufour, G, Eremenko, M, Griesfeller, A, et al. 2012. Validation of three different scientific ozone products retrieved from IASI spectra using ozonesondes. *Atmos. Mes. Tech.* **5**: 611–630. DOI: https://doi.org/10.5194/amt-5-611-2012

Dufour, G, Eremenko, M, Orphal, J and **Flaud, J-M.** 2010. IASI observations of seasonal and day-to-day variations of tropospheric ozone over three highly populated areas of China: Beijing, Shanghai, and Hong Kong. *Atmos. Chem. Phys.* **10**: 3787–3801. DOI: https://doi.org/10.5194/acp-10-3787-2010

Duncan, BN, Lamsal, LN, Thompson, AM, Yoshida, Y, Lu, Z, Streets, DG, Hurwitz, MM and **Pickering, KE.** 2016. A space-based, high-resolution view of notable changes in urban NO_x pollution around the world (2005–2014). *J. Geophys. Res.* **121**: 976–96. DOI: https://doi.org/10.1002/2015JD024121

Ebojie, F. 2014. Tropospheric ozone columns retrieval from SCIAMACHY limb-nadir-matching observations (PhD dissertation), Universität Bremen: Physik/Elektrotechnik. Available at: https://elib.suub.uni-bremen.de/peid=D00104050-1.pdf (last access: 18 August 2017).

Ebojie, F, Burrows, JP, Gebhardt, C, Ladstätter-Weißenmayer, A, von Savigny, C, Rozanov, A, Weber, M and **Bovensmann, H.** 2016. Global tropospheric ozone variations from 2003 to 2011 as seen by SCIAMACHY. *Atmos. Chem. Phys.* **16**: 417–436. DOI: https://doi.org/10.5194/acp-16-417-2016

Ebojie, F, von Savigny, C, Ladstätter-Weißenmayer, A, Rozanov, A, Weber, M, Eichmann, K-U, Bötel, S, Rahpoe, N, Bovensmann, H and **Burrows, JP.** 2014. Tropospheric column amount of ozone retrieved from SCIAMACHY limb–nadir-matching observations. *Atmos. Meas. Tech.* **7**: 2073–2096. DOI: https://doi.org/10.5194/amt-7-2073-2014

Eckhardt, S, Stohl, A, Beirle, S, Spichtinger, N, James, P, Forster, C, Junker, C, Wagner, T, Platt, U and **Jennings, SG.** 2003. The North Atlantic Oscillation controls air pollution transport to the Arctic. *Atmospheric Chemistry and Physics* **3**(5): 1769–1778. DOI: https://doi.org/10.5194/acp-3-1769-2003

EEA. 2016. *Air quality in Europe — 2016 report*, EEA Report No 28/2016, European Environment Agency (http://www.eea.europa.eu/publications/air-quality-in-europe-2016) accessed 6 June, 2017.

Eremenko, M, Dufour, G, Foret, G, Keim, C, Orphal, J, Beekmann, M, Bergametti, G and **Flaud, J-M.** 2008. Tropospheric ozone distributions over Europe during the heat wave in July 2007 observed from infrared nadir spectra recorded by IASI. *Geophys. Res. Lett.* **35**(L18): 805. DOI: https://doi.org/10.1029/2008GL034803

Fioletov, VE, Tarasick, DW and **Petropavlovskikh, I.** 2006. Estimating ozone variability and instrument uncertainties from SBUV(/2), ozonesonde, Umkehr, and SAGE II measurements: Short-term variations. *J. Geophys. Res.* **111**(D02): 305. DOI: https://doi.org/10.1029/2005JD006340

Fiore, AM, Naik, V and **Leibensperger, EM.** 2015. Air quality and climate connections. *Journal of the Air & Waste Management Association* **65**(6): 645–685. DOI: https://doi.org/10.1080/10962247.2015.1040526

Fiore, AM, West, JJ, Horowitz, LW, Naik, V and **Schwarzkopf, MD.** 2008. Characterizing the tropospheric ozone response to methane emission controls and the benefits to climate and air quality. *J. Geophys. Res.* **113**(D08): 307. DOI: https://doi.org/10.1029/2007JD009162

Fischer, EV, Jaffe, DA and **Weatherhead, EC.** 2011. Free tropospheric peroxyacetyl nitrate (PAN) and ozone at Mount Bachelor: Potential causes of variability and timescale for trend detection. *Atmospheric Chemistry and Physics* **11**: 5641–5654. DOI: https://doi.org/10.5194/acp-11-5641-2011

Fishman, J, Fakhruzzaman, K, Cros, B and **Nganda, D.** 1991. Identification of widespread pollution in the southern-hemisphere deduced from satellite analyses. *Science* **252**: 1693–1696. DOI: https://doi.org/10.1126/science.252.5013.1693

Fishman, J, Wozniak, AE and **Creilson, JK.** 2003. Global distribution of tropospheric ozone from satellite measurements using the empirically corrected tropospheric ozone residual technique: Identification of the regional aspects of air pollution. *Atmos. Chem. Phys.* **3**: 893–907. DOI: https://doi.org/10.5194/acp-3-893-2003

Fleming, ZL, Doherty, RM, von Schneidemesser, E, Malley, CS, Cooper, OR, Pinto, JP, et al. 2018. Tropospheric Ozone Assessment Report: Present-day ozone distribution and trends relevant to human health. *Elem Sci Anth.* **6**(1): 12. DOI: https://doi.org/10.1525/elementa.273

Foret, G, Hamaoui, L, Schmechtig, C, Eremenko, M, Keim, C, Dufour, G, Boynard, A, Coman, A, Ung, A and **Beekmann, M.** 2009. Evaluating the potential of IASI ozone observations to constrain simulated surface ozone concentrations. *Atmos. Chem. Phys.* **9**: 8479–8491. DOI: https://doi.org/10.5194/acp-9-8479-2009

Forster, P, et al. 2007. Changes in Atmospheric Constituents and in Radiative Forcing. In: *Climate Change 2007: The Physical Science Basis. Contribution of Working Group I to the Fourth Assessment Report of*

the Intergovernmental Panel on Climate Change, Solomon, S, Qin, D, Manning, M, Chen, Z, Marquis, M, Averyt, KB, Tignor, M and Miller, HL (eds.), 129–234. Cambridge University Press, Cambridge, United Kingdom and New York, NY, USA.

Forster, P and **Shine, K.** 1997. Radiative forcing and temperature trends from stratospheric ozone changes. *J. Geophys. Res. Atmos.* **102**: 10841–10855. DOI: https://doi.org/10.1029/96JD03510

Galani, E, Balis, D, Zanis, P, Zerefos, C, Papayannis, A, Wernli, H and **Gerasopoulos, E.** 2003. Observations of stratosphere-to-troposphere transport events over the eastern Mediterranean using a ground-based lidar system. *J. Geophys. Res.* **108**: 8527. DOI: https://doi.org/10.1029/2002JD002596

Galbally, IE, Schultz, MG, Buchmann, B, Gilge, S, Guenther, F, Koide, H, Oltmans, S, Patrick, L, Scheel, H-E, Smit, H, Steinbacher, M, Steinbrecht, W, Tarasova, O, Viallon, J, Volz-Thomas, A, Weber, M, Wielgosz, R and **Zellweger, C.** 2013. Guidelines for Continuous Measurement of Ozone in the Troposphere, GAW Report No 209. *Publication WMO-No.* **1110**. ISBN 978-92-63-11110-4, WMO, Geneva.

Garcia-Menendez, F, Monier, E and **Selin, NE.** 2017. The role of natural variability in projections of climate change impacts on U.S. ozone pollution. *Geophys. Res. Lett.* **44**: 2911–2921. DOI: https://doi.org/10.1002/2016GL071565

Gaudel, A, Ancellet, G and **Godin-Beekmann, S.** 2015. Analysis of 20 years of tropospheric ozone vertical profiles by lidar and ECC at Observatoire de Haute Provence (OHP) at 44 N, 6.7 E, *Atmos. Environ.* **113**: 78–89. DOI: https://doi.org/10.1016/j.atmosenv.2015.04.028

Gauss, M, et al. 2003. Radiative forcing in the 21st century due to ozone changes in the troposphere and the lower stratosphere. *J. Geophys. Res.* **108**(D9): 4292. DOI: https://doi.org/10.1029/2002JD002624

Gauss, et al. 2006. Radiative forcing since preindustrial times due to ozone change in the troposphere and the lower stratosphere. *Atmos. Chem. Phys.* **6**: 575–599. DOI: https://doi.org/10.5194/acp-6-575-2006

Granados-Muñoz, MJ and **Leblanc, T.** 2016. Tropospheric ozone seasonal and long-term variability as seen by lidar and surface measurements at the JPL-Table Mountain Facility, California. *Atmos. Chem. Phys.* **16**: 9299–9319. DOI: https://doi.org/10.5194/acp-16-9299-2016

Granier, C, Bessagnet, B, Bond, T, D'Angiola, A, van der Gon, HD, et al. 2011. Evolution of anthropogenic and biomass burning emissions of air pollutants at global and regional scales during the 1980–2010 period. *Climatic Change* **109**: 163–190. DOI: https://doi.org/10.1007/s10584-011-0154-1

Gratz, LE, Jaffe, DA and **Hee, JR.** 2014. Causes of increasing ozone and decreasing carbon monoxide in springtime at the Mt. Bachelor Observatory from 2004 to 2013. *Atmospheric Environment,* **109**: 323–330. DOI: https://doi.org/10.1016/j.atmosenv.2014.05.076

Harris, JM and **Kahl, JD.** 1990. A descriptive atmospheric transport climatology for the Mauna Loa Observatory using clustered trajectories. *J. Geophys. Res.* **95**: 13,651–13,667. DOI: https://doi.org/10.1029/JD095iD09p13651

Hering, WS. 1964. Ozonesonde Observations Over North America, Volume 1, AFCRL-64-30(I), Air Force Cambridge Research Labs, Hanscom AFB, Bedford, MA.

Hering, WS and **Borden, TS.** 1964. Ozonesonde Observations Over North America, Volume 2, AFCRL-64–30(II), Air Force Cambridge Research Labs, Hanscom AFB, Bedford, MA.

Hering, WS and **Borden, TS.** 1965. Ozonesonde Observations Over North America, Volume 3, AFCRL-64–30(III), Air Force Cambridge Research Labs, Hanscom AFB, Bedford, MA.

Hering, WS and **Borden, TS.** 1967. Ozonesonde Observations Over North America, Volume 4, AFCRL-64–30(IV), Air Force Cambridge Research Labs, Hanscom AFB, Bedford, MA.

Heue, K-P, et al. 2016. Trends of tropical tropospheric ozone from 20 years of European satellite measurements and perspectives for the Sentinel-5 Precursor. *Atmos. Meas. Tech.* **9**: 5037–5051. DOI: https://doi.org/10.5194/amt-9-5037-2016

Hilton, F, August, T, Barnet, C, Bouchard, A, Camy-Peyret, C, Clarisse, L, Clerbaux, C, Coheur, P-F, Collard, A, Crevoisier, C, Dufour, G, Edwards, D, Faijan, F, Fourrié, N, Gambacorta, A, Gauguin, S, Guidard, V, Hurtmans, D, Illingworth, S, Jacquinet-Husson, N, Kerzenmacher, T, Klaes, D, Lavanant, L, Masiello, G, Matricardi, M, McNally, T, Newman, S, Pavelin, E, Péquignot, E, Phulpin, T, Remedios, J, Schlüssel, P, Serio, C, Strow, L, Taylor, J, Tobin, D, Uspensky, A and **Zhou, D.** 2012. Hyperspectral Earth Observation from IASI: Five Years of Accomplishments. *Bulletin of the American Meteorological Society* **93**(3): 347–370. DOI: https://doi.org/10.1175/BAMS-D-11-00027.1

Hoesly, RM, Smith, SJ, Feng, L, Klimont, Z, Janssens-Maenhout, G, Pitkanen, T, Seibert, JJ, Vu, L, Andres, RJ, Bolt, RM, Bond, TC, Dawidowski, L, Kholod, N, Kurokawa, J-I, Li, M, Liu, L, Lu, Z, Moura, MCP, O'Rourke, PR and **Zhang, Q.** 2018. Historical (1750–2014) anthropogenic emissions of reactive gases and aerosols from the Community Emissions Data System (CEDS). *Geosci. Model Dev.* **11**: 369–408. DOI: https://doi.org/10.5194/gmd-11-369-2018

Huang, G, Liu, X, Chance, K, Yang, K, Bhartia, PK, Cai, Z, Allaart, M, Ancellet, G, Calpini, B, Coetzee, GJR, Cuevas-Agulló, E, Cupeiro, M, De Backer, H, Dubey, MK, Fuelberg, HE, Fujiwara, M, Godin-Beekmann, S, Hall, TJ, Johnson, B, Joseph, E, Kivi, R, Kois, B, Komala, N, König-Langlo, G, Laneve, G, Leblanc, T, Marchand, M, Minschwaner, KR, Morris, G, Newchurch, MJ, Ogino, SY, Ohkawara, N,

Piters, AJM, Posny, F, Querel, R, Scheele, R, Schmidlin, FJ, Schnell, RC, Schrems, O, Selkirk, H, Shiotani, M, Skrivánková, P, Stübi, R, Taha, G, Tarasick, DW, Thompson, AM, Thouret, V, Tully, MB, Van Malderen, R, Vömel, H, von der Gathen, P, Witte, JC and **Yela, M.** 2017. Validation of 10-year SAO OMI Ozone Profile (PROFOZ) product using ozonesonde observations. *Atmos. Meas. Tech.* **10**: 2455–2475. DOI: https://doi.org/10.5194/amt-10-2455-2017

Huang, M, Carmichael, GR, Chai, T, Pierce, RB, Oltmans, SJ, Jaffe, DA, Bowman, KW, Kaduwela, A, Cai, C, Spak, SN, Weinheimer, AJ, Huey, LG and **Diskin, GS.** 2013. Impacts of transported background pollutants on summertime western US air quality: model evaluation, sensitivity analysis and data assimilation. *Atmos. Chem. Phys.* **13**: 359–391. DOI: https://doi.org/10.5194/acp-13-359-2013

Hubert, D, Lambert, J-C, Verhoelst, T, et al. 2016. Ground-based assessment of the bias and long-term stability of 14 limb and occultation ozone profile data records. *Atmos. Meas. Tech.* **9**: 2497–2534. DOI: https://doi.org/10.5194/amt-9-2497-2016

Hurtmans, D, Coheur, P-F, Wespes, C, Clarisse, L, Scharf, O, Clerbaux, C, Hadji-Lazaro, J, George, M and **Turquety, S.** 2012. FORLI radiative transfer and retrieval code for IASI. *Journal of Quantitative Spectroscopy and Radiative Transfer* **113**: 1391–1408. DOI: https://doi.org/10.1016/j.jqsrt.2012.02.036

IPCC. 2013. Climate Change 2013: The Physical Science Basis. In: Stocker, TF, Qin, D, Plattner, G-K, Tignor, M, Allen, SK, Boschung, J, Nauels, A, Xia, Y, Bex, V and Midgley, PM (eds.), *Contribution of Working Group I to the Fifth Assessment Report of the Intergovernmental Panel on Climate Change*, 1535. Cambridge University Press, Cambridge, United Kingdom and New York, NY, USA.

Jacob, DJ, Heikes, EG, Fan, SM, Logan, JA, Mauzerall, DL, Bradshaw, JD, Singh, HB, Gregory, GL, Talbot, RW, Blake, DR and **Sachse, GW.** 1996. Origin of ozone and NO_x in the tropical troposphere: A photochemical analysis of aircraft observations over the South Atlantic basin. *Journal of Geophysical Research: Atmospheres* **101**(D19): 24235–24250. DOI: https://doi.org/10.1029/96JD00336

Jacob, DJ, Logan, JA and **Murti, PP.** 1999. Effect of rising Asian emissions on surface ozone in the United States. *Geophys. Res. Lett.* **26**: 2175–2178. DOI: https://doi.org/10.1029/1999GL900450

Jacob, DJ and **Winner, DA.** 2009. Effect of climate change on air quality. *Atmospheric Environment*, **43**(1): 51–63. DOI: https://doi.org/10.1016/j.atmosenv.2008.09.051

Jia, J, Ladstätter-Weißenmayer, A, Hou, X, Rozanov, A and **Burrows, JP.** 2017. Tropospheric ozone maxima observed over the Arabian Sea during the premonsoon. *Atmos. Chem. Phys.* **17**: 4915–4930. DOI: https://doi.org/10.5194/acp-17-4915-2017

Kalabokas, P, Hjorth, J, Foret, G, Dufour, G, Eremenko, M, Siour, G, Cuesta, J and **Beekmann, M.** 2017. An investigation on the origin of regional springtime ozone episodes in the western Mediterranean. *Atmos. Chem. Phys.* **17**: 3905–3928. DOI: https://doi.org/10.5194/acp-17-3905-2017

Kalabokas, PD, Cammas, J-P, Thouret, V, Volz-Thomas, A, Boulanger, D and **Repapis, CC.** 2013. Examination of the atmospheric conditions associated with high and low summer ozone levels in the lower troposphere over the eastern Mediterranean. *Atmos. Chem. Phys.* **13**: 10339–10352. DOI: https://doi.org/10.5194/acp-13-10339-2013

Kalabokas, PD, Mihalopoulos, N, Ellul, R, Kleanthous, S and **Repapis, CC.** 2008. An investigation of the meteorological and photochemical factors influencing the background rural and marine surface ozone levels in the Central and Eastern Mediterranean. *Atmos. Environ.* **42**: 7894–7906. DOI: https://doi.org/10.1016/j.atmosenv.2008.07.009

Kalabokas, PD and **Repapis, CC.** 2004. A climatological study of rural surface ozone in central Greece. *Atmos. Chem. Phys.* **4**: 1139–1147. DOI: https://doi.org/10.5194/acp-4-1139-2004

Kalabokas, PD, Thouret, V, Cammas, J-P, Volz-Thomas, A, Boulanger, D and **Repapis, CC.** 2015. The geographical distribution of meteorological parameters associated with high and low summer ozone levels in the lower troposphere and the boundary layer over the Eastern Mediterranean (Cairo case). *Tellus B*, **67**: 27853. DOI: https://doi.org/10.3402/tellusb.v67.27853

Kalabokas, PD, Volz-Thomas, A, Brioude, J, Thouret, V, Cammas, J-P and **Repapis, CC.** 2007. Vertical ozone measurements in the troposphere over the Eastern Mediterranean and comparison with Central Europe. *Atmos. Chem. Phys.* **7**: 3783–3790. DOI: https://doi.org/10.5194/acp-7-3783-2007

Kerr, J, Mcelroy, C and **Olafson, R.** 1981. Measurements of ozone with the Brewer ozone spectrophotometer. In: *Quadrennial International Ozone Symposium*, 74–79. Boulder, Colorado.

Kiehl, JT, Schneider, TL, Portmann, RW and **Solomon, S.** 1999. Climate forcing due to tropospheric and stratospheric ozone. *J. Geophys. Res.* **104**(D24): 31239–31254. DOI: https://doi.org/10.1029/1999JD900991

Kleanthous, S, Vrekoussis, M, Mihalopoulos, N, Kalabokas, P and **Lelieveld, J.** 2014. On the temporal and spatial variation of ozone in Cyprus. *Sc. of the Tot. Environ.* **476**: 677–687.

Komhyr, WD, Connor, BJ, McDermid, IS, McGee, TJ, Parrish, AD and **Margitan, JJ.** 1995. Comparison of STOIC 1989 ground-based lidar, microwave spectrometer, and Dobson spectrophotometer Umkehr ozone profiles with ozone profiles from balloon-borne electrochemical concentration cell ozonesondes. *J. Geophys. Res.* **100**(D5): 9273–9282. DOI: https://doi.org/10.1029/94JD02173

Komhyr, WD and **Sticksel, DR.** 1967a. Ozonesonde Observations 1962–1966 (Volume 1), ESSA Technical Report, IER 5I-IAS I, August 1967, Boulder, CO.

Komhyr, WD and **Sticksel, DR.** 1967b. Ozonesonde Observations 1962–1966 (Volume 2), ESSA Technical Report, ERL 80-APCL, 3, August 1968, Boulder, CO.

Krotkov, NA, McLinden, CA, Li, C, Lamsal, LN, Celarier, EA, Marchenko, SV, Swartz, WH, Bucsela, EJ, Joiner, J, Duncan, BN, Boersma, KF, Veefkind, JP, Levelt, PF, Fioletov, VE, Dickerson, RR, He, H, Lu, Z and **Streets, DG.** 2016. Aura OMI observations of regional SO_2 and NO_2 pollution changes from 2005 to 2015. *Atmos. Chem. Phys.* **16**: 4605–4629. DOI: https://doi.org/10.5194/acp-16-4605-2016

Kuai, L, Bowman, KW, Worden, HM, Herman, RL and **Kulawik, SS.** 2017. Hydrological controls on the tropospheric ozone greenhouse gas effect. *Elem Sci Anth.* **5**: 10. DOI: https://doi.org/10.1525/elementa.208

Lacis, AA, Wuebbles, DJ and **Logan, JA.** 1990. Radiative forcing of climate by changes in the vertical distribution of ozone. *J. Geophys. Res.* **95**: 9971–9981. DOI: https://doi.org/10.1029/JD095iD07p09971

Laj, P, Klausen, J, Bilde, M, Plass-Duelmer, C, Pappalardo, G, Clerbaux, C, Baltensperger, U, Hjorth, J, Simpson, D, Reimann, S and **Coheur, PF.** 2009. Measuring atmospheric composition change. *Atmospheric Environment* **43**(33): 5351–5414. DOI: https://doi.org/10.1016/j.atmosenv.2009.08.020

Lal, S, Venkataramani, S, Chandra, N, Cooper, OR, Brioude, J and **Naja, M.** 2014. Transport effects on the vertical distribution of tropospheric ozone over western India. *J. Geophys. Res. Atmos.* **119**. DOI: https://doi.org/10.1002/2014JD021854

Leblanc, T, McDermid, IS and **Walsh, TD.** 2012. Ground-based water vapor raman lidar measurements up to the upper troposphere and lower stratosphere for long-term monitoring. *Atmos. Meas. Tech.* **5**(1): 17–36. DOI: https://doi.org/10.5194/amt-5-17-2012

Leblanc, T, Sica, RJ, van Gijsel, JAE, Godin-Beekmann, S, Haefele, A, Trickl, T, Payen, G and **Gabarrot, F.** 2016a. Proposed standardized definitions for vertical resolution and uncertainty in the NDACC lidar ozone and temperature algorithms–Part 1: Vertical resolution. *Atmos. Meas. Tech.* **9**: 4029–4049. DOI: https://doi.org/10.5194/amt-9-4029-2016

Lefohn, AS, et al. 2018. Tropospheric Ozone Assessment Report: Global ozone metrics for climate change, human health, and crop/ecosystem Research. *Elem. Sci. Anth.*, **6**: 28. DOI: https://doi.org/10.1525/elementa.279

Lefohn, AS, Shadwick, D and **Oltmans, SJ.** 2010. Characterizing changes in surface ozone levels in metropolitan and rural areas in the United States for 1980–2008 and 1994–2008. *Atmos. Environ.* **44**: 5199–5210. DOI: https://doi.org/10.1016/j.atmosenv.2010.08.049

Leibensperger, EM, Mickley, LJ and **Jacob, DJ.** 2008. Sensitivity of US air quality to mid-latitude cyclone frequency and implications of 1980–2006 climate change. *Atmos. Chem. Phys.* **8**(23): 7075–86. DOI: https://doi.org/10.5194/acp-8-7075-2008

Lelieveld, J, Berresheim, H, Borrmann, S, Crutzen, PJ, Dentener, FJ, Fischer, H, Feichter, J, Flatau, PJ, Heland, J, Holzinger, R, Korrmann, R, Lawrence, MG, Levin, Z, Markowicz, KM, Mihalopoulos, N, Minikin, A, Ramanathan, V, de Reus, M, Roelofs, GJ, Scheeren, HA, Sciare, J, Schlager, H, Schultz, M, Siegmund, P, Steil, B, Stephanou, EG, Stier, P, Traub, M, Warneke, C, Williams, J and **Ziereis, H.** 2002. Global air pollution crossroads over the Mediterranean. *Science* **298**: 794–799. DOI: https://doi.org/10.1126/science.1075457

Levelt, PF, van den Oord, GHJ, Dobber, MR, Malkki, A, Visser, H, de Vries, J, Stammes, P, Lundell, JOV and **Saari, H.** 2006. The Ozone Monitoring Instrument. *IEEE Trans. Geosci. Remote Sens.* **44**: 1093–1101. DOI: https://doi.org/10.1109/TGRS.2006.872333

Leventidou, E, Eichmann, K-U, Weber, M and **Burrows, JP.** 2016. "Tropical tropospheric ozone columns from nadir retrievals of GOME-1/ERS-2, SCIAMACHY/Envisat, and GOME-2/MetOp-A (1996–2012)". *Atmospheric Measurement Techniques* **9**: 3407–3427. DOI: https://doi.org/10.5194/amt-9-3407-2016

Li, G, Bei, N, Cao, J, Wu, J, Long, X, Feng, T, Dai, W, Liu, S, Zhang, Q and **Tie, X.** 2017. Widespread and persistent ozone pollution in eastern China during the non-winter season of 2015: observations and source attributions. *Atmos. Chem. Phys.* **17**: 2759–2774. DOI: https://doi.org/10.5194/acp-17-2759-2017

Li, Q, et al. 2001. A tropospheric ozone maximum over the Middle East. *Geophysical Research Letters* **28**: 3235–3238. DOI: https://doi.org/10.1029/2001GL013134

Lin, M, et al. 2017. US surface ozone trends and extremes from 1980 to 2014: quantifying the roles of rising Asian emissions, domestic controls, wildfires, and climate. *Atmos. Chem. Phys.* **17**: 2943–2970. DOI: https://doi.org/10.5194/acp-17-2943-2017

Lin, M, Horowitz, LW, Cooper, OR, Tarasick, D, Conley, S, Iraci, LT, Johnson, B, Leblanc, T, Petropavlovskikh, I and **Yates, EL.** 2015. Revisiting the evidence of increasing springtime ozone mixing ratios in the free troposphere over western North America. *Geophys. Res. Lett.* **42**. DOI: https://doi.org/10.1002/2015GL065311

Lin, M, Horowitz, LW, Oltmans, SJ, Fiore, AM and **Fan, S.** 2014. Tropospheric ozone trends at Mauna Loa Observatory tied to decadal climate variability. *Nature Geoscience* **7**: 136–143. DOI: https://doi.org/10.1038/ngeo2066

Liu, C, Liu, X and **Chance, K.** 2013. The impact of using different ozone cross sections on ozone profile retrievals from OMI UV measurements. *J. Quant. Spectrosc. Radiat. Transfer* **130**: 365–372. DOI: https://doi.org/10.1016/j.jqsrt.2013.06.006

Liu, F, et al. 2016. Recent reduction in NO_x emissions over China: synthesis of satellite observations and emission inventories. *Environ. Res. Lett.*, 11,114002. DOI: https://doi.org/10.1088/1748-9326/11/11/114002

Liu, G, Liu, J, Tarasick, DW, Fioletov, VE, Jin, JJ, Moeini, O, Liu, X, Sioris, CE and **Osman, M.** 2013. A global tropospheric ozone climatology from trajectory-mapped ozone soundings. *Atmospheric Chemistry and Physics* **13**: 10659–10675. DOI: https://doi.org/10.5194/acp-1310659-2013

Liu, J, et al. 2017. Causes of interannual variability over the southern hemispheric tropospheric ozone maximum. *Atmos. Chem. Phys.* **17**: 3279–3299. DOI: https://doi.org/10.5194/acp-17-3279-2017

Liu, J, Rodriguez, JM, Thompson, AM, Logan, JA, Douglass, AR, Olsen, MA, Steenrod, SD and **Posny, F.** 2016. Origins of tropospheric ozone interannual variation over Réunion: A model investigation. *J. Geophys. Res. Atmos.* **121**: 521–537. DOI: https://doi.org/10.1002/2015JD023981

Liu, J, Tarasick, DW, Fioletov, VE, McLinden, C, Zhao, T, Gong, S, Sioris, C, Jin, JJ, Liu, G and **Moeini, O.** 2013. A global ozone climatology from ozone soundings via trajectory mapping: A stratospheric perspective. *Atmospheric Chemistry and Physics* **13**: 11441–11464. DOI: https://doi.org/10.5194/acp-13-11441-2013

Liu, JJ, Jones, DBA, Worden, JR, Noone, D, Parrington, M and **Kar, J.** 2009. Analysis of the summertime build-up of tropospheric ozone abundances over the Middle East and North Africa as observed by the Tropospheric Emission Spectrometer instrument. *J. Geophys. Res.* **114**(D05): 304. DOI: https://doi.org/10.1029/2008JD010993

Liu, X, Bhartia, PK, Chance, K, Spurr, RJD and **Kurosu, TP.** 2010. Ozone profile retrievals from the Ozone Monitoring Instrument. *Atmos. Chem. Phys.* **10**: 2521–2537. DOI: https://doi.org/10.5194/acp-10-2521-2010

Liu, X, Chance, K and **Kurosu, TP.** 2007. Improved ozone profile retrievals from GOME data with degradation correction in reflectance. *Atmos. Chem. Phys.* **7**: 1575–1583. DOI: https://doi.org/10.5194/acp-7-1575-2007

Liu, X, Chance, K, Sioris, CE and **Kurosu, TP.** 2007. Impact of using different ozone cross sections on ozone profile retrievals from Global Ozone Monitoring Experiment (GOME) ultraviolet measurements. *Atmos. Chem. Phys.* **7**: 3571–3578. DOI: https://doi.org/10.5194/acp-7-3571-2007

Liu, X, Chance, K, Sioris, CE, Spurr, RJD, Kurosu, TP, Martin, RV and **Newchurch, MJ.** 2005. Ozone profile and tropospheric ozone retrievals from the Global Ozone Monitoring Experiment: Algorithm description and validation. *J. Geophys. Res.* **110**(D20). DOI: https://doi.org/10.1029/2005JD006240

Livesey, NJ, Read, WG, Froidevaux, L, Lambert, A, Manney, GL, Pumphrey, HC, Santee, ML, Schwartz, MJ, Wang, S, Cofield, RE, Cuddy, DT, Fuller, RA, Jarnot, RF, Jiang, JH, Knosp, BW, Stek, PC, Wagner, PA and **Wu, DL.** 2011. EOS MLS Version 3.3 Level 2 data quality and description document, Tech. rep., Jet Propulsion Laboratory. Available from: http://mls.jpl.nasa.gov.

Logan, JA. 1985. Tropospheric ozone: Seasonal behavior, trends, and anthropogenic influence. *J. Geophys. Res.* **90**(D6): 10463–10482. DOI: https://doi.org/10.1029/JD090iD06p10463

Logan, JA, et al. 2012. Changes in ozone over Europe: Analysis of ozone measurements from sondes, regular aircraft (MOZAIC) and alpine surface sites. *J. Geophys. Res.* **117**(D09): 301. DOI: https://doi.org/10.1029/2011JD016952

Logan, JA and **Kirchhoff, VWJH.** 1986. Seasonal variations of tropospheric ozone at Natal, Brazil. *J. Geophys. Res.* **91**(D7): 7875–7881. DOI: https://doi.org/10.1029/JD091iD07p07875

Lombardozzi, D, Levis, S, Bonan, G, Hess, PG and **Sparks, JP.** 2015. The influence of chronic ozone exposure on global carbon and water cycles. *J. Clim* **28**: 292–305. DOI: https://doi.org/10.1175/JCLI-D-14-00223.1

LRTAP Convention. 2015. Draft Chapter III: Mapping Critical levels for Vegetation, of the Manual on Methodologies and Criteria for Modelling and Mapping Critical Loads and Levels and Air Pollution Effects, Risks and Trends. Available at: http://icpmapping.org/Mapping_Manual.

Ma, Z, et al. 2016. Significant increase of surface ozone at a rural site, north of eastern China. *Atmos. Chem. Phys.* **16**: 3969–3977. DOI: https://doi.org/10.5194/acp-16-3969-2016

Marenco, A, et al. 1998. Measurement of ozone and water vapor by Airbus in-service aircraft: The MOZAIC airborne program, an overview. *J. Geophys. Res.* **103**(D19): 25631–25642. DOI: https://doi.org/10.1029/98JD00977

Mateer, CL. 1964. A study of the information content of Umkehr Observations. Ph. D. thesis, University of Michigan.

Mateer, CL and **DeLuisi, JJ.** 1992. A new Umkehr inversion algorithm. *J. Atmos. Ter. Phys.* **54**: 537–556. DOI: https://doi.org/10.1016/0021-9169(92)90095-3

Matricardi, M, Chevallier, F, Kelly, G and **Thepaut, JN.** 2004. An improved general fast radiative transfer model for the assimilation of radiance observations. *Quarterly Journal of the Royal Meteorological Society*, **130**: 153–173. DOI: https://doi.org/10.1256/qj.02.181

McDermid, S, Beyerle, G, Haner, D and **Leblanc, T.** 2002. Redesign and improved performance of the tropospheric ozone lidar at the Jet Propulsion Laboratory Table Mountain Facility. *Appl. Opt.* **41**(36): 7550–7555. DOI: https://doi.org/10.1364/AO.41.007550

McLinden, CA, Olsen, SC, Hannegan, B, Wild, O, Prather, MJ and **Sundet, J.** 2000. Stratospheric ozone in 3-D models: A simple chemistry and the cross-tropopause flux. *J. Geophys. Res.* **105**(D11): 14653–14665. DOI: https://doi.org/10.1029/2000JD900124

McPeters, RD, Labow, GJ and **Logan, JA.** 2007. Ozone climatological profiles for satellite retrieval algorithms. *J. Geophys. Res.* **112**(D05): 308. DOI: https://doi.org/10.1029/2005JD006823

Mickley, LJ, Jacob, DJ, Field, BD and **Rind, D.** 2004. Effects of future climate change on regional air pollution episodes in the United States. *Geophys. Res. Lett.* **30**(L2): 4103. DOI: https://doi.org/10.1029/2004GL021216

Mickley, LJ, Jacob, DJ and **Rind, D.** 2001. Uncertainty in preindustrial abundance of tropospheric ozone: implications for radiative forcing calculations. *J. Geophys. Res.* **106**(D4): 3389–3399. DOI: https://doi.org/10.1029/2000JD900594

Miles, GM, Siddans, R, Kerridge, BJ, Latter, BG and **Richards, NAD.** 2015. Tropospheric ozone and ozone profiles retrieved from GOME-2 and their validation. *Atmospheric Measurement Techniques* **8**(1). DOI: https://doi.org/10.5194/amt-8-385-2015

Mills, G, et al. 2018. Tropospheric Ozone Assessment Report: Present-day ozone distribution and trends relevant to vegetation. *Elem. Sci. Anth.*, in-review.

Miyazaki, K, et al. 2017. Decadal changes in global surface NO_x emissions from multi-constituent satellite data assimilation. *Atmos. Chem. Phys.* **17**: 807–837. DOI: https://doi.org/10.5194/acp-17-807-2017

Monks, PS, Archibald, AT, Colette, A, Cooper, O, Coyle, M, Derwent, R, Fowler, D, Granier, C, Law, KS, Mills, GE, Stevenson, DS, Tarasova, O, Thouret, V, von Schneidemesser, E, Sommariva, R, Wild, O and **Williams, ML.** 2015. Tropospheric ozone and its precursors from the urban to the global scale from air quality to short-lived climate forcer. *Atmos. Chem. Phys.* **15**: 8889–8973. DOI: https://doi.org/10.5194/acp-15-8889-2015

Moxim, WJ and **Levy, H, II.** 2000. A model analysis of the tropical South Atlantic Ocean tropospheric ozone maximum: The interaction of transport and chemistry. *J. Geophys. Res.* **105**(D13): 17393–17415. DOI: https://doi.org/10.1029/2000JD900175

Munro, R, Siddans, R, Reburn, WJ and **Kerridge, BJ.** 1998. Direct measurement of tropospheric ozone distributions from space. *Nature* **392**: 168–171. DOI: https://doi.org/10.1038/32392

Myhre, G, Shindell, D, Bréon, F-M, Collins, W, Fuglestvedt, J, Huang, J, Koch, D, Lamarque, J-F, Lee, D, Mendoza, B, Nakajima, T, Robock, A, Stephens, G, Takemura, T and **Zhang, H.** 2013. Anthropogenic and Natural Radiative Forcing. In: *Climate Change 2013: The Physical Science Basis. Contribution of Working Group I to the Fifth Assessment Report of the Intergovernmental Panel on Climate Change*, Stocker, TF, Qin, D, Plattner, G-K, Tignor, M, Allen, SK, Boschung, J, Nauels, A, Xia, Y, Bex, V and Midgley, PM (eds.). Cambridge University Press, Cambridge, United Kingdom and New York, NY, USA.

Naik, V, et al. 2005. Net radiative forcing due to changes in regional emissions of tropospheric ozone precursors. *J. Geophys. Res.* **110**(D2): 4306. DOI: https://doi.org/10.1029/2005JD005908

Nair, PJ, Godin-Beekmann, S, Pazmiño, A, Hauchecorne, A, Ancellet, G, Petropavlovskikh, I, Flynn, LE and **Froidevaux, L.** 2011. Coherence of long-term stratospheric ozone vertical distribution time series used for the study of ozone recovery at a northern mid-latitude station. *Atmos. Chem. Phys.* **11**: 4957–4975. DOI: https://doi.org/10.5194/acp-11-4957-2011

National Research Council. 1992. Rethinking the ozone problem in urban and regional air pollution. National Academies Press.

Nédélec, P, Blot, R, Boulanger, D, Athier, G, Cousin, J, Gautron, B, Petzold, A, Volz-Thomas, A and **Thouret, V.** 2015. Instrumentation on commercial aircraft for monitoring the atmospheric composition on a global scale: the IAGOS system, technical overview of ozone and carbon monoxide measurements. *Tellus B* **67**. DOI: https://doi.org/10.3402/tellusb.v67.27791

Neu, J, et al. 2014. Tropospheric ozone variations governed by changes in stratospheric circulation. *Nature Geoscience* **7**: 340–344. DOI: https://doi.org/10.1038/ngeo2138

Oetjen, H, Payne, VH, Kulawik, SS, Eldering, A, Worden, J, Edwards, DP, Francis, GL, Worden, HM, Clerbaux, C, Hadji-Lazaro, J and **Hurtmans, D.** 2014. Extending the satellite data record of tropospheric ozone profiles from Aura-TES to MetOp-IASI: characterisation of optimal estimation retrievals. *Atmos. Meas. Tech.* **7**: 4223–4236. DOI: https://doi.org/10.5194/amt-7-4223-2014

Oetjen, H, Payne, VH, Neu, JL, Kulawik, SS, Edwards, DP, Eldering, A, Worden, HM and **Worden, JR.** 2016. A joint data record of tropospheric ozone from Aura-TES and MetOp-IASI. *Atmos. Chem. Phys.* **16**: 10229–10239. DOI: https://doi.org/10.5194/acp-16-10229-2016

Oltmans, SJ, Karion, A, Schnell, RC, Pétron, G, Helmig, D, Montzka, SA, et al. 2016. O_3, CH_4, CO_2, CO, NO_2 and NMHC aircraft measurements in the Uinta Basin oil and gas region under low and high ozone conditions in winter 2012 and 2013. *Elementa* **4**: 132. DOI: https://doi.org/10.12952/journal.elementa.000132

Oltmans, SJ, Lefohn, AS, Harris, JM, Galbally, I, Scheel, HE, Bodeker, G, Brunke, E, Claude, H, Tarasick, D, Johnson, BJ, Simmonds, P, Shadwick, D, Anlauf, K, Hayden, K, Schmidlin, F, Fujimoto, T, Akagi, K, Meyer, C, Nichol, S, Davies, J, Redondas, A and **Cuevas, E.** 2006. Long-term Changes in Tropospheric Ozone. *Atmos. Environ.* **40**: 3156–3173. DOI: https://doi.org/10.1016/j.atmosenv.2006.01.029

Oltmans, SJ, Lefohn, AS, Shadwick, D, Harris, JM, Scheel, H-E, Galbally, I, Tarasick, DW, Johnson, BJ Brunke, EG, Claude, H, Zeng, G, Nichol, S, Schmidlin, FJ, Davies, J, Cuevas, E, Redondas, A, Naoe, H, Nakano, T and **Kawasato, T.** 2013. Recent Tropospheric Ozone Changes–A Pattern Dominated by Slow or No Growth. *Atmospheric Environment* **67**: 331–351. DOI: https://doi.org/10.1016/j.atmosenv.2012.10.057

Parrish, DD, Lamarque, J-F, Naik, V, Horowitz, L, Shindell, DT, et al. 2014. Long-term changes in

lower tropospheric baseline ozone concentrations: Comparing chemistry-climate models and observations at northern mid-latitudes. *J. Geophys. Res.* **119**(9): 5719–5736. DOI: https://doi.org/10.1002/2013JD021435

Parrish, DD, Law, KS, Staehelin, J, Derwent, R, Cooper, OR, et al. 2012. Long-term changes in lower tropospheric baseline ozone concentrations at northern mid-latitudes. *Atmos. Chem. Phys.* **12**: 11485–11504. DOI: https://doi.org/10.5194/acp-12-11485-2012

Parrish, DD, Law, KS, Staehelin, J, Derwent, R, Cooper, OR, et al. 2013. Lower tropospheric ozone at northern mid-latitudes: Changing seasonal cycle. *Geophys. Res. Lett* **40**: 1631–1636. DOI: https://doi.org/10.1002/grl.50303

Pavelin, EG, English, SJ and **Eyre, JR.** 2008. The assimilation of cloud-affected infrared satellite radiances for numerical weather prediction, *Q. J. R. Meteorol. Soc.* **134**: 737–749. DOI: https://doi.org/10.1002/qj.243

Payne, VH, Neu, JL and **Worden, HM.** 2017. Satellite observations for understanding the drivers of variability and trends in tropospheric ozone. *J. Geophys. Res.*

Petetin, H, Thouret, V, Athier, G, Blot, R, Boulanger, D, Cousin, J-M, Gaudel, A, Nédélec, P and **Cooper, O.** 2016a. Diurnal cycle of ozone throughout the troposphere over Frankfurt as measured by MOZAIC-IAGOS commercial aircraft. *Elementa: Science of the Anthropocene* **4**. DOI: https://doi.org/10.12952/journal.elementa.000129

Petetin, H, Thouret, V, Fontaine, A, Sauvage, B, Athier, G, Blot, R, Boulanger, D, Cousin, J-M and **Nédélec, P.** 2016b. Characterizing tropospheric ozone and CO around Frankfurt between 1994–2012 based on MOZAIC-IAGOS aircraft measurements. *Atmos. Chem. Phys.* **16**: 15147–15163. DOI: https://doi.org/10.5194/acp-16-15147-2016

Petropavlovskikh, I, Bhartia, PK and **DeLuisi, J.** 2005. New Umkehr ozone profile retrieval algorithm optimized for climatological studies. *Geophys. Res. Lett.* **32**(L1): 6808. DOI: https://doi.org/10.1029/2005GL023323

Petropavlovskikh, I, Evans, R, McConville, G, Oltmans, S, Quincy, D, Lantz, K, Disterhoft, P, Stanek, M and **Flynn, L.** 2011. Sensitivity of Dobson and Brewer Umkehr ozone profile retrievals to ozone cross-sections and stray light effects. *Atmospheric Measurement Techniques* **4**: 1841–1853. DOI: https://doi.org/10.5194/amt-4-1841-2011

Petzold, A, Thouret, V, Gerbig, C, Zahn, A, Brenninkmeijer, C, Gallagher, M, Hermann, M, Pontaud, M, Ziereis, H, Boulanger, D, Marshall, J, Nédélec, P, Smit, H, Friess, U, Flaud, J, Wahner, A, Cammas, J and **Volz-Thomas, A.** 2015. Global-scale atmosphere monitoring by in-service aircraft–current achievements and future prospects of the European Research Infrastructure IAGOS. *Tellus B* **67**. DOI: https://doi.org/10.3402/tellusb.v%v.28452

Portmann, RW, Solomon, S, Fishman, J, Olson, JR, Kiehl, JT and **Briegleb, B.** 1997. Radiative forcing of the Earth's climate system due to tropical tropospheric ozone production. *Journal of Geophysical Research: Atmospheres* **102**(D8): 9409–9417. DOI: https://doi.org/10.1029/96JD04007

Price, S and **Pales, JC.** 1963. Mauna Loa Observatory: The first five years, Monthly Weather Review, October-December. DOI: https://doi.org/10.1175/1520-0493(1963)091%3C0665:MLOTFF%3E2.3.CO;2

REVIHAAP. 2013. Review of evidence on health aspects of air pollution–REVIHAAP Project technical report. World Health Organization (WHO) Regional Office for Europe. Bonn. Available at: http://www.euro.who.int/data/assets/pdf_file/0004/193108/REVIHAAP-Final-technical-report-final-version.pdf.

Richards, NAD, Arnold, SR, Chipperfield, MP, Miles, G, Rap, A, Siddans, R, Monks, SA and **Hollaway, MJ.** 2013. The Mediterranean summertime ozone maximum: global emission sensitivities and radiative impacts. *Atmos. Chem. Phys.* **13**: 2331–2345. DOI: https://doi.org/10.5194/acp-13-2331-2013

Rodgers, CD. 2000. Inverse methods for atmospheric sounding: Theory and Practice, Series on Atmospheric, Oceanic and Planetary Physics–Vol. 2. *World Scientific*. DOI: https://doi.org/10.1142/3171

Rodriguez-Franco, JJ and **Cuevas, E.** 2013. Characteristics of the subtropical tropopause region based on long-term highly-resolved sonde records over Tenerife. *J. Geophys. Res. Atmos.* **118**. DOI: https://doi.org/10.1002/jgrd.50839

Roelofs, GJ, Scheeren, HA, Heland, J, Ziereis, H and **Lelieveld, J.** 2003. A model study of ozone in the eastern Mediterranean free troposphere during MINOS (August 2001). *Atmos. Chem. Phys.* **3**: 1199–1210. DOI: https://doi.org/10.5194/acp-3-1199-2003

Rozanov, VV, Diebel, D, Spurr, RJD and **Burrows, JP.** 1997. GOMETRAN: A radiative transfer model for the satellite project GOME–the plane-parallel version. *J. Geophys. Res.* **102**: 16683–16695. DOI: https://doi.org/10.1029/96JD01535

Safieddine, S, et al. 2016. Tropospheric ozone variability during the East Asian summer monsoon as observed by satellite (IASI), aircraft (MOZAIC) and ground stations. *Atmos. Chem. Phys.* **16**: 10489–10500. DOI: https://doi.org/10.5194/acp-16-10489-2016

Safieddine, S, Boynard, A, Coheur, P-F, Hurtmans, D, Pfister, G, Quennehen, B, Thomas, JL, Raut, J-C, Law, KS, Klimont, Z, Hadji-Lazaro, J, George, M and **Clerbaux, C.** 2014. Summertime tropospheric ozone assessment over the Mediterranean region using the thermal infrared IASI/MetOp sounder and the WRF-Chem model. *Atmos. Chem. Phys.* **14**: 10119–10131. DOI: https://doi.org/10.5194/acp-14-10119-2014

Sánchez, ML, García, MA, Pérez, IA and **de Torre, B.** 2008. Evaluation of surface ozone measurements during 2000–2005 at a rural area in the upper

Spanish plateau. *J. Atmos. Chem.* **60**: 137–152. DOI: https://doi.org/10.1007/s10874-008-9113-2

Saunders, R, Matricardi, M and **Brunel, P.** 1999. An improved fast radiative transfer model for assimilation of satellite radiance observations. *QJRMS* **125**: 1407–1425.

Sauvage, B, et al. 2005. Tropospheric ozone over Equatorial Africa: regional aspects from the MOZAIC data. *Atmos. Chem. Phys.* **5**: 311–335. DOI: https://doi.org/10.5194/acp-5-311-2005

Sauvage, B, Martin, RV, van Donkelaar, A and **Ziemke, JR.** 2007. Quantification of the factors controlling tropical tropospheric ozone and the South Atlantic maximum. *J. Geophys. Res.* **112**(D1): 1309. DOI: https://doi.org/10.1029/2006JD008008

Scheeren, HA, Lelieveld, J, Roelofs, GJ, Williams, J, Fischer, H, de Reus, M, de Gouw, JA, Warneke, C, Holzinger, R, Schlager, H, Klüpfel, T, Bolder, M, van der Veen, C and **Lawrence, M.** 2003. The impact of monsoon outflow from India and Southeast Asia in the upper troposphere over the eastern Mediterranean. *Atmos. Chem. Phys.* **3**: 1589–1608. DOI: https://doi.org/10.5194/acp-3-1589-2003

Schenkeveld, VME, Jaross, G, Marchenko, S, Haffner, D, Kleipool, QL, Rozemeijer, NC, Veefkind, JP and **Levelt, PF.** 2016. In-flight performance of the Ozone Monitoring Instrument. *AMT*, in-review.

Schnadt Poberaj, C, Staehelin, J, Brunner, D, Thouret, V, De Backer, H, et al. 2009. Long-term changes in UT/LS ozone between the late 1970s and the 1990s deduced from the GASP and MOZAIC aircraft programs and from ozonesondes. *Atmos. Chem. Phys.* **9**: 5343–5369. DOI: https://doi.org/10.5194/acp-9-5343-2009

Schneider, M, Blumenstock, T, Hase, F, Höpfner, M, Cuevas, E, Redondas, A and **Sancho, JM.** 2005. Ozone profiles and total column amounts derived at Izaña Tenerife Island, from FTIR solar absorption spectra, and its validation by an intercomparison to ECC-sonde and Brewer spectrometer measurements. *Journal of Quantitative Spectroscopy & Radiative Transfer* **91**: 245–274. DOI: https://doi.org/10.1016/j.jqsrt.2004.05.067

Schultz, MG, Schröder, S, Lyapina, O, Cooper, O, Galbally, I, Petropavlovskikh, I, et al. 2017. Tropospheric Ozone Assessment Report: Database and Metrics Data of Global Surface Ozone Observations. *Elem Sci Anth.* **5**: 58. DOI: https://doi.org/10.1525/elementa.244

Schürmann, GJ, Algieri, A, Hedgecock, IM, Manna, G, Pirrone, N and **Sprovieri, F.** 2009. Modeling local and synoptic scale influences on ozone concentrations in a topographically complex region of Southern Italy. *Atmos. Environ.* **43**: 4424–4434. DOI: https://doi.org/10.1016/j.atmosenv.2009.06.017

Schwab, JJ, Wolfe, D, Casson, P, et al. 2016. Atmospheric Science Research at Whiteface Mountain, NY: Site Description and History. *Aerosol and Air Quality Research* **16**: 827–840. DOI: https://doi.org/10.4209/aaqr.2015.05.0343

Shen, L and **Mickley, LJ.** 2017. Effects of El Niño on summertime ozone air quality in the eastern United States. *Geophysical Research Letters* **44**: 12,543–12,550.DOI:https://doi.org/10.1002/2017GL076150

Shen, L, Mickley, LJ and **Gilleland, E.** 2016. Impact of increasing heat waves on U.S. ozone episodes in the 2050s: Results from a multimodel analysis using extreme value theory. *Geophys. Res. Lett.* **43**: 4017–4025.DOI:https://doi.org/10.1002/2016GL068432

Shindell, D and **Faluvegi, G.** 2009. Climate response to regional radiative forcing during the twentieth century. *Nature Geoscience* **2**: 294. DOI: https://doi.org/10.1038/ngeo473

Simon, H, et al. 2015. Ozone Trends Across the United States over a Period of Decreasing NO_x and VOC Emissions. *Environ. Sci. Technol.* **49**: 186–195. DOI: https://doi.org/10.1021/es504514z

Simpson, D, Arneth, A, Mills, G, Solberg, S and **Uddling, J.** 2014. Ozone — the persistent menace: interactions with the N cycle and climate change. *Current Opinion in Environmental Sustainability* **9–10**: 9–19. DOI: https://doi.org/10.1016/j.cosust.2014.07.008

Sitch, S, Cox, PM, Collins, WJ and **Huntingford, C.** 2007. Indirect radiative forcing of climate change through ozone effects on the land-carbon sink. *Nature* **448**: 791–794. DOI: https://doi.org/10.1038/nature06059

Škerlak, B, Sprenger, M and **Wernli, H.** 2014. A global climatology of stratosphere–troposphere exchange using the ERA-Interim data set from 1979 to 2011. *Atmos. Chem. Phys.* **14**: 913–937. DOI: https://doi.org/10.5194/acp-14-913-2014

Sofen, ED, Bowdalo, D and **Evans, MJ.** 2016. How to most effectively expand the global surface ozone observing network. *Atmospheric Chemistry and Physics*, **16**(3): 1445–1457. DOI: https://doi.org/10.5194/acp-16-1445-2016

Steinbrecht, W, et al. 2017. An update on ozone profile trends for the period 2000 to 2016. *Atmos. Chem. Phys.* **17**: 10675–10690. DOI: https://doi.org/10.5194/acp-17-10675-2017

Stevenson, D, et al. 2013. Tropospheric ozone changes, radiative forcing and attribution to emissions in the Atmospheric Chemistry and Climate Model Intercomparison Project (ACCMIP). *Atmos. Chem. Phys.* **13**: 3063–3085. DOI: https://doi.org/10.5194/acp-13-3063-2013

Stevenson, DS, Dentener, FJ, Schultz, MG, Ellingsen, K, Van Noije, TPC, Wild, O, Zeng, G, Amann, M, Atherton, CS, Bell, N, Bergmann, DJ, Bey, I, Butler, T, Cofala, J, Collins, WJ, Derwent, RG, Doherty, RM, Drevet, J, Eskes, HJ, Fiore, AM, Gauss, M, Hauglustaine, DA, Horowitz, LW, Isaksen, ISA, Krol, MC, Lamarque, J-F, Lawrence, MG, Montanaro, V, Müller, J-F, Pitari, G, Prather, MJ, Pyle, JA, Rast, S, Rodgriguez, JM, Sanderson, MG, Savage, NH, Shindell, DT, Strahan, SE, Sudo, K and **Szopa, S.** 2006. Multimodel ensemble simulations of present-day and near-future tropospheric

ozone. *J. Geophys. Res.* **111**(D8). DOI: https://doi.org/10.1029/2005JD006338

Stohl, A, et al. 2003. Stratosphere-troposphere exchange: A review, and what we have learned from STACCATO. *J. Geophys. Res.* **108**(D12): 8516. DOI: https://doi.org/10.1029/2002JD002490

Strode, SA, Douglass, AR, Ziemke, JR, Manyin, M, Nielsen, JE and **Oman, LD.** 2017. A model and satellite-based analysis of the tropospheric ozone distribution in clear versus convectively cloudy conditions. *Journal of Geophysical Research: Atmospheres* **122**: 11,948–11,960. DOI: https://doi.org/10.1002/2017JD027015

Sun, L, Xue, L, et al. 2016. Significant increase of summertime ozone at Mount Tai in Central Eastern China. *Atmos. Chem. Phys.* **16**: 10637–10650. DOI: https://doi.org/10.5194/acp-16-10637-2016

Swap, RJ, Annegarn, HJ, Suttles, JT, King, MD, Platnick, S, Privette, JL and **Scholes, RJ.** 2003. Africa burning: A thematic analysis of the Southern African Regional Science Initiative (SAFARI 2000). *J. Geophys. Res.* **108**: 8465. DOI: https://doi.org/10.1029/2003JD003747

Tanimoto, H, et al. 2015. Consistency of tropospheric ozone observations made by different platforms and techniques In: The global databases. *Tellus, B,* **67**: 27073. DOI: https://doi.org/10.3402/tellusb.v67.27073

Tarasick, DW, et al. 2010. High-resolution tropospheric ozone fields for INTEX and ARCTAS from IONS ozonesondes. *J. Geophys. Res.* **115**(D20): 301. DOI: https://doi.org/10.1029/2009JD012918

Tarasick, DW, Davies, J, Smit, HGJ and **Oltmans, SJ.** 2016. A re-evaluated Canadian ozonesonde record: measurements of the vertical distribution of ozone over Canada from 1966 to 2013. *Atmos. Meas. Tech.* **9**: 195–214. DOI: https://doi.org/10.5194/amt-9-195-2016

Tarasick, D, Galbally, I, Cooper, OR, Ancellet, G, Leblanc, T, Wallington, TJ, Ziemke, J, Liu, X, Steinbacher, M, Stähelin, J, Vigouroux, C, Hannigan, J, García, O, Foret, G, Zanis, P, Weatherhead, E, Petropavlovskikh, I, Worden, H, Osman, M, Liu, J, Lin, M, Schultz, M, Granados-Muñoz, M, Thompson, AM, Oltmans, SJ, Cuesta, J, Dufour, G, Thouret, V, Hassler, B and **Trickl, T.** 2018. Tropospheric Ozone Assessment Report: Tropospheric ozone observations–How well do we know tropospheric ozone changes? *Elem. Sci. Anth.* in-review.

Team, NS. 2000. An Assessment of Tropospheric Ozone Pollution-a North American Perspective. NARSTO. http://www.narsto.org/ozone_assessment.

The Royal Society. 2008. *Ground-level Ozone in the 21st century: Future Trends, Impacts and Policy Implications.* Royal Society policy document 15/08, RS1276, (http://royalsociety.org/Report_WF.aspx?pageid57924&terms5ground-level1ozone).

Thompson, AM, et al. 2000. A tropical Atlantic Paradox: Shipboard and satellite views of a tropospheric ozone maximum and wave-one in January–February 1999. *J. Geophys. Res.* DOI: https://doi.org/10.1029/1999GL011273

Thompson, AM, Balashov, NV, Witte, JC, Coetzee, GJR, Thouret, V and **Posny, F.** 2014. Tropospheric ozone increases in the southern African region: Bellwether for rapid growth in southern hemisphere pollution? *Atmos. Chem. Phys.* **14**: 9855–9869. DOI: https://doi.org/10.5194/acp-14-9855-2014

Thompson, AM, Miller, SK, Tilmes, S, Kollonige, DW, Witte, JC, Oltmans, SJ, Johnson, BJ, Fujiwara, M, Schmidlin, FJ, Coetzee, GJR, Komala, N, Maata, M, bt Mohamad, M, Nguyo, J, Mutai, C, Ogino, S-Y, Raimundo, F, Da Silva, NM, Paes Leme, F, Posny, R, Scheele, HB, Selkirk, M, Shiotani, R, Stübi, G, Levrat, B, Calpini, V, Thouret, H, Tsuruta, J, Valverde Canossa, H, Vömel, S, Yonemura, J, Andrés Diaz, N, Tan Thanh, T and **Thuy Ha, HT.** 2012. Southern Hemisphere Additional Ozonesondes (SHADOZ) ozone climatology (2005–2009): Tropospheric and tropical tropopause layer (TTL) profiles with comparisons to OMI based ozone products. *J. Geophys. Res.* **117**(D2): 3301. DOI: https://doi.org/10.1029/2010JD016911

Thompson, AM, Witte, JC, Smit, HGJ, Oltmans, SJ, Johnson, BJ, Kirchhoff, VWJH and **Schmidlin, FJ.** 2007. Southern Hemisphere Additional Ozonesondes (SHADOZ) 1998–2004 tropical ozone climatology: 3. Instrumentation, station-to-station variability, and evaluation with simulated flight profiles. *J. Geophys. Res.* **112**(D03): 304. DOI: https://doi.org/10.1029/2005JD007042

Thompson, AM, Witte, JC, Sterling, C, Jordan, A, Johnson, BJ, Oltmans, SJ, Fujiwara, M, Vömel, H, Allaart, M, Piters, A, Coetzee, GJR, Posny, F, Corrales, E, Andres, J, Diaz, C, Félix, N, Komala, N, Lai, M, Maata, F, Mani, Z, Zainal, S-Y, Ogino, F, Paredes, T, Luiz Bezerra Penha, F, Raimundo da Silva, S, Sallons-Mitro, HB, Selkirk, F, Schmidlin, J, Stuebi, R and **Thiongo, K.** 2017. First reprocessing of Southern Hemisphere Additional Ozonesondes (SHADOZ) Ozone Profiles (1998–2016). 2. Comparisons with satellites and ground-based instruments. *J. Geophys. Res.*, in press. DOI: https://doi.org/10.1002/2017JD027406

Thouret, V, Cammas, J-P, Sauvage, B, Athier, G, Zbinden, R, Nédélec, P, Simon, P and **Karcher, F.** 2006. Tropopause referenced ozone climatology and inter-annual variability (1994–2003) from the MOZAIC programme. *Atmos. Chem. Phys.* **6**: 1033–1051. DOI: https://doi.org/10.5194/acp-6-1033-2006

Thouret, V, Marenco, A, Logan, JA, Nédélec, P and **Grouhel, C.** 1998. Comparisons of ozone measurements from the MOZAIC airborne program and the ozone sounding network at eight locations. *J. Geophys. Res.* **103**(D19): 25695–25720. DOI: https://doi.org/10.1029/98JD02243

Tombrou, M, Bossioli, E, Kalogiros, J, Allan, JD, Bacak, A, Biskos, G, Coe, H, Dandou, A, Kouvarakis, G,

Mihalopoulos, N, Percival, CJ, Protonotariou, AP and **Szabó-Takács, B.** 2015. Physical and chemical processes of air masses in the Aegean Sea during Etesians: Aegean-GAME airborne campaign. *Sci. Total Environ* 506–507, 201–216. DOI: https://doi.org/10.1016/j.scitotenv.2014.10.098

Trickl, T, Feldmann, H, Kanter, H-J, Scheel, HE, Sprenger, M, Stohl, A and **Wernli, H.** 2010. Forecasted deep stratospheric intrusions over Central Europe: case studies and climatological aspects. *Atmos. Chem. Phys.* **10**: 499–524. DOI: https://doi.org/10.5194/acp-10-499-2010

Trickl, T, Vogelmann, H, Giehl, H, Scheel, H-E, Sprenger, M and **Stohl, A.** 2014. How stratospheric are deep stratospheric intrusions? *Atmos. Chem. Phys.* **14**: 9941–9961. DOI: https://doi.org/10.5194/acp-14-9941-2014

Tyrlis, E, Škerlak, B, Sprenger, M, Wernli, H, Zittis, G and **Lelieveld, J.** 2014. On the linkage between the Asian summer monsoon and tropopause fold activity over the eastern Mediterranean and the Middle East. *J. Geophys. Res. Atmos.* **119**. DOI: https://doi.org/10.1002/2013JD021113

U.S. Environmental Protection Agency. 2013. Integrated Science Assessment for Ozone and Related Photochemical Oxidants. EPA/600/R-10/076F. Office of Research and Development, Research Triangle Park, NC (February).

van der A, RJ, et al. 2017. Cleaning up the air: effectiveness of air quality policy for SO_2 and NO_x emissions in China. *Atmos. Chem. Phys.* **17**: 1775–1789. DOI: https://doi.org/10.5194/acp-17-1775-2017

van der Werf, GR, Randerson, JT, Giglio, L, Collatz, GJ, Mu, M, et al. 2010. Global fire emissions and the contribution of deforestation, savanna, forest, agricultural, and peat fires (1997–2009). *Atmos. Chem. Phys.* **10**: 11,707–11,735. DOI: https://doi.org/10.5194/acp-10-11707-2010

Velchev, K, Cavalli, F, Hjorth, J, Marmer, E, Vignati, E, Dentener, F and **Raes, F.** 2011. Ozone over the Western Mediterranean Sea – results from two years of shipborne measurements. *Atmos. Chem. Phys.* **11**: 675–688. DOI: https://doi.org/10.5194/acp-11-675-2011

Verstraeten, WW, Neu, JL, Williams, JE, Bowman, KW, Worden, JR and **Boersma, KF.** 2015. Rapid increases in tropospheric ozone production and export from China. *Nat. Geosci.* **8**: 690–695. DOI: https://doi.org/10.1038/ngeo2493

Vigouroux, C, Blumenstock, T, Coffey, M, Errera, Q, García, O, Jones, NB, Hannigan, JW, Hase, F, Liley, B, Mahieu, E, Mellqvist, J, Notholt, J, Palm, M, Persson, G, Schneider, M, Servais, C, Smale, D, Thölix, L and **De Mazière, M.** 2015. Trends of ozone total columns and vertical distribution from FTIR observations at eight NDACC stations around the globe. *Atmos. Chem. Phys.* **15**: 2915–2933. DOI: https://doi.org/10.5194/acp-15-2915-2015

Vigouroux, C, De Mazière, M, Demoulin, P, Servais, C, Hase, F, Blumenstock, T, Kramer, I, Schneider, M, Mellqvist, J, Strandberg, A, Velazco, V, Notholt, J, Sussmann, R, Stremme, W, Rockmann, A, Gardiner, T, Coleman, M and **Woods, P.** 2008. Evaluation of tropospheric and stratospheric ozone trends over Western Europe from ground-based FTIR network observations. *Atmos. Chem. Phys.* **8**: 6865–6886. DOI: https://doi.org/10.5194/acp-8-6865-2008

Wang, T, et al. 2017. Ozone pollution in China: A review of concentrations, meteorological influences, chemical precursors, and effects. *Science of the Total Environment* **575**: 1582–1596. DOI: https://doi.org/10.1016/j.scitotenv.2016.10.081

Wasserstein, RL and **Lazar, NA.** 2016. The ASA's Statement on p-Values: Context, Process, and Purpose. *The American Statistician* **70**: 129–133. DOI: https://doi.org/10.1080/00031305.2016.1154108

Wellemeyer, CG, Taylor, SL, Seftor, CJ, McPeters, RD and **Bhatia, PK.** 1997. A correction for the Total Ozone Mapping Spectrometer profile shape errors at high latitude. *J. Geophys. Res.* **102**: 9029–9038. DOI: https://doi.org/10.1029/96JD03965

Wespes, C, Emmons, L, Edwards, DP, Hannigan, J, Hurtmans, D, Saunois, M, Coheur, P-F, Clerbaux, C, Coffey, MT, Batchelor, RL, Lindenmaier, R, Strong, K, Weinheimer, AJ, Nowak, JB, Ryerson, TB, Crounse, JD and **Wennberg, PO.** 2012. Analysis of ozone and nitric acid in spring and summer arctic pollution using aircraft, ground-based, satellite observations and mozart-4 model: source attribution and partitioning. *Atmos. Chem. Phys.* **12**: 237–259. DOI: https://doi.org/10.5194/acp-12-237-2012

Wespes, C, Hurtmans, D, Clerbaux, C, Boynard, A and **Coheur, P-F.** 2018. Decrease in tropospheric O_3 levels of the Northern Hemisphere 1 observed by IASI. *Atmos. Chem. Phys.* Discuss. DOI: https://doi.org/10.5194/acp-2017-904

Wespes, C, Hurtmans, D, Clerbaux, C and **Coheur, P-F.** 2017. O_3 variability in the troposphere as observed by IASI over 2008–2016: Contribution of atmospheric chemistry and dynamics. *J. Geophys. Res. Atmos.* **122**. DOI: https://doi.org/10.1002/2016JD025875

West, JJ, Fiore, AM, Naik, V, Horowitz, LW, Schwarzkopf, MD and **Mauzerall, DL.** 2007. Ozone air quality and radiative forcing consequences of changes in ozone precursor emissions. *Geophys. Res. Lett.* **34**(L06): 806. DOI: https://doi.org/10.1029/2006GL029173

Wilcox, LJ, Hoskins, BJ and **Shine, KP.** 2012. A global blended tropopause based on ERA data. Part I: Climatology. *Q. J. R. Meteorol. Soc.* **138**(L06): 806. DOI: https://doi.org/10.1002/qj.951

Wirth, V. 2000. Thermal versus dynamical tropopause in upper-tropospheric balanced flow anomalies. *Q.J.R. Meteorol. Soc.* **126**: 299–317. DOI: https://doi.org/10.1002/qj.49712656215

Witte, JC, Thompson, AM, Smit, HG, Fujiwara, M, Posny, F, Coetzee, GJ, Northam, ET, Johnson, BJ, Sterling, CW, Mohamad, M and **Ogino, SY.** 2017. First reprocessing of Southern Hemisphere

ADditional OZonesondes (SHADOZ) profile records (1998-2015) 1: Methodology and evaluation. *Journal of Geophysical Research: Atmospheres* **122**: 6611–6636. DOI: https://doi.org/10.1002/2016JD026403

Worden, J, et al. 2009. Observed vertical distribution of tropospheric ozone during the Asian summertime monsoon. *J. Geophys. Res.* **114**(D13): 304. DOI: https://doi.org/10.1029/2008JD010560

Worden, H, Bowman, KW, Kulawik, S and **Aghedo, A.** 2011. Sensitivity of outgoing longwave radiative flux to the global vertical distribution of ozone characterized by instantaneous radiative kernels from Aura-TES. *J. Geophys. Res.* **116**(D14): 115. DOI: https://doi.org/10.1029/2010JD015101

Worden, HM, Bowman, KW, Worden, JR, Eldering, A and **Beer, R.** 2008. Satellite measurements of the clear-sky greenhouse effect from tropospheric ozone. *Nat. Geosci.* **1**: 305–308. DOI: https://doi.org/10.1038/ngeo182

WMO. 1957. Meteorology–A three-dimensional science: Second session of the commission for aerology. *WMO bull.* IV4, 134–138.

WMO. 2010. **Douglass, A** and **Fioletov, V** (Coordinating Lead Authors), **Godin-Beekmann, S, Müller, R, Stolarski, R, Webb, A, Arola, A, Burkholder, J, Burrows, J, Chipperfield, M, Valverde Canossa, J, Cordero, R, David, C, den Outer, P, Diaz, S, Flynn, L, Hegglin, M, Herman, J, Huck, P, Janjai, S, Janosi, I, Krzyscin, J, Liu, Y, Logan, J, McKenzie, R, Matthes, K, Muthama, NJ, Petropavlovskikh, I, Pitts, M, Rex, SRM, Salawitch, R, Sinnhuber, B-M, Staehelin, J, Strahan, S, Tourpali, K** and **Vigouroux, C.** 2011. Stratospheric Ozone and Surface Ultraviolet Radiation, Chapter 2 in Scientific Assessment of Ozone Depletion: 2010, Global Ozone Research and Monitoring Project–Report No. **52**: 516. World Meteorological Organization, Geneva, Switzerland.

WMO. 2014. **Pawson, S** and **Steinbrecht, W** (Lead authors), **Charlton-Perez, AJ, Fujiwara, M, Karpechko, AY, Petropavlovskikh, I, Urban, J** and **Weber, M.** 2014. Update on Global Ozone: Past, Present, and Future, Chapter 2 in Scientific Assessment of Ozone Depletion: 2014. *Global Ozone Research and Monitoring Project-Report No.* 55, 416, World Meteorological Organization, Geneva, Switzerland.

Wu, S, Mickley, LJ, Jacob, DJ, Logan, JA, Yantosca, RM, et al. 2007. Why are there large differences between models in global budgets of tropospheric ozone? *J. Geophys. Res.* **112**(D05): 302. DOI: https://doi.org/10.1029/2006JD007801

Xu, W, Lin, W, Xu, X, Tang, J, Huang, J, Wu, H and **Zhang, X.** 2016. Long-term trends of surface ozone and its influencing factors at the Mt Waliguan GAW station, China–Part 1: Overall trends and characteristics. *Atmos. Chem. Phys.* **16**: 6191–6205. DOI: https://doi.org/10.5194/acp-16-6191-2016

Xue, L, et al. 2014. Increasing External Effects Negate Local Efforts to Control Ozone Air Pollution: A Case Study of Hong Kong and Implications for Other Chinese Cities. *Environ. Sci. Technol.* **48**. DOI: https://doi.org/10.1021/es503278g

Yamasoe, M, Sauvage, B, Thouret, V, Nédélec, P, LeFlochmoen, E and **co-authors.** 2015. Analysis of tropospheric ozone and carbon monoxide profiles over South America based on MOZAIC/IAGOS database and model simulations. *Tellus B,* **67**: 27884. DOI: https://doi.org/10.3402/tellusb.v67.27884

Young, PJ, et al. 2013. Pre-industrial to end 21st century projections of tropospheric ozone from the Atmospheric Chemistry and Climate Model Intercomparison Project (ACCMIP). *Atmos. Chem. Phys.* **13**: 2063–2090. DOI: https://doi.org/10.5194/acp-13-2063-2013

Young, PJ, Naik, V, et al. 2018. **Young, PJ, Naik, V, Fiore, AM, Gaudel, A, Guo, J, Lin, MY,** et al. 2018. Tropospheric Ozone Assessment Report: Assessment of global-scale model performance for global and regional ozone distributions, variability, and trends. *Elem Sci Anth.* **6**(1): 10. DOI: https://doi.org/10.1525/elementa.265

Zanis, P, Hadjinicolaou, P, Pozzer, A, Tyrlis, E, Dafka, S, Mihalopoulos, N and **Lelieveld, J.** 2014. Summertime free-tropospheric ozone pool over the eastern Mediterranean/Middle East. *Atmos. Chem. Phys.* **14**: 115–132. DOI: https://doi.org/10.5194/acp-14-115-2014

Zbinden, RM, Thouret, V, Ricaud, P, Carminati, F, Cammas, J-P and **Nédélec, P.** 2013. Climatology of pure tropospheric profiles and column contents of ozone and carbon monoxide using MOZAIC in the mid-northern latitudes (24°N to 50°N) from 1994 to 2009. *Atmos. Chem. Phys.* **13**(24): 12363–12388. DOI: https://doi.org/10.5194/acp-13-12363-2013

Zeng, G, Morgenstern, O, Shiona, H, Thomas, AJ, Querel, RR and **Nichol, SE.** 2017. Attribution of recent ozone changes in the Southern Hemisphere mid-latitudes using statistical analysis and chemistry-climate model simulations. *Atmos. Chem. Phys.* Discuss. DOI: https://doi.org/10.5194/acp-2017-386

Zerefos, CS, Kourtidis, KA, Melas, D, Balis, D, Zanis, P, Katsaros, L, Mantis, HT, Re-papis, C, Isaksen, I, Sundet, J, Herman, J, Bhartia, PK and **Calpini, B.** 2002. Photo-chemical Activity and Solar Ultraviolet Radiation (PAUR) Modulation factors: An overview of the project. *J. Geophys. Res.* **107**(D18): 8134. DOI: https://doi.org/10.1029/2000JD00134

Zhang, Y, Cooper, OR, Gaudel, A, Thompson, AM, Nédélec, P, Ogino, S-Y and **West, JJ.** 2016. Tropospheric ozone change from 1980 to 2010 dominated by equatorward redistribution of emissions. *Nature Geoscience*. DOI: https://doi.org/10.1038/ngeo2827

Zhao, B, Wang, SX, Liu, H, Xu, JY, Fu, K, Klimont, Z, Hao, JM, He, KB, Cofala, J and **Amann, M.** 2013. NO_x emissions in China: historical trends and future perspectives. *Atmos. Chem. Phys.* **13**: 9869–9897. DOI: https://doi.org/10.5194/acp-13-9869-2013

Ziemke, JR, Chandra, S, Duncan, BN, Froidevaux, L, Bhartia, PK, Levelt, PF and **Waters, JW.**

2006. Tropospheric ozone determined from Aura OMI and MLS: Evaluation of measurements and comparison with the Global Modeling Initiative's Chemical Transport Model. *J. Geophys. Res.* **111**(D19): 303. DOI: https://doi.org/10.1029/2006JD007089

Ziemke, JR, Chandra, S, Oman, LD and **Bhartia, PK.** 2010. A new ENSO index derived from satellite measurements of column ozone. *Atmos. Chem. Phys.* **10**: 3711–3721. DOI: https://doi.org/10.5194/acp-10-3711-2010

Ziemke, JR and **Cooper, OR.** 2017. [Global Climate] Tropospheric Ozone [in "State of the Climate in 2016"]. *Bull. Amer. Meteor. Soc.*, in review.

Ziemke, JR, Douglass, AR, Oman, LD, Strahan, SE and **Duncan, BN.** 2015. Tropospheric ozone variability in the tropical Pacific from ENSO to MJO and shorter timescales. *Atmos. Chem. Phys.* **15**: 8037–8049. DOI: https://doi.org/10.5194/acp-15-8037-2015

How to cite this article: Gaudel, A, Cooper, OR, Ancellet, G, Barret, B, Boynard, A, et al. 2018. Tropospheric Ozone Assessment Report: Present-day distribution and trends of tropospheric ozone relevant to climate and global atmospheric chemistry model evaluation. *Elem Sci Anth,* 6: 39. DOI: https://doi.org/10.1525/elementa.291

Domain Editor-in-Chief: Detlev Helmig, Institute of Alpine and Arctic Research, University of Colorado Boulder, US

Associate Editor: Alastair Lewis, National Centre for Atmospheric Science, University of York, GB

Knowledge Domain: Atmospheric Science

Part of an *Elementa* Special Feature: Tropospheric Ozone Assessment Report (TOAR): GLOBAL METRICS FOR CLIMATE CHANGE, HUMAN HEALTH AND CROP/ECOSYSTEM RESEARCH

Submitted: 06 November 2017 **Accepted:** 25 March 2018 **Published:** 10 May 2018

ELEMENTA Science of the Anthropocene

Elem Sci Anth is a peer-reviewed open access journal published by University of California Press.

OPEN ACCESS